

Final Report – December 2009

Project PECASE: Nanostructure Hybrid Organic/Inorganic Materials for Active Opto-Electronic Devices

Award # FA955004-1-0462

Prof. Vladimir Bulović
Electrical Engineering and Computer Science Department
M.I.T.

We had a number of successes in developing the new generation of light emitting devices (LEDs) based on heterogeneous integration of organic thin films and inorganic nanocrystal quantum dot (QD) lumophores. This report outlines in one-page summaries a series of successful demonstrations. The eleven attached publications further enumerate on our technical successes.

We demonstrated:

1. ... QD-LEDs of red, green, and blue color emission using identical structures for all three colors, by just replacing the QD lumophore layer in the device stack. Our devices drastically simplify the fabrication process of pixelated multicolor emitters as our device design requires only one layer (QD layer) difference between different color emitters.
2. ... a method for patterning different color QD-LED with high resolution, as needed for pixelated display or detector structures. This is the first demonstration of high resolution patterns of QD monolayers, with demonstrated lateral resolution of sub-200nm.
3. ... the first resonant cavity QD-LEDs, a QD-LED device embedded in a microcavity of thickness comparable to the emission wavelength of the QD lumophores. Consequently, the photon emission out of these devices is highly directional.
4. ... energy transfer from a phosphorescent organic thin film to a QD monolayer, demonstrating, for the first time, that QDs can accept triplet excitons of efficient organic dyes through a resonant energy transfer method.
5. ... numerical simulation of the packing of QDs in an ordered monolayer of hexagonally packed QD spheres (5nm in diameter). We demonstrated that in order to achieve the perfectly ordered packing, as we observe, the standard deviation of diameter of QDs can not exceed 5%. This indicates that nearly all of the QDs in our samples are the same to within a single atomic bond, a remarkable precision in QD synthesis.
6. ... the first white QD-LEDs with electroluminescent emission emanating from a monolayer of mixed quantum dots. We show that QD-LEDs can be generated with an arbitrary spectrum by simply mixing different QDs in the electroluminescent layer, akin to mixing paints in a paint shop.

Report Documentation Page				Form Approved OMB No. 0704-0188	
Public reporting burden for the collection of information is estimated to average 1 hour per response, including the time for reviewing instructions, searching existing data sources, gathering and maintaining the data needed, and completing and reviewing the collection of information. Send comments regarding this burden estimate or any other aspect of this collection of information, including suggestions for reducing this burden, to Washington Headquarters Services, Directorate for Information Operations and Reports, 1215 Jefferson Davis Highway, Suite 1204, Arlington VA 22202-4302. Respondents should be aware that notwithstanding any other provision of law, no person shall be subject to a penalty for failing to comply with a collection of information if it does not display a currently valid OMB control number.					
1. REPORT DATE 03 JAN 2011		2. REPORT TYPE Final		3. DATES COVERED 30-09-2004 to 29-09-2009	
4. TITLE AND SUBTITLE Nanostructure Hybrid Organic/Inorganic Materials for Active Opto-Electronic Devices (PECASE)				5a. CONTRACT NUMBER FA9550-04-1-0462	
				5b. GRANT NUMBER	
				5c. PROGRAM ELEMENT NUMBER	
6. AUTHOR(S) Vladimir Bulovic				5d. PROJECT NUMBER	
				5e. TASK NUMBER	
				5f. WORK UNIT NUMBER	
7. PERFORMING ORGANIZATION NAME(S) AND ADDRESS(ES) Massachusetts Institute of Technology, 77 Massachusetts Ave., 13-3138, Cambridge, MA, 02139				8. PERFORMING ORGANIZATION REPORT NUMBER ; AFRL-OSR-VA-TR-2011-0202	
9. SPONSORING/MONITORING AGENCY NAME(S) AND ADDRESS(ES) AFOSR, 875 North Randolph Street, Suite 325, Arlington, VA, 22203				10. SPONSOR/MONITOR'S ACRONYM(S)	
				11. SPONSOR/MONITOR'S REPORT NUMBER(S) AFRL-OSR-VA-TR-2011-0202	
12. DISTRIBUTION/AVAILABILITY STATEMENT Approved for public release; distribution unlimited					
13. SUPPLEMENTARY NOTES					
14. ABSTRACT <p>"The scope of this proposal is nanoscale integration of organic and inorganic materials into hybrid optoelectronic structures to create active devices that combine the diversity of organic materials with the high performance electronic and optical properties of inorganic nanocrystals. The proposal addresses three areas of nanoscale intergration and active device development: (1) the directed structuring of materials at the nanoscale through patterning and material growth methods, (2) the development of model systems as test beds to understand electrical and optical processes in hybrid organic/inorganic materials, and (3) applying the physical principles learned to the development of high-preformance active nanostructured devices. The following preliminary appliactions are proposed as examples of technologies that can be substantially enhanced by our methods: (1) hybrid organic/inorganic light emitting devices (LEDs) based on engineered organic/nanocrystal junctions, (2) hybrid organic/inorganic efficient photodectors with tunability from the UV to the IR, and (3) nanopatterning at 2 to 10 nm scale using periodic arrays of ordered nanocrystals."</p>					
15. SUBJECT TERMS					
16. SECURITY CLASSIFICATION OF:			17. LIMITATION OF ABSTRACT Same as Report (SAR)	18. NUMBER OF PAGES 67	19a. NAME OF RESPONSIBLE PERSON
a. REPORT unclassified	b. ABSTRACT unclassified	c. THIS PAGE unclassified			

7. ... a printing method for patterning top electrode of molecular and quantum dot devices, demonstrating lateral resolution of better than 20 μ m over macroscopic areas. The method was used to demonstrate red-green-blue-emissive QD-LED structures with resolution of 1000 dots-per-inch.
8. ... first analysis of electronic and excitonic processes in hybrid organic/inorganic QD-LEDs, identifying the exciton energy transfer processes as dominantly determining the performance of these devices.
9. ... first all-inorganic QD-LED structures. In these devices QD lumophores are surrounded by metal-oxide charge-transporting thin films, enabling stable operation even under very high current densities.
10. ... a method for patterning thin film electrodes of nanostructured LEDs by Contact lift-off with an elastomeric stamp. The fabricated structures have operational performance that matches that of conventionally patterned structures, yet our new patterning method is simpler.
11. ... inkjet printed films of luminescent QDs that are used as patterned films of AC-driven thin film electroluminescent (AC-EL) structures. We demonstrated that red and green QD luminescence complements the blue luminescence of the AC-EL to generate of full-color triangle.
12. ... AC-driven electroluminescence from phosphor-doped nanocrystals. This s the first demostration of electrical excitation of these new QD structures.
13. ... electroluminescence from single QD light sources. These are the smallest electrically excited light structures, with typical lateral dimension of less than 10 nm.

PUBLICATIONS associated with the PECASE grant:

1. P.O. Anineeva, , C.F. Madigan, S.A. Coe-Sullivan, J.S. Steckel, M.G. Bawendi, and V. Bulović, "Photoluminescence of CdSe/ZnS Core/Shell Quantum Dots Enhanced by Energy Transfer from a Phosphorescent Donor," *Chemical Physics Letters*, 424, 120 (2006).
2. J.-M. Caruge, J.E. Halpert, V. Bulović, and M.G. Bawendi, "NiO as an Inorganic Hole-Transporting Layer in Quantum-Dot Light-Emitting Devices," *Nano Letters* 6, 2991 (2006).
3. J.S. Steckel, P. Snee, S. Coe-Sullivan, J.P. Zimmer, J.E. Halpert, P. Anikeeva, L. Kim, V. Bulovic, M.G. Bawendi, "Color-Saturated Green-Emitting QD-LEDs," *Angewandte Chemie International Edition*, 45, 5796 –5799 (2006).
4. P.O. Anikeeva, J.E. Halpert, M.G. Bawendi, V. Bulović, "Electroluminescence from a mixed red-green-blue colloidal quantum dot monolayer," *Nano Letters* 7, 2196 (2007).
5. H. Huang, A. Dorn, V. Bulović, M.G. Bawendi, "Electrically Driven Light Emission from Single Colloidal Quantum Dots at Room Temperature," *Applied Physics Letters* 90, 023110 (2007).

6. H. Huang, A. Dorn, G.P. Nair, V. Bulović, M.G. Bawendi, "Bias-Induced Photoluminescence Quenching of Single Colloidal Quantum Dots Embedded in Organic Semiconductors," *Nano Letters* 7, 3781-3786, 6 pages (2007).
7. J. Yu and V. Bulović, "Micropatterning metal electrode of organic light emitting devices using rapid polydimethylsiloxane lift-off," *Applied Physics Letters* 91, 043102, 3 pages (2007).
8. J.M. Caruge, J.E. Halpert, V. Wood, V. Bulović, and M.G. Bawendi, "Colloidal Quantum-Dot Light-Emitting Diodes with Metal-Oxide Charge Transport Layers," *Nature Photonics* 2, 247 (2008).
9. Kim, L., P.O. Anikeeva, S.A. Coe-Sullivan, J.S. Steckel, M.G. Bawendi, and V. Bulović, "Contact Printing of Quantum Dot Light-Emitting Devices," *Nano Letters* 8, 4513 (2008).
10. Wood, V., M.J. Panzer, J. Chen, M.S. Bradley, J.E. Halpert, M.G. Bawendi, and V. Bulović, "Inkjet-Printed Quantum Dot-Polymer Composites for Full-Color AC-Driven Displays," *Advanced Materials* 21, 2151 (2009).
11. Wood, V., J.E. Halpert, M.J. Panzer, M.G. Bawendi, V. Bulović, "Alternating Current Driven Electroluminescence from ZnSe/ZnS:Mn/ZnS Nanocrystals," *Nano Letters* 9, 2367 (2009).

Ph.D. THESIS that were partially supported by the PECASE grant:

1. Vanessa Wood (October 2009)
"Electrical Excitation of Colloidally Synthesized Quantum Dots in Metal Oxide Structures"
2. Polina Anikeeva (February 2009)
"Physical Properties and Design of Light-Emitting Devices Based on Organic Materials and Nanoparticles"
3. Jennifer Yu (September 2008)
"Improving OLED Technology for Displays"
4. Seth Coe-Sullivan (June 2005)
"Hybrid Organic/Quantum Dot Thin Film Structures and Devices"

Prof. Vladimir Bulović
M.I.T. Room 13-3138
Organic and Nanostructured Electronics Lab
77 Massachusetts Ave, Cambridge, MA 02139

tel: (617) 253-7012
<http://onelab.mit.edu>

Quantum Dot Light-Emitting Devices

S. Coe-Sullivan, P. Anikeeva, J. Steckel, M. Bawendi, and V. Bulović

Hybrid organic/inorganic light-emitting devices (QD-LEDs) combine stability and color clarity of semiconductor nanoparticles and low cost processing procedures of organic materials with the aim to generate a flat panel display technology. Semiconductor quantum dots (QDs) are nanocrystals that are of smaller diameter than the Bohr exciton in a bulk crystal of the same material. By reducing the size of the nanocrystal, quantum confinement effects lead to an increase in the band edge exciton energy. Changing QDs sizes and materials one can obtain luminescence wavelength from UV, through whole visible spectrum, and near IR.

Typical QD-LED consists of a transparent inorganic anode deposited on a glass substrate followed by organic electron (ETL) and hole transport layers (HTL) with QD monolayer in between, a metal anode is deposited on top of the structure Fig.1 and 2 (left). We are presently investigating physical mechanisms that govern light generation in QD-LED. Time-resolved optical methods allow us to study charge and exciton transport in organic films and at organic/QD interfaces, Fig. 2 (right). Physical insights lead to an optimized design and improved performance of QD-LEDs.

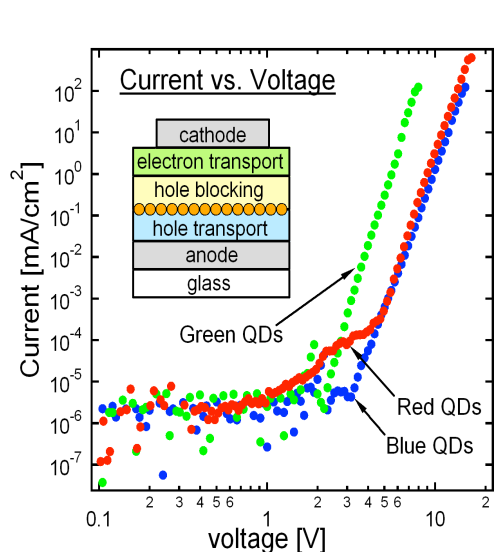


Fig.1 Current-Voltage (IV) characteristics of QD-LEDs with monolayers of red, green, and blue QDs as the recombination layers. Top left corner: device structure

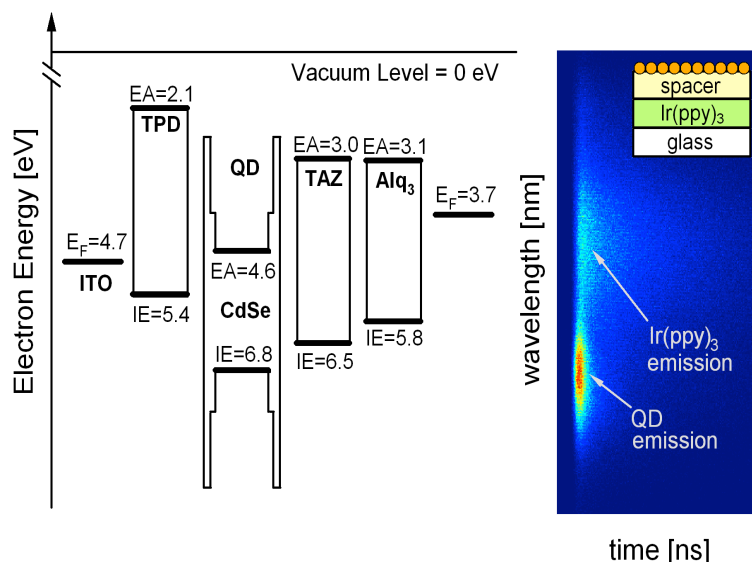


Fig.2 On the left: level diagram of a typical QD-LED. On the right: time-resolved photoluminescence measurement of the structure on the top right corner.

Patterned Quantum Dot Monolayers in QD-LEDs

S. Coe-Sullivan, L. Kim, J. Steckel, R. Tabone, M.G. Bawendi, and V. Bulović

Hybrid organic/inorganic quantum dot light emitting devices (QD-LEDs) contain luminescent nanocrystal quantum dots (QDs) imbedded in an organic thin film structure. The QDs are nanometer size particles of inorganic semiconductors that exhibit efficient luminescence and whose emission color can be tuned by changing the size of the nanocrystals. For example, luminescence of QDs of CdSe is tuned from blue to red by changing the QD diameter from 2 nm to 12 nm. By further changing the material system, saturated color emission can be tuned from the UV, through the visible, and into the IR. The inorganic emissive component provides potential for a long operating lifetime of QD-LEDs. The room temperature fabrication method ensures compatibility of the QD-LED technology with the established all-organic LEDs (OLEDs).

The optimized QD-LED device structure contains a single monolayer of QDs embedded within the layered organic thin film structure. The technology is enabled by the self-assembly of the QDs as a densely packed monolayer on top of a conjugated organic film. The QD film is positioned with nanometer precision in the recombination zone of the device. Most recently, by using a microcontact printing (stamping) process we demonstrated that neat layers of QDs can be placed independently of the organic layers and in-plane patterned, allowing for the pixel formation necessary for display technology (Fig. 1). To date, we demonstrated QD-LED color emission across the visible part of the spectrum and from 1.3 μm to 1.6 μm in the near infra-red (Fig. 2).

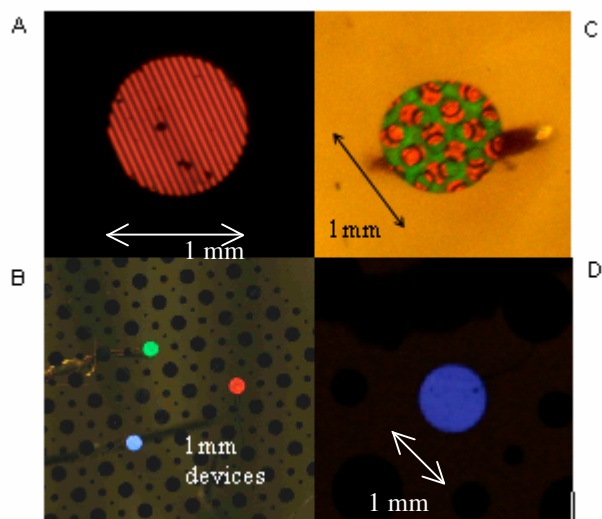


Figure 1: (A) 25 μm wide lined red QD-LED, patterned by microcontact printing (stamping). (B) Stamped red QD-LED, stamped green QD-LED, and blue organic LED. (C) Stamped patterned green/red QD-LED. (D) Stamped blue QD-LED.

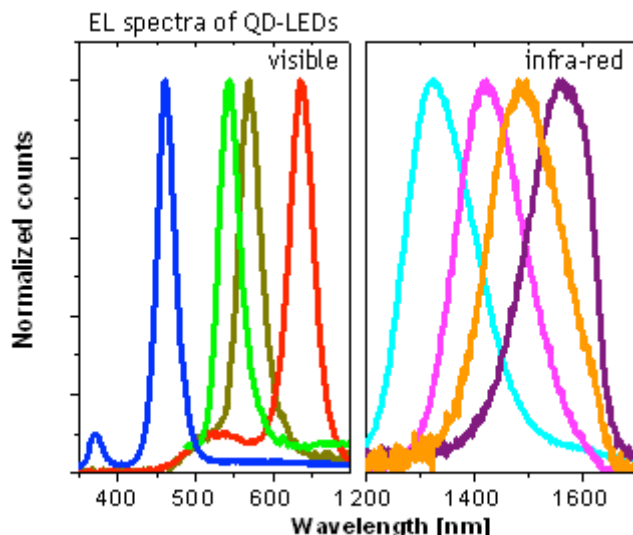


Figure 2: Electroluminescence spectra of QD-LEDs in visible and infra-red.

References:

- [1] Coe-Sullivan, S., W. Woo, J. Steckel, M.G. Bawendi, and V. Bulović, "Tuning the Performance of Hybrid Organic/Inorganic Quantum Dot Light-Emitting Devices," *Organic Electronics* 4, 123 (2003).

Resonant Cavity Quantum Dot LEDs

V. Wood, J.R. Tischler, V. Bulović

Quantum dot LEDs (QD-LEDs), which capitalize on the excellent color saturation and high photoluminescence efficiencies offered by quantum dots, promise to be part of future generation display technologies [1]. The goal of our project is to integrate the already developed technology of the QD-LED into a resonant cavity (RC) and thereby achieve enhanced, directed electroluminescence (EL) that can be of use in fields as diverse as optical communications, spectroscopy, and environmental and industrial sensing.

The RC structure we are currently investigating (Figure 1) consists of a standard QD-LED [1] grown on top of a distributed Bragg reflector (DBR). A DBR is a highly reflective mirror made of $\lambda/4$ layers of alternating high and low indices of refraction. With a reflectivity of more than 98% in the wavelength region of interest, the DBR serves as one of the cavity mirrors. The other cavity mirror is the Ag doped Mg electrode of the QD-LED.

With this structure, we have achieved narrowed emission, which is evident when comparing EL spectra and images of the QD-LED and the RC QD-LED (Figure 2). The QD-LED appears orange because our eyes sense the red light of the QDs as well as the shorter wavelength emission from the organics. In contrast, the RC QD-LED exhibits effectively monochromatic red light. The plot of peak emission intensity at different angles (Figure 2) shows an emission cone of less than twenty degrees. If the path-length of the cavity does not match the QD emission wavelength, EL from the RC QD-LED is off-normal. We are currently working to understand the emission enhancement capability of our RC QD-LED.

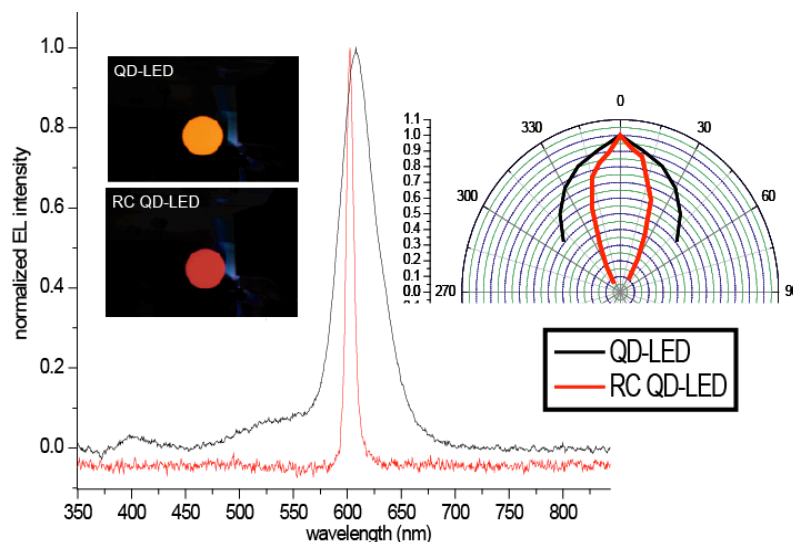
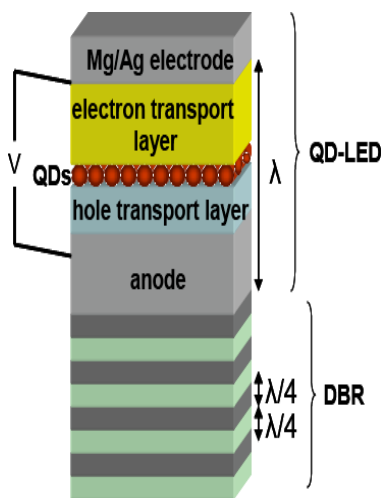


Figure 1: Schematic of RC QD-LED

Figure 2: Comparison of EL spectra, images, and angular emission profiles of RC QD-LED and QD-LED. RC QD-LED exhibits marked narrowing.

Reference

S. Coe, W.K. Woo, M. Bawendi, V. Bulovic, "Electroluminescence from single monolayers of nanocrystals in molecular organic devices," *Nature*, vol.420, no. 6917, pp. 800-803, 2002.

Energy Transfer from an Organic Phosphorescent Thin Film to a Monolayer of Quantum Dots

P. O. Anikeeva, C. F. Madigan, S. A. Coe-Sullivan, J. S. Steckel, M.G. Bawendi, V. Bulović

Over the past several years the optical and electronic properties of colloidal synthesized nanocrystals, or quantum dots (QDs), of CdSe have been extensively studied, with the aim of using QD films in solid state optoelectronic devices. Efficient exciton generation in CdSe QDs suggests use of nanocrystal composite films in photovoltaic cells, while high luminescence quantum yields and tunability of QD emission wavelengths over the entire visible spectrum suggests QD film use in light emitting devices (LEDs). These developments are a consequence of advances in colloidal QD synthesis that allow for increased control over the shape, size, and emission wavelength of nanocrystals, and the development of methods for forming QD thin films of controlled structure and composition. We utilize these advances in the present study to demonstrate triplet exciton energy transfer (ET) from a thin film of phosphorescent molecules to a monolayer of CdSe/ZnS core/shell QDs (see Fig. 1). Triplet exciton harvesting and transfer to an efficient lumophore has been previously used in advancing organic light emitting device (OLED) technology, and has the potential to similarly benefit the emerging field of quantum-dot-LEDs.

The efficient energy transfer is facilitated by the spectral overlap of the organic phosphor fac tris(2-phenylpyridine) iridium (Ir(ppy)_3) luminescence and QD absorption spectra. In time-resolved photoluminescence (PL) measurements the energy transfer is manifested as elongation of the QD PL time constant from 40 ns to 400 ns (see Fig. 2), and a concomitant 55 % increase of time-integrated QD PL intensity. Numerical analysis supports the conclusion that the observed PL dynamics are dominated by exciton diffusion within the Ir(ppy)_3 film to the QD layer, energy transfer to the from Ir(ppy)_3 to QD film, and subsequent QD luminescence.

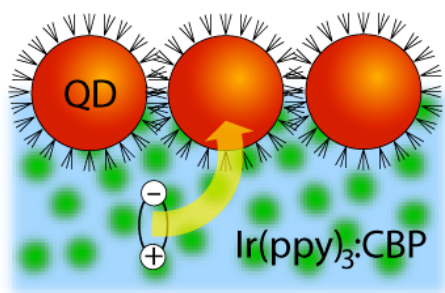


Figure 1: Schematic diagram of the energy transfer from an organic film doped with a phosphorescent donor to a monolayer of colloidal CdSe/ZnS core-shell QDs.

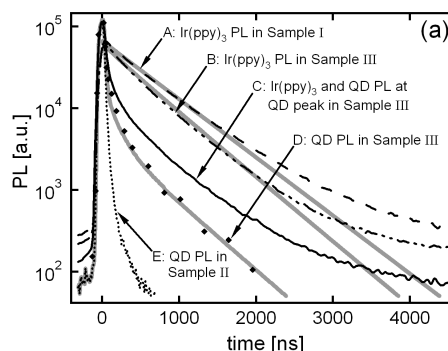


Figure 2: Time resolved PL measurements for samples I, II, and III, which respectively correspond to Ir(ppy)_3 film on glass, QD layer on glass, and QD layer on Ir(ppy)_3 film on glass. The black lines and dots represent the experimental measurements, and the thick grey lines represent numerical fits using the proposed diffusion model. Data set A represents Ir(ppy)_3 PL decay in purely organic sample, data set B represents Ir(ppy)_3 PL decay in contact with QDs, data set C represents QD and Ir(ppy)_3 PL decay in contact with each other at QD PL peak position, data set D represents QD dynamics in contact with Ir(ppy)_3 , data set E represents QD dynamics in purely QD sample.

Packing of Quantum Dot Monolayers

Ethan Howe and Vladimir Bulović

We developed a kinetic model for assembly of ordered quantum dot (QD) monolayers on 2-dimensional surface that reproduces experimental observations for a variety of QD size distributions (of Gaussian size profile). Such QD monolayers have already been utilized in a number of thin-film applications, QD-LEDs and QD-photodetectors. However, methods of fabrication of QD films are still being developed and our work focuses on developing a numerical tool to investigate methods for improving the quality of these films.

To numerically assemble a QD monolayer, we model the QDs as spheres that moves on the surface with no friction but with random thermal motion added at each time step. We apply a van der Waals attraction between QDs and hard-wall repulsion at the QD radius. When two QDs collide, their interaction is partially inelastic based on a model parameter. These conditions allow for a range of behavior encompassing many interesting phenomena. We find that a mono-disperse size distribution of QDs forms hexagonally close-packed aggregates, and the packing and aggregate stability of the QD monolayer degrades dramatically as the standard deviation of the size distribution is increased. In experimental studies [1], the instability of QD monolayers has been observed to occur for standard deviations of greater than 10% in QD diameter. We were able to reproduce these findings in our simulations (Figure 1). We have further shown that confining the same QD distributions inside of a 1-dimensional hard boundary with a width of a few QD diameters can counteract this instability.

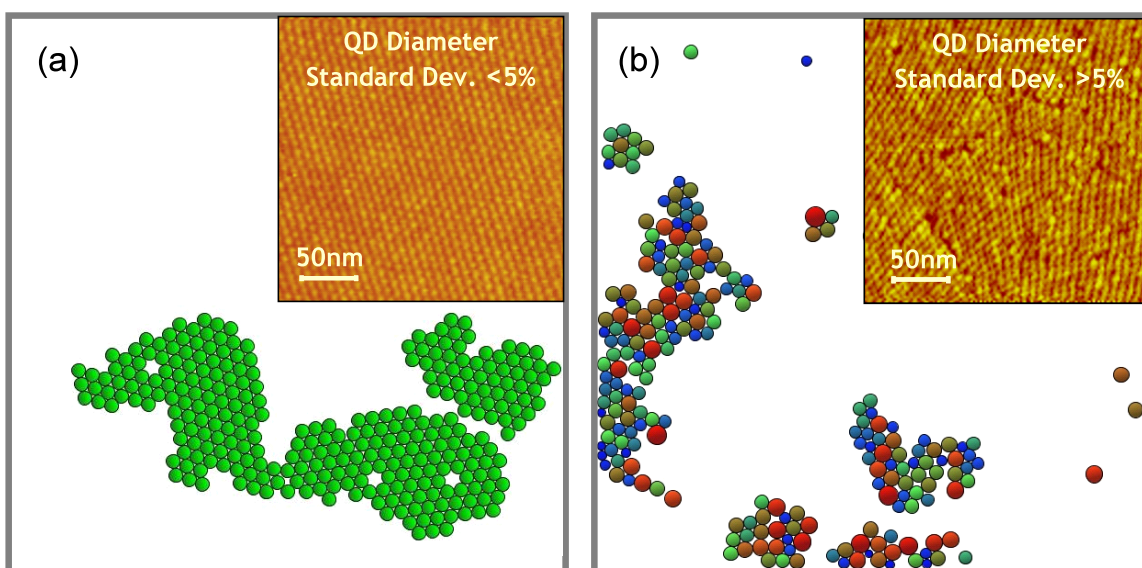


Figure 1: a) Results of simulation of packing for 300 QDs of equal size. The inset is an AFM image [1] of a monolayer of QDs with less than 5% standard deviation in diameters. In our simulation we observe the same hexagonal close-packed arrangement of QDs and stability of aggregates that allows for good monolayer formation. b) Results of simulation for packing 300 QDs with a 15% standard deviation in diameters. The inset is an AFM image for the same method of preparation as a) but with QDs having a greater than 5% standard deviation in diameters. For these large size distributions our simulated dots could no longer form hexagonally close-packed arrays. In addition, aggregates readily broke up as dots were less well-bound.

Reference

S. Coe-Sullivan *et al.*, *Advanced Functional Materials* **15**, 1117-1124 (2005).

White Light QD-LEDs

P. O. Anikeeva, J. E. Halpert, M. G. Bawendi, V. Bulović

We are developing white-light emitting quantum dot LEDs (QD-LEDs) for use as planar white-light sources in the full-color active matrix displays with color filters, and in future solid state lighting. Our white QD-LEDs consist of organic charge transport layers with a QD monolayer sandwiched between them. This device architecture enables independent processing of the charge transport layers and the emissive layer. The independent processing of QDs is a result of the recent development of the QD printing technique, which allows for the solvent-free deposition of QD monolayers onto various organic materials. By mixing different amounts of high quantum yield colloidal core/shell QDs (red CdSe/ZnS, green ZnCdSe/ZnS, blue CdS/ZnS) we demonstrate different QD-LED colors. Figure 1a shows electroluminescence of the white QD-LED with the CIE (Comision International de l'Eclairage) coordinates of (0.42, 0.41). Figure 1b and Inset of Figure 2 also show that CIE coordinates vary only slightly under the different applied bias and different operation time.

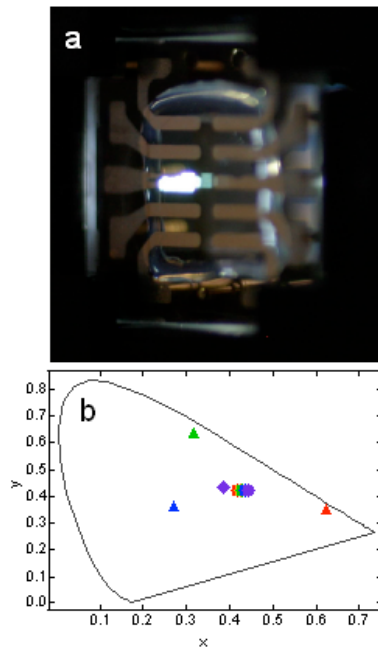


Figure 1: a. Photograph of a white QD-LED operated at 10 V of applied bias. b. CIE coordinates of QD-LEDs: red (red triangle), green (green triangle), blue (blue triangle) and white (purple diamond) at 12 V. Change of color with operation lifetime is shown with progression from red circle to purple circle for a QD-LED operated at 9 V.

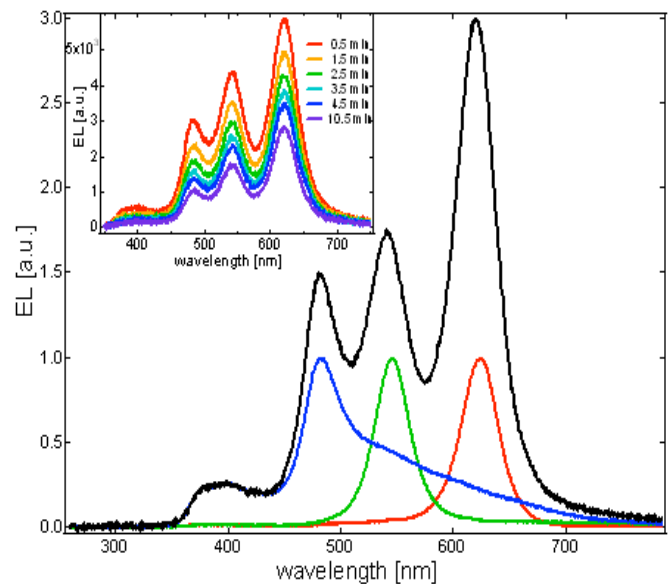


Figure 2: Electroluminescence of the blue (blue line), green (green line), red (red line) and white (black line) QD-LEDs shown not to scale to demonstrate the presence of the spectral signatures of all three QD colors in the white device spectrum. Inset: We observe slight change of the spectral shape of the white QD-LED with operation time.

References

- S. A. Coe-Sullivan, Ph. D thesis, Massachusetts Institute of Technology, Cambridge, 2005.
- P. O. Anikeeva, J. E. Halpert, M. G. Bawendi, V. Bulović, unpublished results.

Patterning Micron-Sized Features of Quantum Dots and Metal Electrodes

J. Yu and V. Bulović

Organic LED (OLED) and quantum dot LEDs (QD-LED) are a promising technology for the emissive element in flat panel displays. However, organic material in these devices are isensitive to solvent exposure and create processing challenges in patterning a pixelated display. This project aims to develop novel fabrication processes for OLED and QD-LED displays.

In QD-LEDs, quantum dots can be patterned by spin-casting a monolayer onto a relief poly(dimethylsiloxane) (PDMS) stamp and then transferring the pattern onto an organic substrate [1]. However, the spin cast process requires significant use of material. An alternative solution is to directly pattern the dots using thermal inkjet pico-fluidic drop dispensing system (TIPS) provided by Hewlett-Packard (Figure 1(a)). A process for formation of patterned monolayer using this technique is currently being developed.

Patterning of electrodes in OLED or QD-LED displays is presently done primarily by shadow masking, which is limited in resolution, or cold-welding which requires high pressures, additional protection layers, use of gold electrode, or subsequent dry etching steps [2,3]. As an alternative, we are investigating subtractive patterning of silver or silver-magnesium electrodes with untreated PDMS stamp. We demonstrated 25 μm feature sizes with good yield on 20nm thick silver-magnesium films (Figure 1(b)). This PDMS lift-off technique applied on an OLED electrode made of 50 nm silver film on top of 50 nm silver-magnesium yields OLEDs with the same quantum efficiency and current voltage characteristics to OLEDs defined by shadow masking (Figure 2).

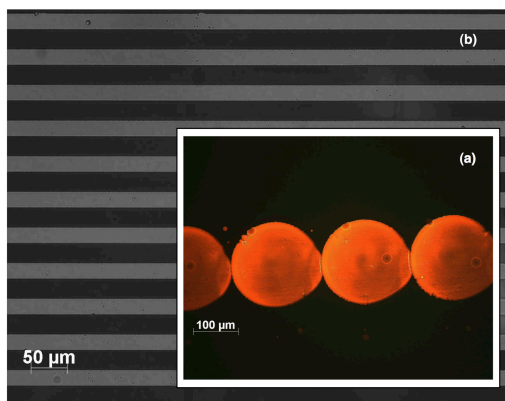


Figure 1

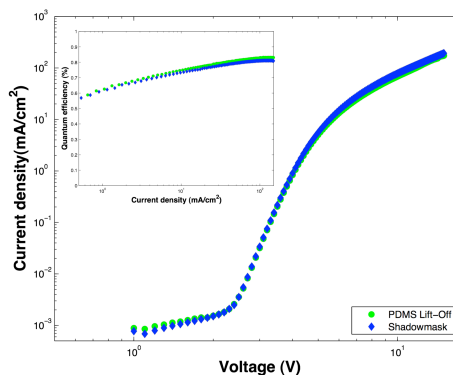


Figure 2

-
- [1] L. Kim. "Deposition of Colloidal Quantum Dots by Microcontact Printing for LED Display Technology", Master's Thesis, Massachusetts Institute of Technology, Cambridge, 2006.
[2] C. Kim, P. Burrows, S. Forrest, "Micropatterning of Organic Electronic Devices by Cold-Welding," Science, vol.288, pp.831-833, May 2000.
[3] C. Kim, S. Forrest. " Fabrication of Organic Light-Emitting Devices by Low-Pressure Cold-Welding," Advanced Materials, vol.15, No. 6, pp. 541-545, March 2003.

Electronic and Excitonic Processes in Quantum Dot LEDs

P. O. Anikeeva, C. F. Madigan, J. E. Halpert, M. G. Bawendi, V. Bulović

Hybrid light emitting devices (LEDs) based on organic charge transporting materials and emissive colloidal quantum dot monolayers have demonstrated superior color purity and high external quantum efficiency close to that of organic LEDs (OLEDs) [1] making them a technology that can potentially replace OLEDs in flat panel displays. While fabrication methods for QD-LEDs have been extensively studied over the past several years, the mechanisms of QD-LED operation still present a significant scientific challenge. Understanding the excitonic and electronic processes in QD-LEDs is crucial to efficient device design.

We investigate the mechanism of operation of the hybrid organic/colloidal quantum dot (QD) light emitting devices (QD-LEDs). By varying the position of the emitting QD monolayer within the stacked organic structure, we find that the quantum efficiency of the device improves by >50% upon imbedding the emissive QD monolayer into the hole-transporting layer <10 nm below the interface between hole and electron transporting layers. We analyze these results in the context of two different mechanisms for QD light emission: the charge injection model and the exciton energy transfer model. We find that maximizing energy transfer contribution to QD luminescence improves QD-LED performance, primarily due to inefficiencies arising from charged QDs..

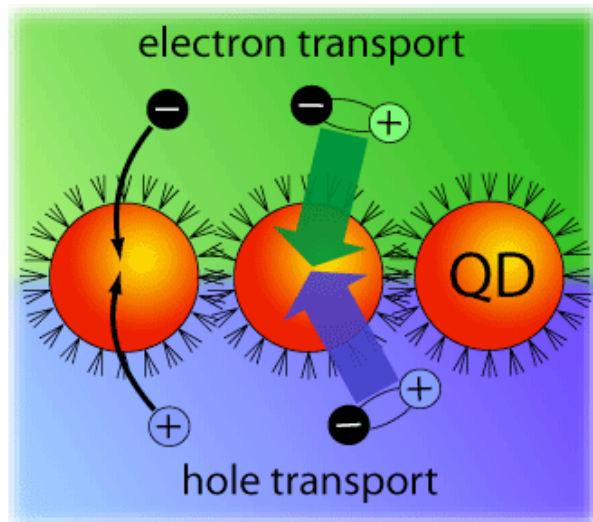


Figure 1: Schematic diagram of the charge injection and energy transfer from an organic charge transporting layers to a monolayer of colloidal CdSe/ZnS core-shell QDs.

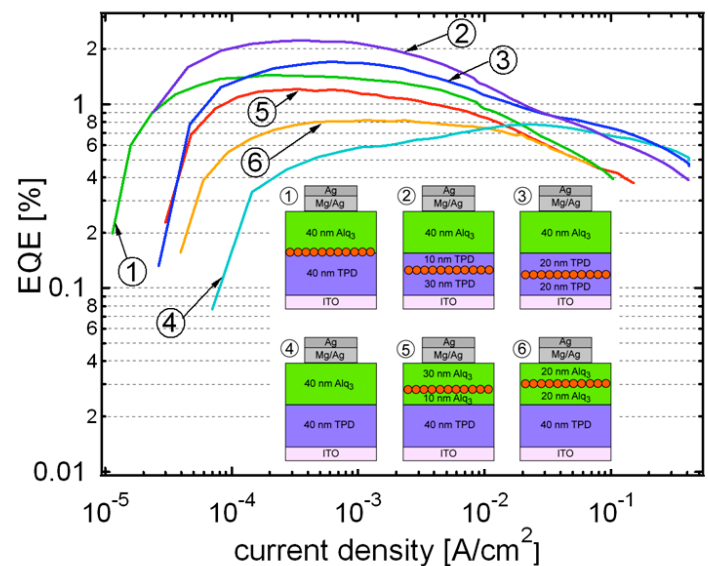


Figure 2: External quantum efficiency curves are shown for six devices displayed in the inset. The highest EQE of 2.3% corresponds to the device 2 in which QD monolayer is imbedded 10 nm into TPD layer below the TPD/Alq3 interface.

References

- S.A. Coe-Sullivan, "Hybrid Organic/Quantum Dot Thin Film Structures and Devices " Ph.D thesis, Massachusetts Institute of Technology, Cambridge, 2005.
- L. Kim, "Deposition of Colloidal Quantum Dots by Microcontact Printing for LED Display Technology" M. Eng. Thesis, Massachusetts Institute of Technology, Cambridge, 2006.

All Inorganic Colloidal Quantum Dot LEDs

V. Wood, J.M. Caruge, J.E. Halpert, M.G. Bawendi, V. Bulović

LEDs with a quantum dot (QD) emissive layer are an attractive technology for display and large area lighting applications. QDs are nanoparticles that can be synthesized to emit anywhere from the ultraviolet to the infrared regions of the spectrum by changing their size and chemical composition. For example, varying the size of CdSe QDs from 17 to 120 Å tunes them to emit light at a wavelength between 470 nm to 630 nm [1]. Furthermore, QDs possess excellent color saturation and high photoluminescence efficiencies.

QDs have been successfully integrated into LEDs with organic charge transport layers. Such devices boast external quantum efficiencies (EQEs) of several percent in the red, green, and blue [2]. However, despite the high EQE and the ease of fabrication offered by organic semiconductor films, organic materials are susceptible to deterioration from atmospheric oxygen and water vapor. Device lifetimes can be improved with packaging, but this increases cost, making it difficult for QD-LEDs to compete with the already established technology of liquid crystal displays (LCDs). Furthermore, organic materials cannot sustain the high current density needed to realize an electrically pumped colloidal QD laser. In contrast, metal oxides are chemically and morphologically stable in air and can operate at high current densities.

We report the first all-inorganic QD-LEDs consisting of radio-frequency sputtered metal-oxide charge transport layers and a colloidal quantum dot electroluminescent region. These devices manifest a 100-fold increase in EQE over the one previously reported inorganic QD structure [3]. Our device consists of ZnCdSe QDs sandwiched between resistive, p-type NiO and co-deposited ZnO and SnO₂ (See Figure 1). We measured an EQE of 0.09% and a peak luminescence of 7000 Cd/m² at 13.8 V and a current density of 3.2 A/cm². As shown in Figure 2, light emission from the QDs is uniform across the device.

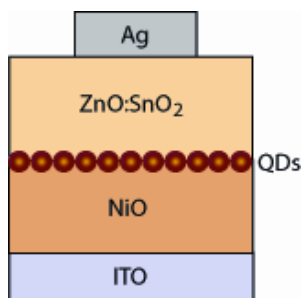


Figure 1: Schematic of the all-inorganic QD-LED structure. Indium tin oxide (ITO) and Ag electrodes are used.

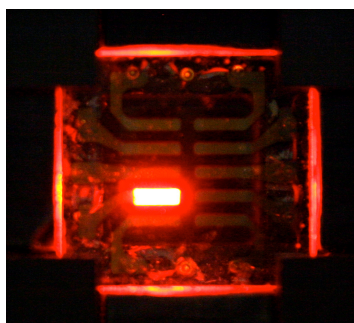


Figure 2: All inorganic QD-LED operating under 6 V applied bias.

References

- C.B. Murray, D.J. Norris, and M.G. Bawendi. "Synthesis and Characterization of Nearly Monodisperse CdE (E = S, Se, Te) Semiconductor Nanocrystallites," *J. Amer. Chem. Soc.*, vol. 115, pp. 8706-8715, 1993.
- P.O. Anikeeva, J.E. Halpert, M.G. Bawendi, and V. Bulović. "Electroluminescence from a Red-Green-Blue Colloidal Quantum Dot Monolayer", to be published.
- A.H. Mueller, M. A. Petruska, M. Achermann, D.J. Werder, E. A. Akhadorov, D. D. Koleske, M. A. Hoffbauer, and V. I. Klimov. "Multicolor light-emitting diodes based on semiconductor nanocrystals encapsulated in GaN charge injection layers," *Nano Lett.*, vol. 5, no. 6, pp. 1039-1044, June 2005.

Microcontact Printing of Quantum Dot LEDs Using Inkjet Assisted Patterning Method

Jennifer Yu, Jianglong Chen, Hao Huang, Mounji Bawendi, Vladimir Bulovic

Colloidal quantum dots (QDs) with tunable emission wavelength, narrow emission band and efficient luminescence have been incorporated into OLEDs and used as lumophores in the QD-LED structure. In the past, the favored method of QD deposition has included a spin-coating step that does not utilize most of the QD material [1] [2]. We propose an alternative method that directly patterns the QD layers on a stamp by inkjet printing and is subsequently transferred onto organic material via microcontact printing (Figure 1a). This technique allows patterning of the QD material and drastically improves material usage in fabrication of QD-LEDs and other optoelectronic devices that utilize QD thin films.

With a thermal inkjet printer from Hewlett Packard, we pattern QDs onto a polydimethylsiloxane (PDMS) stamp with a feature size of 50 μ m. Interaction between the QD solution and the stamp surface plays an important role in the formation of the inkjet printed QD patterns. Coating the stamp with a layer of parylene allows for better drying properties of the ink on the stamp (Figure 1b). The QD patterns have been transfer stamped onto organic hole transport layers (Figure 2a). The QD-LED structure is completed by subsequent deposition of a hole blocking layer, electron transport layer, and electrode, and electroluminescence images of QD-LEDs are shown in Figure 2b,c.

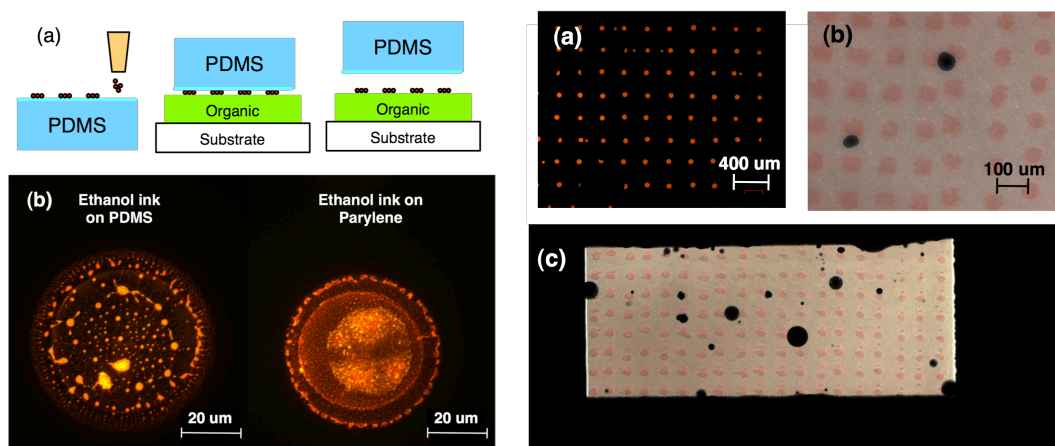


Figure 1: (a) Inkjet printed quantum dot technique (b) Photoluminescence of quantum dot drop on different stamp surfaces.

Figure 2: (a) Photoluminescence of inkjet printed red quantum dots transfer printed from parylene coated PDMS stamp to TPD. (b) (c) Electroluminescence from an inkjet assisted patterned QD-LED.

[1] S. Coe-Sullivan, J. Steckel, W. Woo, M. Bawendi, and V. Bulovic, "Large-area ordered quantum-dot monolayers via phase separation during spin-casting," in *Advanced Functional Materials*, vol. 15, no. 7, pp. 1117-1124, Jul. 2005.

[2] L. Kim. "Deposition of colloidal quantum dots by microcontact printing for LED Display Technology," Master's thesis, Massachusetts Institute of Technology, Cambridge, 2006.

Modeling of Electronic and Excitonic Processes in QD-LEDs

P. O. Anikeeva, C. F. Madigan, J. E. Halpert, M. G. Bawendi, V. Bulović

Hybrid light emitting devices (LEDs), consisting of organic charge transporting layers and a colloidal quantum dot (QD) emissive layer [1], exhibit narrow electroluminescence (EL) spectra, characteristic of colloidal QD luminescence. The manifested saturated color emission is particularly desirable in flat panel display applications, and is broadly applicable to other technologies requiring high spectral quality lighting. The development of novel QD deposition techniques such as microcontact printing [2] allowed us to experimentally investigate the mechanisms of QD-LED operation, by varying the position of the emitting QD monolayer within the stacked organic structure. We find that the quantum efficiency of the device improves by >50% upon imbedding the emissive QD monolayer into the hole-transporting layer <10 nm below the interface between hole and electron transporting layers, while maintaining QD-LED spectral purity (Fig. 1). These findings with additional experiments lead us to conclusion that maximizing exciton generation on organic molecules and subsequent energy transfer to QDs, while minimizing QD charging with electrons improves QD-LED performance.

In order to verify our conclusions based on the previous experimental observations we built a theoretical model for charge and exciton transport in organic LEDs (OLEDs) and QD-LEDs. Considering carrier drift and diffusion we numerically simulate carrier concentration and electric field profiles in device structures and based on them we calculate exciton concentration profiles (Fig. 2). We find that the results of our model are in qualitative agreement with experimental data. We find that exciton diffusion and non-radiative energy transfer from organic thin films to QDs lead to maximum exciton concentration on QD sites resulting in QD-LED spectra dominated by QD emission. We find that imbedding QDs into TPD hole-transporting layer reduces electron concentration at QD sites and consequently eliminates QD luminescence quenching. It also reduces electric field across the QDs eliminating exciton dissociation.

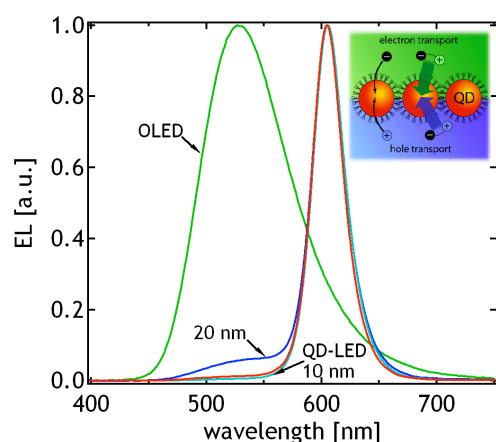


Figure 1: Normalized EL spectra of OLED, QD-LEDs with QDs at the TPD/Alq₃ interface, QDs imbedded into TPD 10 nm and 20 nm below the interface. Inset: Schematic diagram of the charge injection and energy transfer from organic charge transporting layers to a monolayer of colloidal QDs.

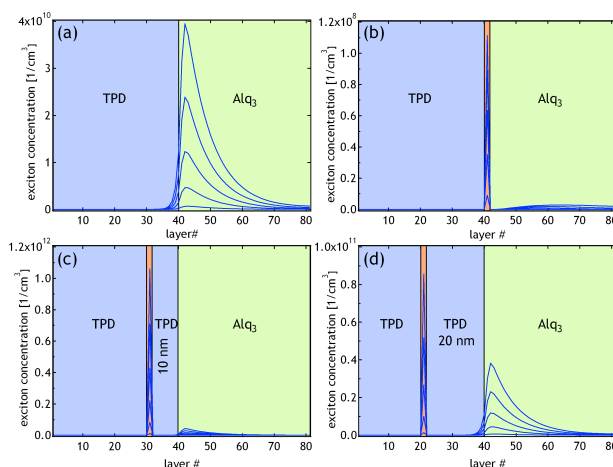


Figure 2: Exciton concentration profiles obtained from numerical simulations for OLED (a), QD-LEDs with QDs at the TPD/Alq₃ interface (b), QDs imbedded into TPD 10 nm (c) and 20 nm (d) below the interface. Theoretical exciton profiles are in qualitative agreement with experimental EL spectra shown in Figure 1.

S.A. Coe-Sullivan, "Hybrid Organic/Quantum Dot Thin Film Structures and Devices " Ph.D thesis, Massachusetts Institute of Technology, Cambridge, 2005.

L. Kim, "Deposition of Colloidal Quantum Dots by Microcontact Printing for LED Display Technology" M. Eng. Thesis, Massachusetts Institute of Technology, Cambridge, 2006.

Micropatterning Organic Electronic Device Electrodes by PDMS lift-off

J. Yu, V. Bulović

Patterning of electrodes in organic electronic devices are done primarily by techniques that are limited in resolution, scalability, or potentially damaging to the underlying organic material. We demonstrate a subtractive stamping technique for patterning the top metal electrode of organic electronic devices. Patterning is achieved by placing a relief patterned polydimethylsiloxane (PDMS) stamp in contact with a metal electrode and quickly peeling off the stamp (Figure 1a). The fast peel rate increases the adhesion energy of the PDMS to the metal electrode, allowing the stamp to pick up the metal from the substrate.

The in-plane roughness of the patterned straight edge is less than 1 μm (Figure 1b) while the transition region of the patterned abrupt step is less than 0.1 μm in width (Figure 1c). We pattern micron sized features on a glass substrate with an ITO step with good yield (Figure 2). We have shown that for organic light emitting devices, this technique is comparable to the traditional shadow masking technique [1]. This technique can also be applied to patterning gold electrodes for organic pentacene transistors.

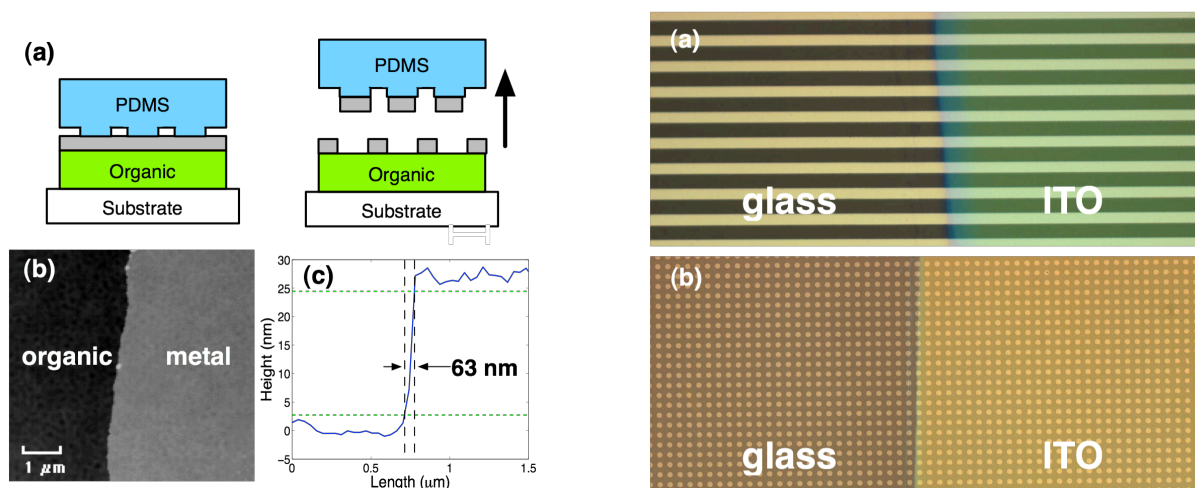


Figure 1: (a) Demonstration of the subtractive stamping technique. A quick release of the PDMS stamp to the substrate is required to lift off metal film from substrate surface. (b) Top view of in-plane roughness of patterned edge of organic to metal from AFM (c) AFM height data to view transition region of organic to metal edge.

Figure 2: Optical microscope image of (a) 13 μm wide lines patterned from 17 nm thick Mg:Ag film and (b) 25 μm diameter circles on 11 nm thick Mg:Ag film on top of 50-nm Alq3, 50-nm TPD, 40-nm PEDOT, and 80-nm ITO or glass substrate. Both images show technique is able to occur even on a step of ITO on a glass substrate.

[1] J. Yu and V. Bulović, "Patterning Micron Sized Features of Quantum Dots and Metal Electrodes," Massachusetts Institute of Technology, Cambridge, MA, Microsystems Technology Laboratory Annual Research Report, 2006.

Inkjet Printed Quantum Dot and Polymer Composites for AC-Driven Electroluminescent Devices

V. Wood, J. Chen, M.J. Panzer, M.S. Bradley, J.E. Halpert, M.G. Bawendi, and V. Bulović

We introduce a technique for the reliable deposition of intricate, multicolored patterns using a quantum dot (QD) and polymer composite and demonstrate its application for robust AC-driven displays with high brightness and saturated colors. AC electroluminescent (AC EL) devices are a well-established technology [1]. Their relatively simple fabrication and long operating lifetimes make them desirable for large area displays; however, a major challenge with AC EL remains finding efficient and stable red phosphors for multicolored displays. Colloidally synthesized QDs are robust, solution-processable lumophores offering tunable and narrowband photoluminescence across the visible spectrum [2]. By integrating QDs into an AC EL device, we demonstrate patterning of saturated red, green, and blue pixels that operate at video brightness.

The concept behind the device operation is optical downconversion: red and green QDs absorb blue electroluminescence from phosphor grains and then emit at longer wavelengths. The device, pictured schematically in Figure 1, is fabricated with a layer by layer approach that is compatible with flexible substrates. A QD and polyisobutylene (PIB) solution is printed on conductive indium tin oxide (ITO) using a Hewlett Packard Thermal Inkjet Pico-fluidic dispensing system (TIPs). Examples of the intricate and multicolored patterns possible are shown in Figure 2a. The electroluminescent phosphor paste (ZnS:Cu powder in a transparent binder from Osram-Sylvania) is deposited uniformly over the sample using a disposable mask and doctor-blading to define the device area. Top contacts are made with conductive tape from 3M. This basic device structure is assembled and tested entirely under atmospheric conditions.

When an AC voltage waveform is applied across the device, we measure spectrally pure QD emission in the red and green and $\sim 100 \text{ Cd/m}^2$ brightness. Photographs of the red, green, and blue pixels of a working, AC-driven device are shown in Figure 2b. The Commission International d'Eclairage (CIE) coordinates of the pixels device define a color triangle that is comparable to the International Telecommunication Union HDTV standard.

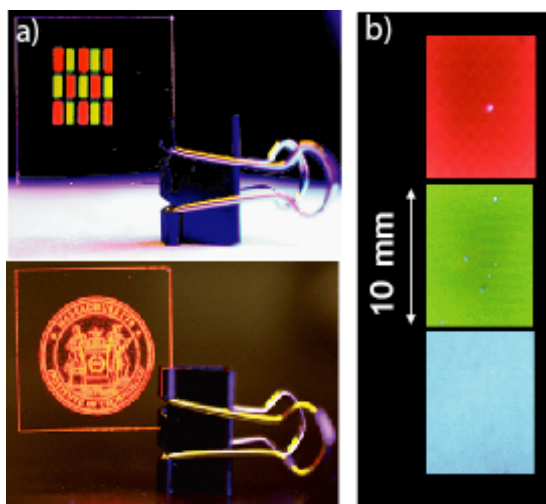
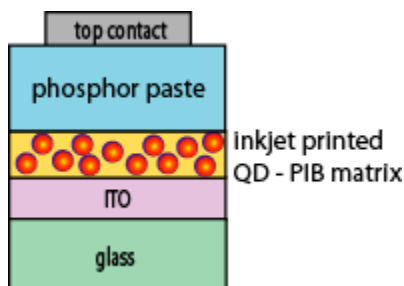


Figure 1: Schematic showing basic device structure.

Figure 2: Photographs of a) photoluminescence of QD-PIB composites inkjet printed on 1 in. x 1 in. indium tin oxide coated glass slides and b) emission from blue, green, and red pixels of completed devices driven at $70 \text{ V}_{\text{rms}}$ and 50 kHz.

[1] Y. A. Ono, *Electroluminescent Displays*. Singapore: World Scientific, 2000.

[2] C.B. Murray, D.J. Norris, and M.G. Bawendi. "Synthesis and characterization of nearly monodisperse CdE (E = S, Se, Te) semiconductor nanocrystallites," *J. Amer. Chem. Soc.*, vol. 115, pp. 8706-8715, 1993.

Electroluminescence from Phosphor-doped Nanocrystals

V. Wood, J. E. Halpert, M. J. Panzer, M.G. Bawendi, V. Bulović

Alternating current thin-film electroluminescent (AC-TFEL) devices already occupy a segment of the large-area, high-resolution, flat-panel-display market. The AC-TFEL displays, which consist of a phosphor layer, such as manganese doped-zinc sulfide (ZnS:Mn), vertically sandwiched between two insulators that are contacted by electrodes, are robust, possess long lifetimes, and offer high luminance with relatively low power consumption [1], [2]. While fabrication of AC-TFEL devices has been the subject of considerable study over the past three decades, significant challenges remain. Development of multicolor displays with balanced red, green, and blue (RGB) emission has proven difficult as the most efficient red, green, and blue phosphors comprise different materials systems that require different deposition and annealing steps. Transparent AC-TFEL displays have recently been demonstrated by Sharp, Inc.; however, the processing of the phosphor to achieve transparency is difficult and has not yet been developed for phosphors other than ZnS:Mn [3].

We present a novel materials system for solution processing of the active phosphor layer in transparent AC-TFEL devices. We use colloiddally-synthesized Mn-doped nanocrystals interspersed between RF magnetron sputtered ZnS layers to demonstrate electroluminescence (EL) from a solution-deposited active layer in an AC-TFEL device fabricated at room temperature [4]. We adapt the synthesis of Thakar *et al.* to make stable ZnSe/ZnS:Mn/ZnS nanocrystals with quantum yields of $(65\pm5)\%$ [5]. As Figure 1 shows, these wide band gap host nanocrystals along with sputtered wide band-gap metal oxides (Al_2O_3 , HfO_2 , and ITO) enable transparent AC TFEL devices without additional processing steps beyond the room-temperature layer-by-layer deposition of each material set. Our devices exhibit electroluminescence from the Mn dopants at frequencies greater than 10 kHz and with voltages as low as 110 V_{pp} (See Figures 1 and 2) [4].

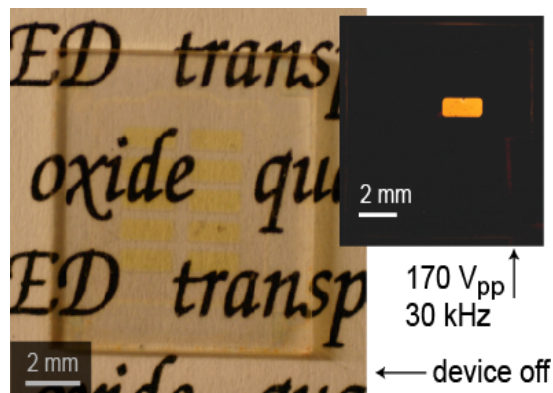


Figure 1: A photograph of a 0.5 in. x 0.5 in. glass substrate containing ten 1 mm x 2 mm AC-TFEL devices, with no bias applied. The substrate is pictured on top of printed text to demonstrate the transparency of our AC-TFEL device architecture. The inset shows the uniformity of pixel illumination (in the dark) with the device operating at 170 V_{pp} and 30 kHz.

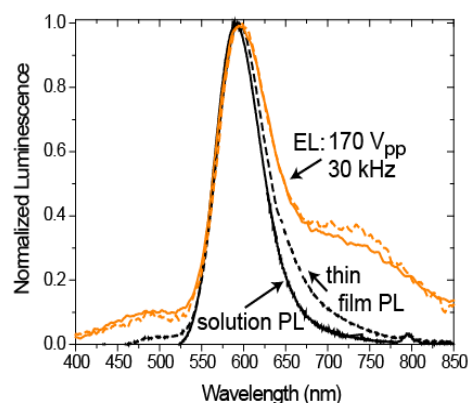


Figure 2: Electroluminescent (EL) spectra for devices with Al_2O_3 and HfO_2 insulating layers (solid and dashed orange curves, respectively). Photoluminescence (PL) spectra of the nanocrystal solution (solid gray curve) and a completed device (dashed black line). The overlap of the spectral peaks indicates that the emission is due to the Mn impurity dopants.

[1] Y. A. Ono, *Electroluminescent Displays*. Singapore: World Scientific, 1995.

[2] J.P. Keir and J.F. Wager, "Electrical Characterization of Thin-Film Electroluminescent Devices," *Annu. Rev. Mat. Sci.*, vol. 27, 1997, pp. 223-248.

[3] A. Abileah, K. Harkonen, A. Pakkala, and G. Smid. *Transparent Electroluminescent (EL) Displays*, Planar Systems, 2008.

[4] V. Wood, J.E. Halpert, M.J. Panzer, M.G. Bawendi, and V. Bulović. "AC-driven Electroluminescence from ZnSe/ZnS:Mn/ZnS Nanocrystals," *Nano Lett.* in press, 2009.

[5] R. Thakar, Y. Chen, and P.T. Snee, "Efficient Emission from Core/(Doped) Shell Nanoparticles: Applications for Chemical Sensing," *Nano Lett.*, vol. 7, no. 11, Oct. 2007., pp. 3429-3432.

Photoluminescence of CdSe/ZnS core/shell quantum dots enhanced by energy transfer from a phosphorescent donor

P.O. Anikeeva^{a,*}, C.F. Madigan^a, S.A. Coe-Sullivan^a, J.S. Steckel^b,
M.G. Bawendi^b, V. Bulović^a

^a Laboratory of Organic Optics and Electronics, Department of Electrical Engineering and Computer Science,
Massachusetts Institute of Technology, Cambridge, MA 02139, USA

^b Department of Chemistry, Massachusetts Institute of Technology, Cambridge, MA 02139, USA

Received 11 February 2006; in final form 3 April 2006

Available online 21 April 2006

Abstract

We demonstrate exciton energy transfer from a thin film of phosphorescent dye *fac* tris(2-phenylpyridine) iridium ($\text{Ir}(\text{ppy})_3$) to a monolayer of colloidal CdSe/ZnS core/shell quantum dots (QDs). The energy transfer is manifested in time-resolved photoluminescence (PL) measurements as elongation of the QD PL time constant from 40 to 400 ns, and a concomitant 55% increase of time-integrated QD PL intensity. The observed PL dynamics are shown to be dominated by exciton diffusion within the $\text{Ir}(\text{ppy})_3$ film to the QD layer.

© 2006 Elsevier B.V. All rights reserved.

Over the past several years the optical and electronic properties of colloidal synthesized nanocrystals [1], or quantum dots (QDs), of CdSe have been extensively studied with the aim of using QD films in solid state opto-electronic devices. Efficient exciton generation in CdSe QDs suggests use of nanocrystal composite films in photovoltaic cells [2], while high luminescence quantum yields and tunability of QD emission wavelengths over the entire visible spectrum suggests QD film use in light emitting devices (LEDs) [3]. These developments are a consequence of advances in colloidal QD synthesis that allow for increased control over the shape, size, and emission wavelength of nanocrystals [4], and the development of methods for forming QD thin films of controlled structure and composition [5]. Utilizing these advances, in the present Letter we fabricate hybrid organic thin film/QD structures which demonstrate triplet exciton energy transfer (ET) from a thin film of phosphorescent molecules to a monolayer of CdSe/ZnS core/shell QDs. Triplet exciton harvesting and transfer to an efficient lumino-

phore has been previously used in advancing organic light emitting device (OLED) technology [6], and has the potential to similarly benefit the emerging field of quantum-dot-LEDs (QD-LEDs) [7].

OLEDs based on phosphorescent materials exhibit high quantum efficiencies [8]. For example, organic phosphors containing $d^6 \text{Ir}^{3+}$ complexes, such as the *fac* tris(2-phenylpyridine) iridium ($\text{Ir}(\text{ppy})_3$) that is used in this Letter (see inset of Fig. 1) [9,10], show record efficient electro-phosphorescence at room temperature with external quantum efficiencies as high as 19% [11]. In these compounds spin-orbit coupling leads to the mixing of the spin-singlet and spin-triplet excited states [10,12], which enables the radiative relaxation of the triplet-state and leads to a fast phosphorescent decay ($<1 \mu\text{s}$) and high phosphorescence efficiency that benefits OLED performance.

In QDs, the presence of transition metal atoms, such as Cd, leads to electron-hole exchange interaction and spin-orbit coupling [13] that mix the electron and hole spin states. In CdSe QDs electron spin-mixing results in a non-emissive lowest energy exciton, so called 'dark exciton' [14], which is between 0.13 meV (as in CdSe bulk) and 12.5 meV (for the smallest QD with few nm diameter)

* Corresponding author.

E-mail address: anikeeva@mit.edu (P.O. Anikeeva).

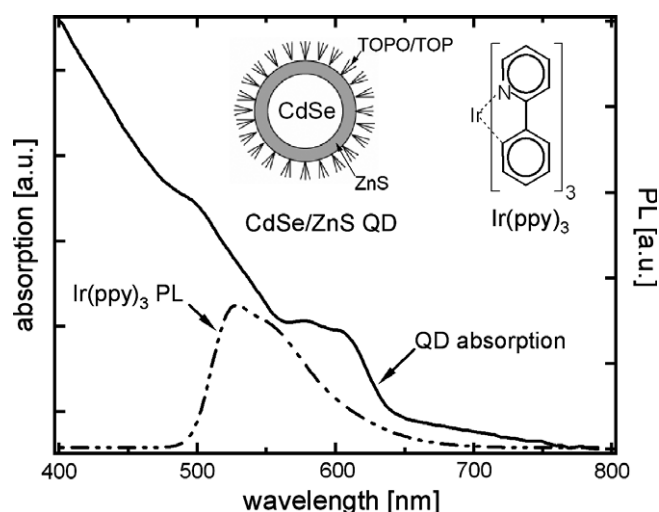


Fig. 1. Overlap between CdSe/ZnS QD absorption (solid line) and Ir(ppy)₃ emission (dash-dot-dot) spectra suggests energy transfer from Ir(ppy)₃ to QDs. (Note. QD absorption spectrum was obtained by the direct measurement in a thin film, consequently it exhibits a red tail due to the scattering of the organic ligands in a solid film.) Inset: Schematic drawing of a ZnS overcoated CdSe QD and Ir(ppy)₃ structural formula.

below the emissive excitonic state [15]. Thermal mixing of the dark and emissive exciton results in a room temperature QD radiative lifetime in the range from 3 to 30 ns (depending on the QD core/shell structure, size distribution, and the fidelity of the organic capping layer), and luminescence efficiencies exceeding 80% in solution [16,17].

Since QDs are efficient lumophores and Ir(ppy)₃ is an efficient triplet exciton harvester, in this Letter we consider energy transfer (ET) from Ir(ppy)₃ to CdSe/ZnS core/shell QDs in order to enhance the luminescence intensity of QD lumophores. Overlap of Ir(ppy)₃ luminescence and QD absorption spectra suggests the possibility of efficient ET (Fig. 1). Our Letter follows earlier experiments that investigated Förster ET to CdSe/ZnS QDs from both fluorescent organic hosts as well as from inorganic substrate layers [18,19]. QDs have proven themselves as efficient exciton donors in energy transfer experiments with various organic dyes and bioorganic molecules [20,21]; however, there remains debate in the literature over the demonstration of ET from an organic donor to CdSe/ZnS core/shell QD (see e.g. [22]). In contrast, the present Letter definitively confirms that CdSe/ZnS core/shell QDs can efficiently accept excitons from an organic donor by demonstrating ET of triplet excitons from a phosphorescent dye to QD lumophores.

We fabricated three thin film structures: sample I is a 40 nm thick film of 10% Ir(ppy)₃ doped into 4,4'-N,N'-dicarbazole-biphenyl (CBP) thermally evaporated onto a glass substrate. Sample II is a monolayer of CdSe/ZnS QDs (7 nm QD diameter) printed [23] onto a glass substrate. Finally, sample III is a hybrid structure consisting of a monolayer of CdSe/ZnS QDs printed onto a 40 nm thick film of 10% Ir(ppy)₃ in CBP on glass.

Comparing the PL signatures of the three samples we observe a $21 \pm 4\%$ decrease of Ir(ppy)₃ time-integrated PL intensity in sample III as compared to sample I and a concomitant $55 \pm 5\%$ increase in CdSe/ZnS QD film PL intensity in sample III as compared to sample II (see Fig. 2). The change in PL is calculated by numerically decomposing the sample III spectrum into CdSe/ZnS QD and Ir(ppy)₃ components. The PL change suggests ET from the Ir(ppy)₃ film to the QD monolayer. We note that simple reabsorption of Ir(ppy)₃ luminescence by the QD film does not account for the observed PL change since the 7 nm thick QD monolayer has very weak absorption ($<1.5\%$) over the Ir(ppy)₃ PL spectrum. Assuming a QD PL efficiency on the order of 0.1 (typical of QD films), we find that reabsorption of Ir(ppy)₃ photons by the QD layer can lead to small QD PL flux increase of at most 0.0015 times the Ir(ppy)₃ photon flux, or a roughly three orders of magnitude smaller than the observed QD intensity. (To provide an upper limit on the reabsorption effect, we assume all of the Ir(ppy)₃ flux is directed through the QD film.) Consequently, reabsorption does not significantly contribute to the observed increase in QD PL in sample III. (Note that because the film thicknesses are much less than the wavelengths of the emitted light, and the refractive index contrasts between the layers are small, optical cavity effects are not expected to be significant.)

Data from time-resolved PL measurements are shown in Fig. 3. The PL of CdSe/ZnS QDs in sample II (data set E) exhibits two time constants with a shorter time constant of $\tau_1^{\text{QD}} = 10$ ns and a longer time constant of $\tau_2^{\text{QD}} = 40$ ns. The Ir(ppy)₃ PL decay also exhibits bi-exponential behavior, with a dominant time constant of $\tau_{\text{Ir(ppy)}_3} = 610$ ns (as obtained from data set A). In sample III, however, the QD PL decay (data set D) is substantially elongated, leading to a longer time constant of $\tau_{2,\text{III}}^{\text{QD}} = 500$ ns, which is

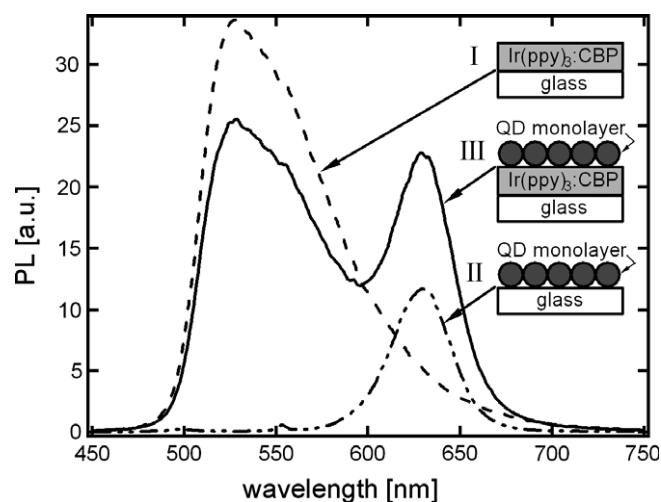


Fig. 2. Time-integrated PL spectra of samples I, II and III. All measurements were obtained at the same excitation source power of $\lambda = 395$ nm light. The PL spectrum of sample III can be constructed from a linear superposition of the PL spectra of samples I and II.

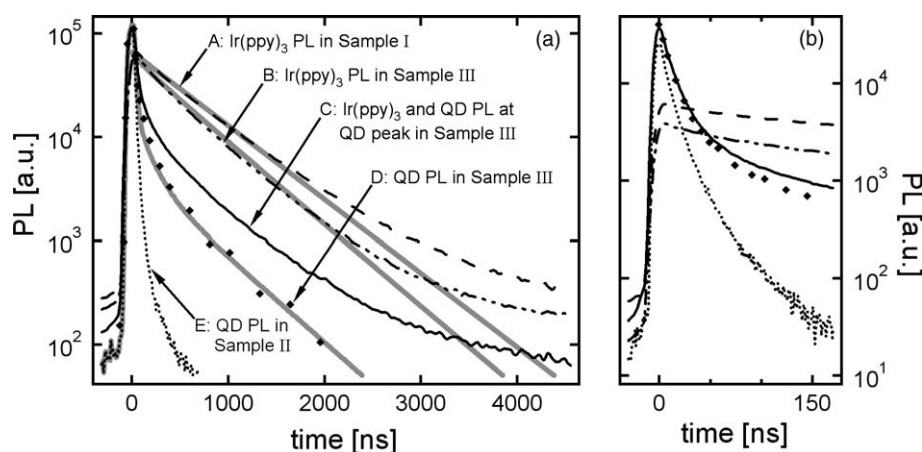


Fig. 3. Time resolved PL measurements for samples I, II and III, performed over (a) a 5000 ns time window and (b) a 500 ns time window (first 200 ns shown). The black lines and dots represent the experimental measurements, and the thick grey lines represent numerical fits using the proposed diffusion model. To obtain data sets A and B, the sample PL was integrated over the wavelength range of $\lambda = 511$ nm to $\lambda = 568$ nm, to yield in each case the time dependence of the Ir(ppy)₃ PL. Similarly, to obtain data sets C and E, a wavelength range of $\lambda = 600$ nm to $\lambda = 656$ nm was used. Data set C therefore reflects the intensity of combined Ir(ppy)₃/QD PL near the QD PL peak. Data set E reflects the intensity of solely the QD PL. To obtain data set D, the intensity due to the Ir(ppy)₃ PL was subtracted from C to yield just the QD PL intensity in sample III. Note that the grey fit lines assume a single exponential time decay for the Ir(ppy)₃, and so are only expected to fit the Ir(ppy)₃ at early times (where the single exponential decay dominates).

identical to the dominant time constant of the Ir(ppy)₃ PL from the same sample (data set B), strongly suggesting that this ‘delayed’ QD PL is due to energy transfer of Ir(ppy)₃ excitons to the QD film.

An investigation of the first 200 ns of QD PL (Fig. 3b) reveals a slight increase in the initial PL intensity and a small increase of the short time constant, yielding $\tau_{1, \text{III}}^{\text{QD}} = 12$ ns. Note that in Fig. 3, the data are obtained by integrating the PL spectra over the wavelength ranges specified in the figure caption. Furthermore, the QD PL decay for sample III (data set D) is obtained by subtracting the Ir(ppy)₃ PL spectrum from the total signal, as illustrated in Fig. 4, and then integrating the difference signal over the specified wavelength range. We again note that the time-dependent contribution of reabsorption to the

QD PL is at most 0.0015 times the Ir(ppy)₃ flux intensity (obtained from sample I). Therefore, for all times reabsorption contribution is at most 3% of the observed QD PL signal.

Since reabsorption does not contribute significantly to the QD PL intensity in sample III, the observed QD PL enhancement and elongation of QD PL lifetime can be attributed to exciton energy transfer from Ir(ppy)₃ molecules to the QD monolayer. For quantitative analysis of the data, we note that the observed PL time dependence (Figs. 3 and 4) is shaped by four physical processes that govern exciton dynamics in the Ir(ppy)₃:CBP film: Ir(ppy)₃ exciton radiative decay, non-radiative decay, ET to the QD film, and diffusion. The two decay mechanisms combine to determine the observed radiative lifetime of 610 ns and a

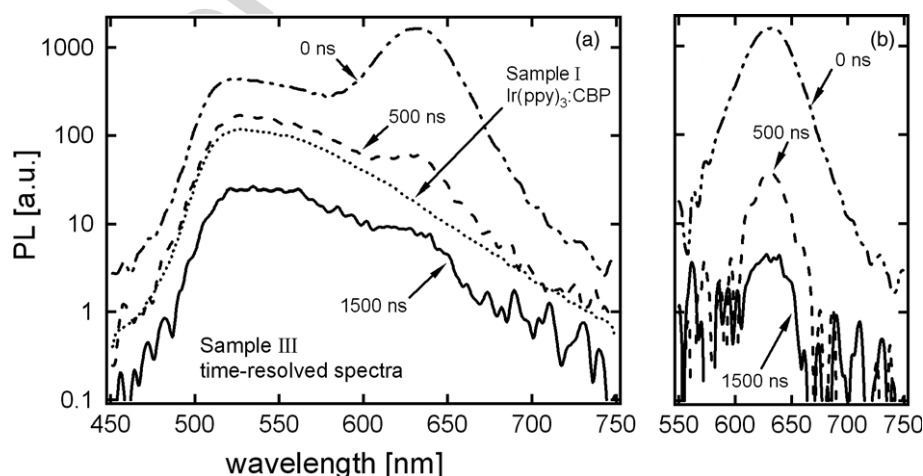


Fig. 4. (a) PL spectra of sample III are shown at times $t = 0$ ns (dash-dot-dot), $t = 500$ ns (dashed line), $t = 1500$ ns (solid line) after excitation. Ir(ppy)₃ integrated PL spectrum (dotted line) is shown for comparison (not to scale). (b) QD PL in sample III obtained by subtracting scaled Ir(ppy)₃ spectrum from the PL of sample III is shown at $t = 0$ ns (dash-dot-dot), $t = 500$ ns (dashed), $t = 1500$ ns (solid) after excitation.

PL quantum efficiency of $\sim 15\%$ (as calculated from optimized electroluminescence efficiencies of 12% doped Ir(ppy)₃:CBP OLEDs [24]). The ET mechanism leads to the observed quenching of the Ir(ppy)₃ PL and the associated enhancement of the QD PL, and capturing the Ir(ppy)₃ excitons that are closest to the QD film. Finally, the diffusion mechanism induces a net flow of Ir(ppy)₃ excitons towards the QD film, due to depletion by ET of Ir(ppy)₃ excitons near the QD interface.

To numerically model the combined processes we model the ET mechanism as an instant energy transfer of any Ir(ppy)₃ exciton that is within distance, L_{ET} , from the QD film. In this model the dynamics of the ET process is controlled entirely by Ir(ppy)₃ exciton diffusion, which determines the rate at which excitons are supplied to the region within L_{ET} of the QD film.

A reasonable value for L_{ET} is determined by considering the possible ET mechanisms. In the case of ET by correlated electron exchange, a mechanism also known as Dexter transfer [25], the exciton capture region consists of a single Ir(ppy)₃ layer adjacent to QDs, since the transfer rate falls off exponentially with distance, reducing to negligible the ET contributions from all the more distant molecular layers. Since the Ir(ppy)₃ molecule is on the order of 1 nm in extent, then we estimate that $L_{ET} = 1$ nm for Dexter energy transfer.

In the case of resonant ET, a mechanism also known as Förster transfer, the capture region can be larger. For Förster transfer, the rate of ET between a donor (D) and an acceptor (A), is given by [26]

$$K_{D \rightarrow A} = \frac{1}{\tau} \left(\frac{R_F}{R} \right)^6 \quad (1)$$

where R is the distance between the donor and the acceptor, τ is the donor lifetime, and, R_F is a Förster radius

$$R_F^6 \equiv \frac{9}{8\pi} \frac{c^4}{n^4} \kappa^2 \eta_D \int \frac{S_D(\omega) \sigma_A(\omega)}{\omega^4} d\omega \quad (2)$$

where c is the speed of light in vacuum, n is the index of refraction of the medium, κ is an orientational factor, η_D is the donor PL quantum efficiency, S_D is the donor emission spectrum (normalized to integrate over frequency to unity), and σ_A is the acceptor absorption cross-section.

We calculate $R_F = 4.1$ nm from (2) by inserting the donor Ir(ppy)₃ PL and acceptor QD absorption spectra shown in Fig. 1, setting $n = 1.7$ and $\kappa^2 = 2/3$ (which averages the result over randomly oriented donor and acceptor dipoles), and using $\eta_D = 0.15$ (as estimated above). (Note. We use $n = 1.7$ characteristic of organic thin films to obtain an upper bound on R_F . Locally the refractive index could be higher due to the higher QD index, of $n \sim 2.1$, which would lead to a lower R_F value.) This R_F value is roughly equal to the center-to-center distance between a QD and an adjacent Ir(ppy)₃ molecule, i.e. 3.5 nm (half the QD diameter) + 0.5 nm (half the extent of the Ir(ppy)₃ molecule) = 4.0 nm. We, therefore, expect that Ir(ppy)₃-to-QD Förster ET is dominated by nearest neighbor trans-

fers. However, it is worth noting that the total rate of energy transfer from a single organic molecule to a QD layer should be integrated over all of the dots in the QD layer. This calculation yields a total transfer rate that scales as R^{-4} [27]. For a hexagonally close packed QD monolayer, the total rate is given by

$$K_{D \rightarrow AL} = \frac{1}{\tau} \frac{R_F^6}{2a^2 R^4} = \frac{1}{\tau} \frac{D_F^4}{R^4} \quad (3)$$

where a is the radius of the QD. Using the values for a and R_F , we obtain $D_F = 3.7$ nm.

Given that as noted above the transfer distance between nearest neighbors is just 4.0 nm, we conclude, as expected from the R_F calculation, that transfer is dominated by the layer of donors in immediate contact with the QD layer, and thus we set $L_{ET} = 1$ nm. (We note that reabsorption, Förster, and Dexter are the most commonly proposed ET mechanisms and are, hence, the mechanisms focused on in this Letter. The following analysis, however, is unchanged even for other ET mechanisms, so long as L_{ET} remains of the order of 1 nm.)

We model the emission, diffusion, and ET processes in Ir(ppy)₃ through a differential equation governing the time, t , and space, x , dependence of the exciton population, $n(x, t)$, in the Ir(ppy)₃ film:

$$\frac{d}{dt} n(x) = -\frac{1}{\tau} \left(-n(x) + L_D^2 \frac{d^2}{dx^2} n(x) \right), \quad 0 \leq x < L - L_{ET} \quad (4)$$

where L is the total thickness of the Ir(ppy)₃ film and $x = L$ is the Ir(ppy)₃/QD interface. For the film region comprising $x \geq L - L_{ET}$, we assume that any non-zero value of n is instantly lost due to ET to QD film. We further assume that initially, at $t = 0^-$, the film is uniformly excited and a moment later, at $t = 0^+$, for $x \geq L - L_{ET}$, all of the exciton concentration is lost to ET. (Because the film absorbs less than 20% of the incident excitation light, the error incurred in assuming uniform excitation is small.) Subsequently, the system evolves following Eq. (4) with diffusion current through the $x = L - L_{ET}$ plane comprising the Ir(ppy)₃ excitons lost to ET due to diffusion. We perform a discrete time numerical calculation of two functions of this system: the number of emitted photons per time step, $n_{PL}(t)$, and the number of energy transferred excitons per time step, $n_{ET}(t)$. Setting $L = 40$ nm, $L_{ET} = 1.0$ nm and $\tau = 610$ ns we find that for a 21% Ir(ppy)₃ quenching fraction, we obtain $L_D = 8.1$ nm. In Fig. 3 we plot the associated fits (grey lines). The $n_{PL}(t)$ function provides the fit to the Ir(ppy)₃ PL in sample III. To fit the QD PL in sample III, we scale the $n_{ET}(t)$ function by 0.6 relative to the Ir(ppy)₃ PL curve (to reflect the reduced PL efficiency of QDs as compared to Ir(ppy)₃ and the spectral collection window) and add to it the QD PL observed in sample II, which provides the PL due to direct excitation of the QD film. For comparison, a single exponential decay with $\tau = 610$ ns is plotted besides Ir(ppy)₃ PL of sample I (data set A).

The model generated PL time dependence is consistent with both the Ir(ppy)₃ and QD time dependent PL intensity from sample III. For the Ir(ppy)₃ PL (data set B), the deviations mainly occur at longer times ($t > 2000$ ns) where the single exponential character of the intrinsic Ir(ppy)₃ PL is no longer valid. For the QD PL (data set D), the fit agrees to within the experimental error at all times. The fit suggests that the QD PL is initially due to both PL of QDs excited by incident light and PL of QDs excited by ET from Ir(ppy)₃. At later times ($t > 150$ ns) the QD PL dynamics are due entirely to the Ir(ppy)₃ exciton diffusion process. We also note that the value of $L_D = 8.1$ nm obtained from the fit is comparable to exciton L_D values measured in other molecular organic thin film systems [28,29].

By considering the scaling factor required to fit the QD PL in sample III (data set D) we can calculate the PL efficiency of the QD film. Due to the measurement windows utilized in generating the intensity profiles in Fig. 3, the Ir(ppy)₃ PL curve (comprising the signal between $\lambda = 511$ nm and $\lambda = 568$ nm) reflects 0.59 of the total Ir(ppy)₃ spectral intensity, while the QD PL curve (comprising the signal between $\lambda = 600$ nm and $\lambda = 656$ nm) reflects 0.86 of the total QD spectral intensity. Consequently, transferring Ir(ppy)₃ excitons to the QD layer should yield a corresponding increase in QD PL curve equal to $0.86/0.59 = 1.46$ times the loss in Ir(ppy)₃ photons for equal quantum efficiencies. Since we fit our QD PL data by scaling the $n_{ET}(t)$ curve down by 0.6 relative to the Ir(ppy)₃ fit, this implies the quantum efficiency, η_{QD} , of the QD film is $0.6/1.46 = 0.41$ times the Ir(ppy)₃ quantum efficiency, yielding $\eta_{QD} = 0.41 \times 0.15 = 0.06$, which is consistent with typical thin film QD PL efficiencies.

Finally, we note that the model employed here is only weakly dependent on L_{ET} , with the main effect being that as L_{ET} increases, L_D decreases because a larger fraction of the Ir(ppy)₃ photons are instantly quenched and therefore less diffusion is required to obtain the desired 21% total quench. In the rather extreme case where $L_{ET} = 5$ nm, the data can still be roughly fit by setting $L_D = 4.0$ nm, yielding a corresponding calculation of $\eta_{QD} = 0.12$. Indeed, we find that this model produces a similar time dependence to the Ir(ppy)₃ PL quench and QD PL enhancement for a wide range of L_{ET} values. Consequently, on the basis of only the experiments shown here, it is not possible to conclusively identify the dominant ET mechanism (e.g., Dexter or Förster).

In conclusion, we report an increase in the PL intensity and an increase in PL lifetime for a CdSe/ZnS QD thin film due to exciton ET from a phosphorescent molecular organic film. The observed ET dynamics are self-consistently explained by a simple numerical model that combines exciton diffusion in the Ir(ppy)₃ film with short-range ET from Ir(ppy)₃ to the QD layer. The demonstrated transfer of triplet excitons to luminescent QDs could benefit the development of QD optoelectronic technologies, such as QD-LEDs.

1. Experimental

Thermal deposition of the organic films was performed at a rate of ~ 0.2 nm/s and a chamber pressure of $< 2 \times 10^{-6}$ Torr. CdSe/ZnS QDs were prepared using a procedure similar to that described in [4]. Prior to the thin film deposition the glass substrates were cleaned by a multiple step solvent cleaning process using Micro 90, acetone and isopropanol. To prevent exposure to an ambient environment during measurements, samples were packaged inside a nitrogen glovebox using a glass coverslip and UV-curing epoxy.

In the time resolved photoluminescence measurement the excitation source was $\lambda = 395$ nm wavelength laser light with 200 fs pulse width and 100 kHz repetition rate obtained by frequency doubling the output of a Coherent Ti-Sapphire laser. Photoluminescence was collected with a Hamamatsu C4780 picosecond fluorescence lifetime system consisting of a C4334 streak camera and a C5094 spectrograph. The light collection scheme consisted of two lenses, one collecting luminescence from a sample and the other focusing it onto a detector slit. Laser beam was incident on the sample at approximately 60° angle away from the normal, and the collecting lens was aligned normal to the sample. All three samples were excited with a constant laser power of 33 mW/cm^2 without altering the collection geometry, allowing a relative comparison of PL intensities. All measurements were performed at room temperature.

Acknowledgements

The authors are grateful for financial support of the MIT Institute for Soldier Nanotechnologies, NSF Materials Research Science and Engineering Center at MIT, and the Presidential Early Career Award for Scientists and Engineers. PA would like to thank Steven E. Kooi for his assistance with time-resolved PL measurements.

References

- [1] C.B. Murray, D.J. Norris, M. Bawendi, J. Am. Chem. Soc. 115 (1993) 8706.
- [2] W.U. Huynh, J.J. Dittmer, A.P. Alivisatos, Science 295 (2002) 2425.
- [3] S. Coe, W.-K. Woo, M.G. Bawendi, V. Bulovic, Nature (London) 420 (2002) 800.
- [4] B.O. Dabbousi, J. Rodriguez Viejo, F.V. Miculec, J.R. Heine, H. Mattoussi, R. Ober, K.F. Jensen, M.G. Bawendi, J. Phys. Chem. B 101 (1997) 9463.
- [5] S. Coe-Sullivan, J.S. Steckel, W.-K. Woo, M.G. Bawendi, V. Bulovic, Adv. Funct. Mater. 15 (2005) 1117.
- [6] M.A. Baldo, M.E. Thompson, S.R. Forrest, Nature (London) 403 (2000) 750.
- [7] S. Coe-Sullivan, J.S. Steckel, L. Kim, M.G. Bawendi, V. Bulovic, Proc. SPIE 5739 (2005) 108.
- [8] M.A. Baldo, D.F. O'Brien, M.E. Thompson, S.R. Forrest, Phys. Rev. B 60 (1999) 14422.
- [9] K. Dedeian, P.I. Djurovich, F.O. Garces, G. Carlson, R.J. Watts, Inorg. Chem. 30 (1991) 1685.

- [10] S. Lamansky, P. Durovich, D. Murphy, F. Abdel-Razzaq, H.-E. Lee, C. Adachi, P.E. Burrows, S.R. Forrest, M. Thompson, *J. Am. Chem. Soc.* 123 (2001) 4304.
- [11] C. Adachi, M.A. Baldo, M.E. Thompson, S.R. Forrest, *J. Appl. Phys.* 90 (2001) 5048.
- [12] M.A. Baldo, D.F. O'Brien, Y. You, A. Shoustikov, S. Sibley, M.E. Thompson, S.R. Forrest, *Nature (London)* 395 (1998) 151.
- [13] P.W. Atkins, R.S. Friedman, *Molecular Quantum Mechanics*, Oxford University Press, Oxford, 1997.
- [14] M. Nirmal, D.J. Norris, M. Kuno, M.G. Bawendi, A.L. Efros, M. Rosen, *Phys. Rev. Lett.* 75 (1995) 3728.
- [15] A.L. Efros, M. Rosen, *Annu. Rev. Mater. Sci.* 30 (2000) 475.
- [16] M.A. Hines, P. Guyot-Sionnest, *J. Phys. Chem.* 100 (1996) 468.
- [17] P. Reiss, J. Bleuse, A. Pron, *Nano Lett.* 2 (2002) 781.
- [18] M. Anni, L. Manna, R. Cingolani, D. Valerini, A. Creti, M. Lomascolo, *Appl. Phys. Lett.* 85 (2004) 4169.
- [19] M. Achermann, M.A. Petruska, S. Kos, D.L. Smith, D.D. Koleske, V.I. Klimov, *Nature (London)* 429 (2004) 642.
- [20] A.R. Clapp, I.L. Medintz, J.M. Mauro, B.R. Fisher, M.G. Bawendi, H. Mattoussi, *J. Am. Chem. Soc.* 126 (2004) 301.
- [21] I.L. Medintz, A.R. Clapp, H. Mattoussi, E.R. Goldman, B.M. Fisher, J.M. Mauro, *Nat. Mater.* 2 (2003) 630.
- [22] A.R. Clapp, I.L. Medintz, B.R. Fisher, G.P. Anderson, H. Mattoussi, *J. Am. Chem. Soc.* 127 (2005) 1242.
- [23] S. Coe-Sullivan, PhD Thesis, Department of Electrical Engineering and Computer Science, Massachusetts Institute of Technology, 2005.
- [24] M.A. Baldo, S. Lamansky, P.E. Burrows, M.E. Thompson, S.R. Forrest, *Appl. Phys. Lett.* 75 (1999) 4.
- [25] M. Pope, C.E. Swenberg, *Electronic Processes in Organic Crystals*, Oxford University Press, Oxford, 1982.
- [26] Th. Förster, *Annalen der Physik* 6 (1948) 55.
- [27] H. Kuhn, *J. Chem. Phys.* 53 (1) (1970) 101.
- [28] E.B. Namdas, A. Ruseckas, I.D.W. Samuel, S.-C. Lo, P.L. Burn, *Appl. Phys. Lett.* 86 (2005) 091104.
- [29] N. Matsusue, S. Ikame, Y. Suzuki, H. Naito, *Appl. Phys. Lett.* 97 (2005) 123512.

NiO as an Inorganic Hole-Transporting Layer in Quantum-Dot Light-Emitting Devices

Jean-Michel Caruge,[†] Jonathan E. Halpert,[†] Vladimir Bulović,^{*,‡} and Mouni G. Bawendi^{*,†}

*Department of Chemistry, Massachusetts Institute of Technology,
77 Massachusetts Avenue, Cambridge, Massachusetts 02139, Laboratory of Organic
Optics and Electronics, Department of Electrical Engineering and Computer Science,
Massachusetts Institute of Technology, 77 Massachusetts Avenue,
Cambridge, Massachusetts 02139*

Received October 2, 2006

ABSTRACT

We demonstrate a hybrid inorganic/organic light-emitting device composed of a CdSe/ZnS core/shell semiconductor quantum-dot emissive layer sandwiched between p-type NiO and tris-(8-hydroxyquinoline) aluminum (Alq₃), as hole and electron transporting layers, respectively. A maximum external electroluminescence quantum efficiency of 0.18% is achieved by tuning the resistivity of the NiO layer to balance the electron and hole densities at quantum-dot sites.

Advances in the chemical synthesis and processing of colloidal semiconductor quantum dots (QDs) combined with the unique emissive properties of these inorganic nanomaterials have triggered the development of QD light-emitting devices (QD-LEDs). Recent works have focused on the choice of adequate electron- and hole-transporting layers to realize high-performance QD-LEDs emitting in the near-infrared and visible spectral ranges.^{1–5} To date, the most efficient QD-LED reported⁵ in the visible spectrum was a hybrid QD/organic device composed of a monolayer of closely packed CdSe/ZnS core/shell QDs sandwiched between organic *N,N'*-diphenyl-*N,N'*-bis(3-methylphenyl)-1-1'-biphenyl-4,4'-diamine (TPD) and tris(8-hydroxyquinoline) aluminum (Alq₃) hole and electron transporting layers, respectively. At video brightness, the external electroluminescence (EL) quantum efficiency (η_{EL}) of these devices was $\sim 2\%$.⁵ To be applicable in display and lighting applications, QD-LEDs not only must be efficient but must also have long operating lifetimes. The lifetime of a typical ITO/TPD/QD/Alq₃/Mg:Ag/Ag device is limited, as in OLEDs, by the degradation of the organic layers under moisture and oxygen and the instability of the metal contacts.^{6,7}

In this work, we explore the possibility of replacing the TPD film with a high-band-gap (> 3 eV) inorganic hole-

transporting layer that is chemically and electrically more stable. NiO has been selected from band-offset considerations (relative to CdSe QDs), ease of deposition, and its chemical compatibility with the CdSe QDs. Additionally, early studies have shown that transparent p-type NiO thin films can be obtained by near-room-temperature reactive sputtering of NiO or Ni targets and can be used as hole-transporting/injecting layers in electro-optical devices.^{8–10} The QD-LED structure we investigate is sketched in the band diagram in Figure 1a with a NiO hole-transporting layer and an Alq₃ electron-transporting layer sandwiching the QD lumophores.

The quenching of QD electroluminescence by the high density of free charge carriers in NiO and the balance^{11–14} of electron and hole currents are two crucial challenges that have to be overcome in order to build efficient NiO QD-LEDs.

We first address the quenching mechanism by observing that photoluminescence intensities of single QDs deposited onto resistive ($\rho \approx 1 \text{ } \Omega \cdot \text{cm}$) NiO thin films remain high, in contrast to quenched photoluminescence of single QDs deposited onto highly conductive ($\rho \approx 5 \times 10^{-4} \text{ } \Omega \cdot \text{cm}$) NiO thin films. The same observation was made for a 30-nm-thick close-packed QD film deposited by spin-coating onto resistive and highly conductive NiO. These observations are consistent with early theoretical and experimental works,^{15–19} which demonstrated that photoluminescence quenching of organic and inorganic lumophores by a conductive dielectric via an energy-transfer process can be tuned by controlling

* Corresponding authors. E-mail: bulovic@mit.edu; mgb@mit.edu.

[†] Department of Chemistry.

[‡] Laboratory of Organic Optics and Electronics, Department of Electrical Engineering and Computer Science.

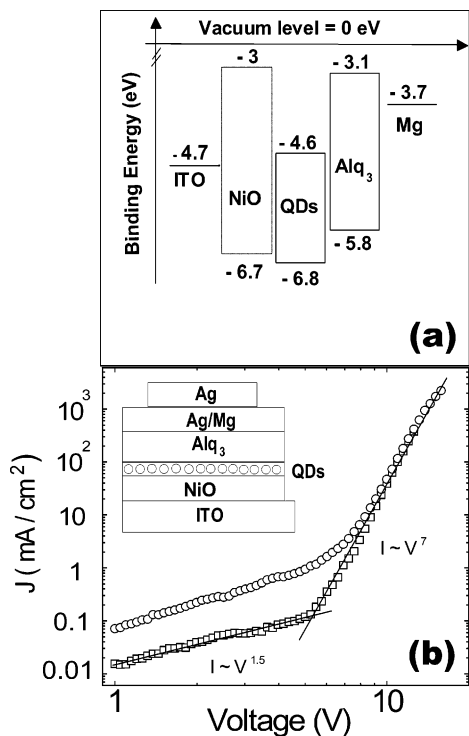


Figure 1. (a) Proposed band diagram of a NiO QD-LED. (b) Forward-biased current–voltage characteristics for NiO QD LEDs constructed with high-resistivity (open squares) and low-resistivity (open circles) NiO HTLs. The contact area is 0.78 mm² for both devices. Inset: schematic representation of the QD-LED structure.

the chromophore–dielectric distance and by tuning the electrical permittivity of the dielectric, which in our study changes with the hole density in the NiO layer. In the case of EL, upon an applied voltage, accumulation of holes around the QD layer, due to the presence of energy barriers, will induce fluctuations in the local hole density, which could affect the quenching of the EL from QDs. However, we believe that the -0.1 and 1 eV band offsets (Figure 1a) at the NiO/QD and QD/Alq₃ interfaces should easily facilitate hole injection into the QDs and Alq₃ (in forward bias) and that a drastic change in the local hole density is unlikely to occur.

Second, we show below that the control of the oxygen concentration inside the sputtering chamber during the sputtering step enables us to accurately tune the resistivity of the NiO films and improve the charge balance inside our devices.

In the following sections, we start by describing the fabrication process of the NiO QD-LEDs. We then show that space-charge-limited conduction is the dominant charge conduction mechanism and demonstrate that η_{EL} up to 0.18% can be achieved in our devices.

The NiO QD-LEDs were fabricated as follows: Prior to the deposition of the NiO thin films, ITO precoated (150 nm thick) glass substrates (with sheet resistance of 30 Ω per square) were cleaned via sequential ultrasonic rinses in detergent solution, deionized water, and acetone and then boiled in isopropanol for 5 min. After cleaning, the glass substrates were dried in nitrogen and exposed to UV-ozone

to eliminate any adsorbed organic materials. They were then inserted into a nitrogen glove box, which is connected to a sputtering and evaporation chamber via a high vacuum transfer line. In the sputtering chamber, a 30-nm-thick NiO thin film was deposited by reactive RF magnetron sputtering of a NiO target in an Ar/O₂ gas mixture. For our most efficient QD-LED described in this paper, the base pressure before sputtering was 10^{-7} Torr, the RF power was fixed at 200 W, the plasma pressure was 6 mTorr, and the ratio between the O₂ and Ar gas flow rates was 2.5%, which, with our sputtering geometry, resulted in a NiO deposition rate of 0.03 nm/s. With the above deposition parameters, the NiO thin films showed p-type conductivity with resistivity of $\rho = 5 \Omega \cdot \text{cm}$ (sheet resistance of 2 M Ω per square), and optical transmission of 80% at $\lambda = 625$ nm (center of the QD emission peak). The resistivity of the p-type NiO thin films is tuned accurately by varying the ratio between the O₂ and Ar flow rates: higher oxygen concentration in the sputtering chamber gives lower resistivities. For instance, increasing the oxygen to argon gas ratio from 2.5% to 10% decreases the resistivity of NiO films from $\rho = 5 \Omega \cdot \text{cm}$ to $\rho = 5 \times 10^{-4} \Omega \cdot \text{cm}$. AFM characterizations of the ITO/NiO surface reveals a rms surface roughness of ~ 2 nm. The surface roughness comes mainly from the ~ 150 -nm-thick commercial ITO films. Indeed, AFM images of a 30-nm-thick NiO thin film sputtered (with the same deposition parameters) onto a flat glass substrate reveal an rms surface roughness of 0.3 nm. Of paramount importance, the NiO films were also highly stable in air and in the presence of the organic solvents used during chemical processing of the QDs.

The glass/ITO/NiO substrates were transferred back into the glove box where they were coated with a 20-nm-thick layer of CdSe/ZnS core/shell QDs that was spun-cast out of chloroform. The thickness of the spun-cast QD films can be tuned by varying the QD concentration in chloroform and/or the spin speed during the spin-coating process. The substrates were then transferred, without exposure to air, into the evaporation chamber, and a 40-nm-thick Alq₃ electron-transporting layer was evaporated at 10^{-6} Torr, at a deposition rate of ~ 0.2 nm/s. A 100-nm-thick Ag/Mg (1/10 by weight) and 30-nm-thick Ag electron-injecting electrode were then evaporated through a shadow mask, forming 1-mm-diameter circular electrodes. The freshly made QD-LEDs were removed from the integrated deposition system, without packaging, and immediately tested in air.

Two sets of devices, with $\rho_1 = 5 \Omega \cdot \text{cm}$ (high-resistivity NiO) and $\rho_2 = 10^{-2} \Omega \cdot \text{cm}$ (low-resistivity NiO), were investigated in this paper. Typical forward biased current–voltage (I – V) characteristics for the two sets of devices (measured with respect to the grounded Ag cathode) are plotted in Figure 1b. The open square and open circle curves are typical I – V curves for the high- and low-resistivity devices, respectively. For both sets of devices, $J \propto V^n$ with $1 < n < 1.5$ below ~ 6 V and $6 < n < 7$ at higher voltages. Here, n is the signature of the charge conduction mechanism and is related to the temperature and to the density and energy distribution of trap states in the organic or inorganic

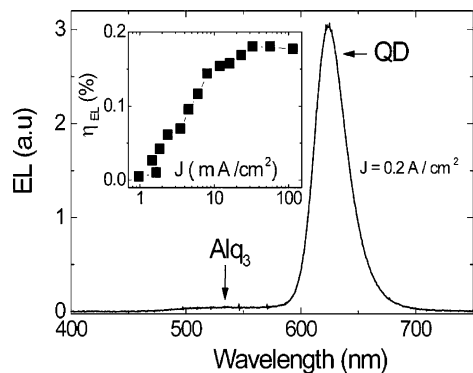


Figure 2. EL spectrum of a NiO QD-LED taken from a high-resistivity NiO device at a current density of 200 mA/cm². More than 95% of the EL originates from QD luminescence. The resistivity of the NiO thin film is 5 Ω·cm. The fwhm of the QD emission peak is 30 nm. The spectral shoulder at $\lambda = 530$ nm is due to Alq₃ emission. Inset: external electroluminescence quantum efficiency vs current density for the same NiO QD-LED.

materials. These I – V curves are consistent with previous reports of trap-assisted space-charge-limited conduction in both CdSe/ ZnS⁴ close packed films and OLEDs.^{20,21} The turn-on voltage, defined as the minimum voltage for which EL can be detected from the devices with an Ocean Optics (SD 2000) spectrometer, is between 6 and 7 V for both sets of devices. The maximum steady-state current densities achieved in the high- and low-resistivity devices are 300 mA/cm² and ~ 4000 mA/cm², respectively. At these current densities, 6×10^6 and 8×10^7 carriers per second, respectively, can be injected into each QD within the luminescent QD layer. Because the single exciton recombination time in a QD is ≤ 10 ns,^{22,23} at these current levels the maximum exciton density per QD is 3% and 40% for the high- and low-resistivity devices, respectively.

Figure 2 shows the EL spectrum of a NiO QD-LED, containing a resistive NiO layer ($\rho_1 = 5$ Ω·cm), at a current density of 200 mA/cm². The 30 nm fwhm QD emission peak centered at $\lambda = 625$ nm dominates the EL spectrum. The broader shoulder centered at $\lambda = 530$ nm is due to a weak Alq₃ emission. The 1 eV band offset (Figure 1a) between the HOMO levels of CdSe QDs and Alq₃ enables hole injection into the Alq₃ film. The inset in Figure 2 shows the evolution of η_{EL} as a function of current density for the same device. The efficiency is calculated as the ratio between the measured photocurrent (measured with a calibrated silicon photodetector) and the total injected current into the device. A maximum η_{EL} of 0.18% and brightness of up to 3000 cd/m² are achieved for most of the high-resistivity devices.

Figure 3 illustrates the negative impact of low-resistance NiO (10^{-2} Ω·cm) on the QD-LED EL spectrum for the second set of devices. In contrast to the device in Figure 2, nearly 50% of the detected EL comes from the Alq₃ layer for current densities lower than 300 mA/cm². This effect is attributed to (i) the imbalance of electron and hole injection at QD sites due to the highly doped NiO thin films, which decreases the exciton density per QD, and (ii) the quenching of the QD layer by the free holes in NiO via energy transfer. Additionally, previous studies on the photoluminescence

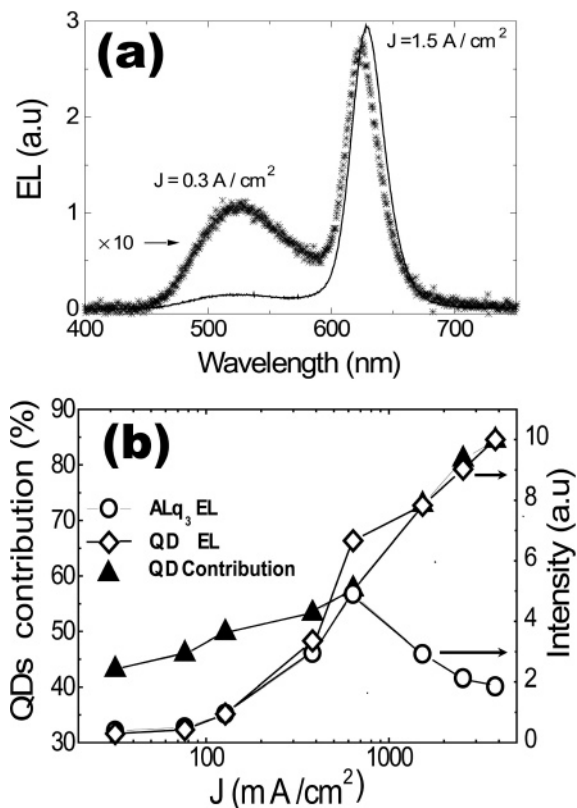


Figure 3. (a) EL spectra of a NiO QD-LED at 300 mA/cm² (stars) and 1500 mA/cm² (solid line) using a film with a resistivity of 10^{-2} Ω·cm. (b) Contribution (solid triangles) of the QD electroluminescence to the EL spectrum versus current density. Integrated areas below the Alq₃ (open circles) and QD (open diamonds) emission peaks, in arbitrary units, as a function of the current density.

intermittency of single CdSe QDs^{24–27} and charging²⁸ of self-assembled CdSe QD films have shown that a charged QD (i.e., a QD with an excess of holes or electrons) is non-emissive because of ultrafast (~ 100 ps) nonradiative Auger^{29–30} processes. Furthermore, the increased hole density shifts the exciton recombination region into the Alq₃ layer, which leads to more emission from the organic layer. At 1.5 A/cm², 85% of the EL originates from the QDs. The increase in the QD spectral contribution with current is due to a 60% decrease in the Alq₃ emission from 600 mA/cm² to 3000 mA/cm² combined with a 50% increase in the QD emission. Figure 3b illustrates the evolution of the integrated areas below the Alq₃ and QD EL peaks, respectively. The solid triangle curve summarizes the evolution of the spectral contribution (in %) of the QDs to the EL spectrum as a function of current density. A 5 nm red shift is noticeable in the EL spectrum at 1.5 A/cm². We speculate that this is due to a Stark effect from high local fields at high current densities.

Finally, as a consequence of quenching and charge imbalance, $\eta_{EL} < 10^{-3}$ % for most of the devices using low-resistivity NiO.

In conclusion, we have fabricated QD-LEDs using p-type NiO films as hole-transporting layers. Careful optimization of the NiO thin film resistivity has enabled us to (i) reduce the quenching of QD luminescence (ii) improve the charge

balance inside the device and (iii) reach QD-LED external quantum efficiencies of 0.18%. The present QD-LEDs are less efficient than the best reported QD-LEDs that utilize TPD hole transport layer. In contrast to earlier studies, however, this work utilizes more stable metal oxide films. Furthermore, we believe that we have not yet reached the limit of device optimization because we speculate that a large fraction of the injected current is shunted through the device due to the roughness of the ITO/NiO sputtered interface. With a smoother ITO/NiO interface, we expect to increase the QD-LED efficiency due to the reduction of shunt currents from direct contacts between ITO/NiO spikes and the Alq₃ layer. Finally, the use of a stable inorganic material as the hole-injection layer enables deposition of QDs by spin-casting or even inkjet-printing out of organic solutions. This is in contrast to solvent-sensitive organic thin films, which require more complicated stamping deposition techniques.³¹ Consequently, the introduction of metal oxides has expanded and simplified the fabrication process of QD-LEDs.

Acknowledgment. This research was funded in part by the NSF-MRSEC program (DMR-0213282), making use of its shared experimental facilities, a PECASE grant (VB), and by the U.S. Army through the Institute for Soldier Nanotechnologies (DAAD-19-02-0002). MGB also acknowledges funding from the David and Lucile Packard Foundation and the Harrison Spectroscopy Laboratory (NSF-CHE-011370).

References

- (1) Colvin, V. L.; Schlamp, M. C.; Alivisatos, A. P. *Nature* **1994**, *370*, 354.
- (2) Tessler, N.; Medvedev, V.; Kazes, M.; Kan, S.; Banin, U. *Science* **2002**, *295*, 1506.
- (3) Coe-Sullivan, S.; Woo, W.-K.; Bawendi, M.; Bulovic, V. *Nature* **2002**, *420*, 800.
- (4) Hikmet, R. A. M.; Talapin, D. V.; Heller, H. J. *Appl. Phys.* **2003**, *93*, 3509.
- (5) (a) Coe-Sullivan, S.; Steckel, J. S.; Woo, W.-K.; Bawendi, M. G.; Bulovic, V. *Adv. Funct. Mater.* **2005**, *15*, 1117–1124. (b) Coe-Sullivan, S.; Woo, W.-K.; Steckel, J.; Bawendi, M. G.; Bulovic, V. *Org. Electron.* **2003**, *4*, 123–130.
- (6) Gosh, A. P.; Gerenser, L. J.; Jarman, C. M.; Formalik, J. E. *Appl. Phys. Lett.* **2005**, *86*, 223503.
- (7) McElvain, J. M.; Antoniadis, H.; Hueschen, M. R.; Miller, J. N.; Roitman, D. M.; Sheats, J. R.; Moon, R. L. *J. Appl. Phys.* **1996**, *80*, 6002.
- (8) Sato, H.; Minami, T.; Takata, S.; Yamada, T. *Thin Solid Films* **1993**, *236*, 1–2.
- (9) Suga, K.; Koshizaki, N.; Yasumoto, K.; Smela, E. *Sens. Actuators, B* **1993**, *14*, 598.
- (10) Lee, W. Y.; Mauri, D.; Hwang, C. *Appl. Phys. Lett.* **1998**, *72*, 1584.
- (11) Liao, C.-H.; Lee, M.-T.; Tsai, C.-H.; Chen, C. H. *Appl. Phys. Lett.* **2005**, *86*, 203507.
- (12) VanSlyke, S. A.; Chen, C. H.; Tang, C. W. *Appl. Phys. Lett.* **1996**, *69*, 2160.
- (13) Aziz, H.; Popovic, Z. D.; Hu, N.-X.; Hor, A.-M.; Xu, G. *Science* **1999**, *283*, 1900.
- (14) Aziz, H.; Popovic, Z. D. *Appl. Phys. Lett.* **2002**, *80*, 2180.
- (15) Drexhage, K. H.; Fleck, M.; Khun, H.; Schaffer, F. P.; Sperling, W. *Ber. Bunsen-Ges. Phys. Chem.* **1966**, *70*, 1179.
- (16) Kuhn, H.; Mobius, D. *Angew. Chem.* **1971**, *10*, 620.
- (17) Chance, R. R.; Prock, A.; Silbey, R. J. *Chem. Phys.* **1974**, *60*, 2744.
- (18) Larkin, I.; Stockma, M. I.; Achermann, M.; Klimov, V. *Phys. Rev. B* **2004**, *69*, 121403(R).
- (19) Morawitz, H. *Phys. Rev.* **1969**, *187*, 1792.
- (20) Burrows, P. E.; Forrest, S. R. *Appl. Phys. Lett.* **1994**, *64*, 2285.
- (21) Burrows, P. E.; Shen, Z.; Bulovic, V.; McCarty, D. M.; Forrest, S. R.; Cronin, J. E.; Thompson, M. E. *J. Appl. Phys.* **1996**, *79*, 7991.
- (22) Brokmann, X.; Coolen, L.; Dahan, M.; Hermier, J. P. *Phys. Rev. Lett.* **2004**, *93*, 107403.
- (23) Kagan, C. R.; Murray, C. B.; Nirmal, M.; Bawendi, M. G. *Phys. Rev. Lett.* **1996**, *76*, 1517.
- (24) Nirmal, M.; Dabbousi, B. O.; Bawendi, M. G.; Macklin, J. J.; Trautman, J. K.; Harris, T. D.; Brus, L. E. *Nature (London)* **1996**, *383*, 802.
- (25) Neuhauser, R. G.; Shimizu, K. T.; Woo, W. K.; Empedocles, S. A.; Bawendi, M. G. *Phys. Rev. Lett.* **2000**, *85*, 3301.
- (26) Tang, J.; Marcus, R. A. *J. Chem. Phys.* **2005**, *123*, 054704.
- (27) Krauss, T. D.; Brus, L. E. *Phys. Rev. Lett.* **1999**, *83*, 4840.
- (28) Woo, W. K.; Shimizu, K. T.; Jarosz, M. V.; Neuhauser, R. G.; Leatherdale, C. A.; Rubner, M. A.; Bawendi, M. G. *Adv. Mater.* **2002**, *14*, 1071.
- (29) Kharchenko, V. A.; Rosen, M. J. *Lumin.* **1996**, *70*, 158.
- (30) Guyot-Sionnest, P.; Wehrenberg, B.; Yu, D. J. *Chem. Phys.* **2005**, *123*, 074709.
- (31) Steckel, J. S.; Snee, P.; Coe-Sullivan, S.; Zimmer, J. P.; Halpert, J. E.; Anikeeva, P.; Kim, L.-A.; Bulovic, V.; Bawendi, M. G. *Angew. Chem., Int. Ed.* **2006**, *45*, 5796.

NL0623208

DOI: 10.1002/anie.200600317

Color-Saturated Green-Emitting QD-LEDs**

Jonathan S. Steckel, Preston Snee, Seth Coe-Sullivan,
John P. Zimmer, Jonathan E. Halpert, Polina Anikeeva,
Lee-Ann Kim, Vladimir Bulovic, and
Moungi G. Bawendi*

Semiconductor nanocrystals (NCs) or quantum dots (QDs) show great promise for use in QD-LED (quantum dot light-emitting device) displays, owing to their unique optical properties and the continual development of new core and core-shell structures to meet specific color needs.^[1–10] This in combination with the recent development of more efficient and saturated QD-LEDs as well as new QD-LED fabrication techniques,^[11,12] suggests that QD-LEDs have the potential to become an alternative flat-panel display technology. The ideal red, green, and blue emission spectrum of an LED for a display application should have a narrow bandwidth and a wavelength such that its color coordinates on the Commission Internationale de l'Eclairage (CIE) chromaticity diagram lie outside the current National Television System Committee (NTSC) standard color triangle (see Figure 2). For a Gaussian emission spectrum with a full width at half maximum (FWHM) of 30 nm and a maximized perceived power, the optimal peak wavelength for display applications is $\lambda = 610$ – 620 nm for red, $\lambda = 525$ – 530 nm for green, and $\lambda = 460$ – 470 nm for blue. For the red pixels, wavelengths longer than $\lambda = 620$ nm become difficult for the human eye to perceive, while those shorter than $\lambda = 610$ nm have coordinates that lie inside the standard NTSC color triangle. Optimization of wavelength for the blue pixels follows the same arguments as for the red pixel, but at the other extreme of the visible spectrum. For green pixels, $\lambda = 525$ – 530 nm provides a color

triangle with the largest area on the CIE chromaticity diagram (and therefore the largest number of colors accessible by a display). Wavelengths longer than $\lambda = 530$ nm make some of the blue/green area of the triangle inaccessible. Wavelengths shorter than $\lambda = 525$ nm compromise the yellow display emissions.

To date, efficient red-emitting QD-LEDs with a peak emission wavelength optimized for display applications have been realized using (CdSe)ZnS core-shell NCs,^[11,13] while blue QD-LEDs with a peak wavelength of emission optimized for display applications have been realized with a (CdS)ZnS core-shell material.^[10] To date, although efficient green-emitting core-shell semiconductor NCs that emit at $\lambda = 525$ nm have been synthesized, they have not been successfully incorporated into a QD-LED suitable for display applications. Previous work using (CdSe)ZnS core-shell NCs gave QD-LEDs that emit at wavelengths no shorter than $\lambda = 540$ – 560 nm.^[13,14] Using (CdSe)ZnS core-shell NCs to achieve $\lambda = 525$ nm emission requires making small CdSe cores (≈ 2.5 nm in diameter).^[15,16] Such small CdSe semiconductor NCs can be difficult to synthesize with narrow size distributions and high quantum efficiencies, and are also more difficult to process and overcoat with a higher-band-gap inorganic semiconductor, which is necessary for incorporation into solid-state structures. A core-shell composite, rather than an organically passivated NC, is desirable in a solid-state QD-LED device owing to the enhanced photoluminescence and electroluminescence (EL) quantum efficiencies of core-shell NCs and their greater tolerance to the processing conditions necessary for device fabrication.^[13,15–20] Larger NCs are also more desirable for use in QD-LEDs because the absorption cross section of NCs scales with size. Larger NCs with larger absorption cross sections lead to an increase in the efficiency of Förster energy transfer from electroluminescing organic molecules to NCs in a working QD-LED, which in turn leads to more efficient devices.

Herein, we report the synthesis of a $\text{Cd}_x\text{Zn}_{1-x}\text{Se}$ alloy core on which we then grew a $\text{Cd}_y\text{Zn}_{1-y}\text{S}$ shell to create a core-shell NC material with the ideal spectral characteristics for green emission in a QD-LED display and with a size large enough for fabricating a working QD-LED. Our $\text{Cd}_x\text{Zn}_{1-x}\text{Se}$ core synthesis was based on work recently published, in which Cd and Se precursors were slowly introduced into a growth solution of ZnSe NCs.^[1,2] A three-step synthetic route was employed to prepare the $(\text{Cd}_x\text{Zn}_{1-x}\text{Se})\text{Cd}_y\text{Zn}_{1-y}\text{S}$ core-shell NCs. In the first step, ZnSe NCs were prepared by rapidly injecting 0.7 mmol of diethylzinc (Strem) and 1 mL of tri-*n*-octylphosphine selenide (TOPSe; 1M) dispersed in 5 mL of tri-*n*-octylphosphine (TOP; 97% Strem) into a round-bottom flask containing 7 grams of degassed hexadecylamine (distilled from 90% Sigma-Aldrich) at 310°C and by then growing the NCs at 270°C for 90 min. The second step consisted of transferring 8 mL of the above ZnSe NC growth solution, at 160°C, into a degassed solution of 16 grams of tri-*n*-octylphosphine oxide (TOPO; distilled from 90% Sigma-Aldrich) and 4 mmol of hexylphosphonic acid (HPA; Alfa Aesar), also at 160°C. A solution of 1.1 mmol of dimethylcadmium (Strem) and 1.2 mL of TOPSe (1M) dispersed in 8 mL of TOP (97% Strem) was then introduced dropwise

[*] Dr. J. S. Steckel,^[‡] Dr. P. Snee,^[‡] Dr. J. P. Zimmer, J. E. Halpert, Prof. M. G. Bawendi
Massachusetts Institute of Technology
Department of Chemistry
Center for Materials Science and Engineering
and The Institute for Soldier Nanotechnologies
77 Massachusetts Avenue, Room 6-221
Cambridge, MA 02139 (USA)
Fax: (+1) 617-253-7030
E-mail: mgb@mit.edu

Dr. S. Coe-Sullivan,^[‡] P. Anikeeva, L.-A. Kim, Prof. V. Bulovic
Massachusetts Institute of Technology
Laboratory of Organic Optics and Electronics
Department of Electrical Engineering and Computer Science
Cambridge, MA 02139 (USA)

[‡] These authors contributed equally to this work.

[**] This work was funded in part by the NSF-MRSEC program (DMR 0213282), by the US Army through the Institute for Soldier Nanotechnologies, under Contract DAAD-19-02-0002 with the US Army Research Office, by the Presidential Early Career Award for Scientists and Engineers (PECASE). QD-LED = quantum dot light-emitting device.

(1 drop/ ≈ 2 s) into the ZnSe NC growth solution/TOPO/HPA mixture at 150°C. The solution was then stirred at 150°C for 46 h. Before overcoating the $\text{Cd}_x\text{Zn}_{1-x}\text{Se}$ cores with $\text{Cd}_y\text{Zn}_{1-y}\text{S}$, the $\text{Cd}_x\text{Zn}_{1-x}\text{Se}$ cores were isolated by precipitation out of solution twice with a miscible non-solvent. In the third step, the $\text{Cd}_y\text{Zn}_{1-y}\text{S}$ shell was grown by introducing dropwise a solution of dimethylcadmium (20% of total required moles of cation; Strem), diethylzinc (Strem), and hexamethyldisilathiane (Fluka) in 8 mL of TOP into a degassed solution of 10 grams of TOPO (distilled from 90% Sigma-Aldrich) and 2.4 mmol of HPA (Alfa Aesar), which contained the core $\text{Cd}_x\text{Zn}_{1-x}\text{Se}$ NCs, at 150°C (the $\text{Cd}_x\text{Zn}_{1-x}\text{Se}$ cores dispersed in hexane were added to the degassed TOPO/HPA solution and the hexane was removed at 70°C under vacuum prior to the addition of the shell precursors).

To fully characterize our $\text{Cd}_x\text{Zn}_{1-x}\text{Se}$ core material, aliquots were sampled from the growth solution at time $t = 7, 60$, and 2760 min (46 h) and analyzed with transmission electron microscopy (TEM), wavelength dispersive spectroscopy (WDS), and absorption and fluorescence spectrophotometry. Figure 1a shows the absorption and emission spectra of these three aliquots as well as the absorption spectrum of the starting ZnSe NCs (2.6 ± 0.5 nm in diameter, as determined by TEM). Over time the absorption and emission spectra shift to the red and the broad trap emission diminishes after 46 h of growth (Figure 1a, spectrum 4), yielding particles approximately 3 nm in diameter. Upon overcoating the cores of $\text{Cd}_x\text{Zn}_{1-x}\text{Se}$ with $\text{Cd}_y\text{Zn}_{1-y}\text{S}$, the trap emission was completely suppressed, yielding an efficient (quantum yields of 50–60%),^[21] saturated (FWHM = 30 nm), green-emitting core-shell material (≈ 4 nm in diameter) suitable for QD-LED display applications (Figure 1b). An alloyed material for the shell was used to minimize lattice mismatch with the $\text{Cd}_x\text{Zn}_{1-x}\text{Se}$ core.

Table 1 shows the growth time ($t = 0, 7, 60$, and 2760 min) of each aliquot, the average outer diameter determined by TEM, the Zn to Cd ratio determined by WDS, the measured first absorption peak, and calculated alloy ($\text{Cd}_x\text{Zn}_{1-x}\text{Se}$) and core-shell ((ZnSe)CdSe core-shell) wavelengths based on the observed Zn to Cd ratios. We see from the raw data that as the reaction proceeds, the first absorption peak shifts to the red, the Zn to Cd ratio decreases, and the diameter of the particles increases. It is important to note that there is a relatively large increase in particle diameter from $t = 7$ to $t = 60$ min of growth, followed by a negligible increase in diameter from $t = 60$ to $t = 2760$ min (46 h). This small change in diameter is accompanied by a relatively large change in the Zn to Cd ratio as well as a relatively large shift of the first absorption peak to the red. This situation suggests that at $t = 7$ min the structure is most likely a (ZnSe)CdSe core-shell structure and that for $t > 7$ min the structure becomes a $\text{Cd}_x\text{Zn}_{1-x}\text{Se}$ alloy, as a result of the migration of cations in the material.^[3] It is of note that a decrease in particle diameter is initially observed following the introduction of neat

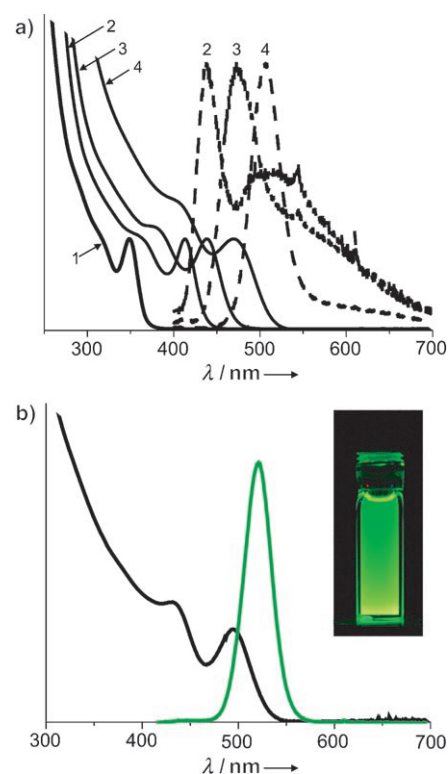


Figure 1. a) Normalized absorption (solid) and emission (dashed) spectra of the core NCs over time: 1) Starting ZnSe NCs (first absorption peak at 350 nm); 2) Aliquot taken out after 7 min of growth (first absorption peak at 413 nm; emission peak at 439 nm); 3) Aliquot taken out after 60 min of growth (438 nm; 475 nm); 4) Aliquot taken out after 46 h of growth (470 nm; 506 nm (FWHM = 34 nm)). b) Absorption (black) and emission (green) spectra of $(\text{Cd}_x\text{Zn}_{1-x}\text{Se})\text{Cd}_y\text{Zn}_{1-y}\text{S}$ core-shell NCs. The emission peaks at 520 nm with a FWHM of 30 nm, and the first absorption feature is at 495 nm. The inset shows the bright, color saturated, green emission from the NCs upon excitation with a UV lamp.

hexadecylamine ZnSe growth solution (2.6 ± 0.5 nm in diameter) into TOPO/phosphonic acid solution at 160°C after about 2/3 of the Cd and Se precursors have been added (7 min aliquot, 1.9 ± 0.3 nm in diameter). This particle etching is plausible based on the large excess of acid present in the solution.

Table 1: Experimental data and the results of effective-mass-approximation calculations of the first transition energy of alloyed $(\text{Cd}_x\text{Zn}_{1-x}\text{Se})$ versus core-shell $(\text{ZnSe})\text{CdSe}$ NCs.

Growth time [min] ^[a]	Outer diameter [nm] ^[b]	Zn/Cd ^[c]	Absorption wavelength [nm] ^[d]	Calculated alloy wavelength [nm]	Calculated core-shell wavelength [nm]	Inner diameter [nm] ^[e]
0	2.6 ± 0.5		350			
7	1.9 ± 0.3	0.33	413	324	416	0.65
60	3.1 ± 0.5	0.18	438	477	509	1.64
2760	3.2 ± 0.5	0.08	470	505	534	1.35

[a] Time from when the Cd and Se precursors were introduced into the flask containing the ZnSe NCs to when the aliquot was removed from the flask (complete addition of the Cd and Se precursors occurred at 9.5 min). [b] Measured from TEM. [c] Measured from WDS. [d] First absorption feature from absorption spectra shown in Figure 1a. [e] Calculated from the Zn/Cd ratio and the known outer NC diameter from TEM measurements. This parameter is relevant only for the core-shell calculations, while the alloy results depend only on the outer diameter.

To help confirm our analysis of the NC morphology ($\text{Cd}_x\text{Zn}_{1-x}\text{Se}$ alloy versus $(\text{ZnSe})\text{CdSe}$ core-shell) we performed calculations whose results are summarized in Table 1. The energies of an electron and hole within an alloyed or a core-shell semiconductor NC were calculated using the effective-mass approximation.^[22,23] These calculations used electron and hole effective masses and band gaps optimized to match reported experimental results for both pure CdSe and ZnSe NCs.^[24–26] We performed two sets of calculations using these optimized parameters to represent an alloyed material or a strict core-shell structure. To model an alloyed NC we adjusted the optimized band gap and electron/hole effective masses by a linear interpolation of the parameters for the pure materials based upon the experimentally determined stoichiometry (i.e., Zn to Cd ratio determined by WDS, shown in Table 1). To model a core-shell structure, we used the measured stoichiometry to determine the core radius and calculated the lowest electron and hole energies of a material with a ZnSe core, CdSe shell, and organic capping layer which has a high band offset (5 eV) for the electron and hole. The lowest transition energy is then determined by adding the electron and hole energies to the optimized band gap^[26] along with the Coulombic binding energy of the electron and hole as determined from perturbation theory.^[27] It can be seen that the calculated first transition energy for a core-shell structure is a good match for the NC material after the initial (7 min aliquot) exposure to the Cd and Se precursors. After prolonged (> 1 h) exposure, the trends in our calculations suggest that an alloyed structure better matches the experimental results, while a core-shell material has a first absorption that is too low in energy. These results suggest that an alloy better represents the electronic structure of our materials.

The $(\text{Cd}_x\text{Zn}_{1-x}\text{Se})\text{Cd}_y\text{Zn}_{1-y}\text{S}$ core-shell NCs were isolated by precipitation out of solution twice with a miscible non-solvent and then filtered through a 0.2 μm syringe filter before use in device fabrication. QD-LED fabrication consisted of first thermally evaporating 4,4'-*N,N'*-dicarbazolyl-biphenyl (CBP) (hole transport layer (HTL)) onto an indium tin oxide (ITO) coated glass substrate at $< 5 \times 10^{-6}$ torr. The QD monolayer, under air-free conditions, was then deposited onto the organic thin film of CBP using micro-contact printing. The substrate was then transported back into the thermal evaporator without exposure to air, where the hole blocking layer (HBL), 3-(4-biphenyl)-4-phenyl-5-*tert*-butylphenyl-1,2,4-triazole (TAZ), and then the electron transporting layer (ETL), tris(8-hydroxyquinoline)aluminum (Alq_3), were deposited. Finally the metal cathode (50 nm thick Mg:Ag, 50:1 by weight, 50 nm Ag cap) was thermally evaporated through a shadow mask to define devices of 1 mm in diameter (see Figure 2a for a diagram of the assembled device structure).

Figure 2a shows the EL spectrum of a typical green-emitting QD-LED. The small peak in the EL spectrum at $\lambda = 380$ nm is CBP emission, which is only 2.6% of the total emission from the device, the rest being QD emission. When the EL spectrum shown in Figure 2a is transformed into its corresponding CIE chromaticity diagram color coordinates ($\text{CIE}_x = 0.21$ and $\text{CIE}_y = 0.70$) we see that it lies far outside of

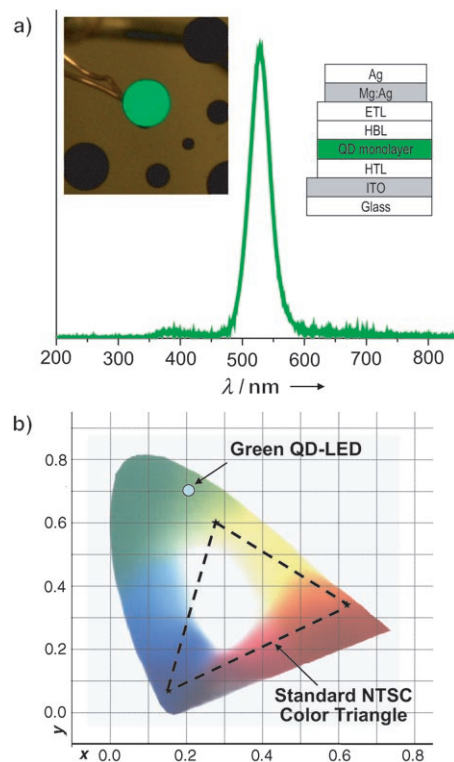


Figure 2. a) The electroluminescence (EL) spectrum for the device: ITO/HTL/($\text{Cd}_x\text{Zn}_{1-x}\text{Se})\text{Cd}_y\text{Zn}_{1-y}\text{S}$ QD monolayer/HBL/ETL/Mg:Ag/Ag (assembled device structure is shown in the inset on the right; see text for details). The emission of the QD-LED peaks at 527 nm with a FWHM of 35 nm. The inset on the left is a photograph of the working green QD-LED. b) The EL spectrum shown in (a), transformed into its CIE chromaticity diagram color coordinates. The standard NTSC color triangle is shown for comparison.

the standard NTSC color triangle (Figure 2b). This shows that using these saturated green-emitting QD-LEDs for a display would provide a significantly larger color triangle on the CIE chromaticity diagram. Figure 3 shows a plot of the external quantum efficiency (EQE) for the device versus current density (J) as well as the current-voltage plot. These devices show low operating voltages (< 10 V) and peak EQEs of 0.5%.

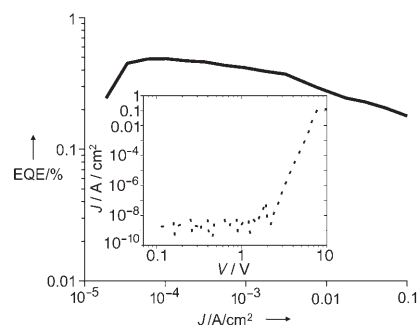


Figure 3. External quantum efficiency (EQE) versus current density (J) for the device (assembled device structure is shown in the inset on the right of Figure 2a). The inset shows the current-voltage curve.

In summary, we have synthesized $\text{Cd}_x\text{Zn}_{1-x}\text{Se}$ alloy core nanocrystals and overcoated these nanocrystals with $\text{Cd}_y\text{Zn}_{1-y}\text{S}$ to create core-shell nanocrystals with the ideal wavelength of emission for QD-LED displays. We have used these $(\text{Cd}_x\text{Zn}_{1-x}\text{Se})\text{Cd}_y\text{Zn}_{1-y}\text{S}$ core-shell nanocrystals to fabricate color-saturated green-emitting QD-LEDs, suitable for display applications.

Received: January 24, 2006

Published online: July 28, 2006

Keywords: light-emitting devices · nanocrystals · quantum dots · semiconductors

- [1] S. A. Ivanov, J. Nanda, A. Piryatinski, M. Achermann, L. P. Balet, I. V. Bezel, P. O. Anikeeva, S. Tretiak, V. I. Klimov, *J. Phys. Chem. B* **2004**, *108*, 10625.
- [2] X. Zhong, R. Xie, Y. Zhang, T. Basche, W. Knoll, *Chem. Mater.* **2005**, *17*, 4038.
- [3] X. Zhong, M. Han, Z. Dong, T. J. White, W. Knoll, *J. Am. Chem. Soc.* **2003**, *125*, 8589.
- [4] R. E. Bailey, S. Nie, *J. Am. Chem. Soc.* **2003**, *125*, 7100.
- [5] X. Zhong, Y. Feng, W. Knoll, M. Han, *J. Am. Chem. Soc.* **2003**, *125*, 13559.
- [6] R. Xie, X. Zhong, T. Basche, *Adv. Mater.* **2005**, *17*, 2741.
- [7] J. J. Li, Y. A. Wang, W. Guo, J. C. Keay, T. D. Mishima, M. B. Johnson, X. Peng, *J. Am. Chem. Soc.* **2003**, *125*, 12567.
- [8] D. V. Talapin, R. Koepppe, S. Gotzinger, A. Kornowski, J. M. Lupton, A. L. Rogach, O. Benson, J. Feldmann, H. Weller, *Nano Lett.* **2003**, *3*, 1677.
- [9] P. Reiss, J. Bleuse, A. Pron, *Nano Lett.* **2002**, *2*, 781.
- [10] J. S. Steckel, J. P. Zimmer, S. Coe-Sullivan, N. E. Stott, V. Bulovic, M. G. Bawendi, *Angew. Chem.* **2004**, *116*, 2206; *Angew. Chem. Int. Ed.* **2004**, *43*, 2154.
- [11] S. Coe-Sullivan, J. S. Steckel, W.-K. Woo, M. G. Bawendi, V. Bulovic, *Adv. Funct. Mater.* **2005**, *15*, 1117.
- [12] S. Coe-Sullivan, J. S. Steckel, L. A. Kim, M. G. Bawendi, V. Bulovic, *Proc. SPIE-Int. Soc. Opt. Eng.* **2005**, 5739, 108.
- [13] S. Coe-Sullivan, W.-K. Woo, J. S. Steckel, M. G. Bawendi, V. Bulović, *Org. Electron.* **2003**, *4*, 123.
- [14] S. Coe, W.-K. Woo, M. Bawendi, V. Bulović, *Nature* **2002**, *420*, 800.
- [15] M. A. Hines, P. Guyot-Sionnest, *J. Phys. Chem.* **1996**, *100*, 468.
- [16] B. O. Dabbousi, J. Rodriguez-Viejo, F. V. Mikulec, J. R. Heine, H. Mattoussi, R. Ober, K. Jensen, M. G. Bawendi, *J. Phys. Chem. B* **1997**, *101*, 9463.
- [17] B. O. Dabbousi, O. Onitsuka, M. G. Bawendi, M. F. Rubner, *Appl. Phys. Lett.* **1995**, *66*, 1316.
- [18] V. L. Colvin, M. C. Schlamp, A. P. Alivisatos, *Nature* **1994**, *370*, 354.
- [19] M. C. Schlamp, X. Peng, A. P. Alivisatos, *J. Appl. Phys.* **1997**, *82*, 5837.
- [20] H. Mattoussi, L. H. Radzilowski, B. O. Dabbousi, E. L. Thomas, M. G. Bawendi, M. F. Rubner, *J. Appl. Phys.* **1998**, *83*, 7965.
- [21] The $(\text{Cd}_x\text{Zn}_{1-x}\text{Se})\text{Cd}_y\text{Zn}_{1-y}\text{S}$ core-shell NC photoluminescence quantum efficiencies were determined by comparing the integrated emission of a given NC sample in dilute hexane solution with an optical density of 0.1 with that of the appropriate laser dye.
- [22] A. R. Kortan, R. Hull, R. L. Opila, M. G. Bawendi, M. L. Steigerwald, P. J. Carroll, L. E. Brus, *J. Am. Chem. Soc.* **1990**, *112*, 1327.
- [23] W. R. Frensley, H. Kroemer, *Phys. Rev. B* **1977**, *16*, 2642.
- [24] C. B. Murray, D. J. Norris, M. G. Bawendi, *J. Am. Chem. Soc.* **1993**, *115*, 8706.
- [25] M. A. Hines, P. Guyot-Sionnest, *J. Phys. Chem. B* **1998**, *102*, 3655.
- [26] The optimized electron effective masses used were 0.3727 for CdSe and 0.345 for ZnSe. The optimized band gaps were 1.9433 for CdSe and 2.9437 for ZnSe. The deviation between the calculated first transition energies versus experiment was on the order of ± 2 nm using these parameters. Band offsets for CdSe relative to ZnSe (-1.20 eV for the electron and 0.22 eV for the hole) were obtained from "Subvolume b, Physics of II-VI and I-VII Compounds, Semimagnetic Semiconductors": *Landolt-Börnstein, New Series, Group III: Crystal and Solid State Physics, Vol. 17* (Ed.: K.-H. Hellwege, O. Madelung, M. Schule, H. Weiss), Springer, Berlin, **1982**.
- [27] L. E. Brus, *J. Chem. Phys.* **1984**, *80*, 4403.

Electroluminescence from a Mixed Red–Green–Blue Colloidal Quantum Dot Monolayer

Polina O. Anikeeva,^{†,‡} Jonathan E. Halpert,^{†,§} Mounji G. Bawendi,^{*,§} and Vladimir Bulović[‡]

Laboratory of Organic Optics and Electronics, Department of Electrical Engineering and Computer Science, Massachusetts Institute of Technology, Cambridge, Massachusetts 02139, and Department of Chemistry, Massachusetts Institute of Technology, Cambridge, Massachusetts 02139

Received February 12, 2007; Revised Manuscript Received April 30, 2007

ABSTRACT

We demonstrate light emitting devices (LEDs) with a broad spectral emission generated by electroluminescence from a mixed-monolayer of red, green, and blue emitting colloidal quantum dots (QDs) in a hybrid organic/inorganic structure. The colloidal QDs are reproducibly synthesized and yield high luminescence efficiency materials suitable for LED applications. Independent processing of the organic charge transport layers and the QD luminescent layer allows for precise tuning of the emission spectrum without changing the device structure, simply by changing the ratio of different color QDs in the active layer. Spectral tuning is demonstrated through fabrication of white QD-LEDs that exhibit external quantum efficiencies of 0.36% (Commission Internationale de l'Eclairage) coordinates of (0.35, 0.41) at video brightness, and color rendering index of 86 as compared to a 5500 K blackbody reference.

The high luminescence efficiency and the narrow spectral emission of colloiddally synthesized quantum dots (QDs)¹ enabled their use in light emitting devices (LEDs)^{2,3} to fabricate planar light sources of high color saturation. In this report we demonstrate that by combining multiple QD lumophores in a diode junction device, an arbitrarily broad electroluminescence spectrum can also be generated, with precisely controlled relative intensities of the constituent spectral components.

Previous reports on efficient monochrome QD-LEDs utilized QD lumophores embedded in organic semiconductor charge transport layers to generate saturated color red, green, and blue (RGB) QD-LEDs with peak efficiencies of 2.0%, 0.5%, and 0.2%, respectively.^{2–6} Monochrome QD-LEDs with lower efficiencies have also been fabricated using inorganic transport layers, which replaced some of the environmentally sensitive organic films.^{7,8} For white color generation, QD lumophores were utilized as a replacement for red^{9,10} or green¹¹ color components in white-light LEDs employing organic emitters. A broad spectral emission using a mixture of QDs has also been demonstrated using red, green, and blue emitting dots embedded in poly(lauryl methacrylate)¹² with a blue GaN or Hg vapor lamp for

excitation. White light photoluminescence from QDs was also obtained by Bowers et al.¹³ and Chen et al.¹⁴ in devices in which deep trap QD luminescence was photoexcited by an external ultraviolet LED. However, deep trap emitters, generally defective CdS or ZnSe QDs, are only weakly luminescent, and the defect trap states on QD lumophores are poorly characterized and not easily reproducible from one synthesis to the next. Using three types of QDs as emitters in an electrically driven structure has been previously reported as preliminary work in our group,¹⁵ and as a parallel effort by Li et al.¹⁶ but with efficiencies of more than a factor of 4 lower.

The goal of the present work is to demonstrate reproducible and efficient spectrally broad electroluminescent QD-LEDs with spectral emission tunable across the CIE (Commission Internationale de l'Eclairage) color space. We demonstrate that the electroluminescence spectrum can be precisely tuned in diode junction devices in which the mixed color electroluminescence is derived from a single QD monolayer containing QDs of multiple colors. To demonstrate spectral tunability, we adjust the relative concentrations of QD components in the QD monolayer to obtain white light emitting QD-LEDs with a high color rendering index.

Our devices consist of an indium tin oxide (ITO) anode on top of a glass substrate with a layer of conducting polymer poly(3,4-ethylenedioxythiophene):poly(styrenesulfonate) PE-DOT:PSS as the hole injection layer, a 40 nm thick hole

[†] These authors contributed equally to this work.

[‡] Laboratory of Organic Optics and Electronics, Department of Electrical Engineering and Computer Science.

[§] Department of Chemistry.

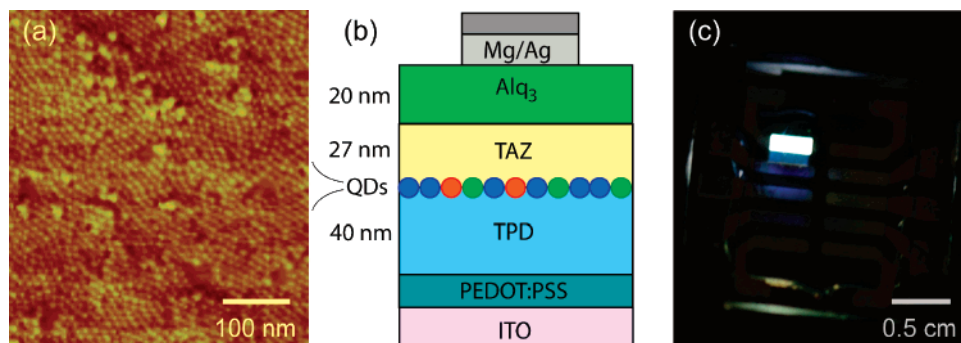


Figure 1. (a) Atomic force microscope phase image of blue QDs forming approximately 1.1 monolayers on top of a 40 nm thick TPD film. (b) Device cross section of a white QD-LED. (c) Photograph of a white QD-LED in operation with 10 V of applied forward bias.

transporting layer of *N,N'*-bis(3-methylphenyl)-*N,N'*-bis(phenyl)benzidine (TPD), an emissive monolayer of colloidal QDs, a 27 nm thick hole blocking layer of 3,4,5-triphenyl-1,2,4-triazole (TAZ) (that limits exciton formation to near/at QD sites), a 20 nm thick electron transporting layer of tris(8-hydroxyquinoline) aluminum (Alq₃), and a 100 nm thick cathode of magnesium silver alloy, coated with a 20 nm thick silver protective layer (see Figure 1). We use three types of colloidal synthesized QDs (see Supporting Information) to generate the red, green, and blue spectral components of the white LED. The red QD solution consisted of CdSe/ZnS core-shell QDs with a photoluminescence (PL) peak at wavelength $\lambda = 620$ nm. The green QD solution consisted of ZnSe/CdSe alloyed cores overcoated with a shell of ZnS with a PL peak at $\lambda = 540$ nm. Finally, the blue QD solution consisted of ZnCdS alloyed QDs with a PL peak at $\lambda = 440$ nm.

QD solutions for the white QD-LEDs were prepared by mixing red, green, and blue QD solutions so that the R:G:B QD ratio in the film is 1:2:10. The R:G:B QD ratio was chosen in part to compensate for the differences in PL efficiency of different QD samples. Additionally, QD-to-QD proximity in the electroluminescent QD monolayer enables exciton energy transfer from higher energy to lower energy QDs,^{17,18} red shifting the overall emission, and necessitating a higher concentration of blue QDs in the QD monolayer. Consequently, blue QDs of high luminescence efficiency are needed for efficient QD-LED operation.

We found that CdSe/ZnS QDs emitting between 550 nm and 650 nm with a quantum yield (QY) of almost 90%¹⁹ produced electroluminescence (EL) devices with external quantum efficiency (EQE) of $\sim 2\%$ in the orange and red.⁵ These QDs readily accept excitons transferred from the blue- and green-emitting transport materials allowing the production of bright and efficient QD-LEDs. Core/shell/shell QDs made from ZnSe/CdSe/ZnS were produced with emission from 510 to 560 nm with a QY of $\sim 70\%$,²⁰ enabling devices with EQE of 0.5%.⁴ The lower EQE of these green devices is likely due to the greater difficulty of transferring excitons from the blue and green emitting transport materials to the QD monolayer, which does not absorb as strongly at those wavelengths as do redder QDs. Blue devices were initially constructed using CdS/ZnS particles, as in previously published devices;⁶ however the QY of the QDs after

processing (15%) was not high enough to allow for efficient blue emission in the film. High QY ZnCdS alloyed QDs were then synthesized instead and found to emit between 400 and 500 nm with a QY of 40% after processing.²¹ These materials were able to produce devices with greater EQE (0.35%) than previous devices and thus enabled the production of mixed films with an adequate blue QY to create reasonably efficient white EL devices. The EQE for the blue devices was still lower than for the green and red devices, mainly because resonant energy transfer of excitons from the organic transport materials is either less efficient, as in the case of TPD, or impossible, as in the case of Alq₃. In this case the device function is more dependent than the green or red devices on the ability of the transport materials to directly inject charge into the band structure of the QDs. Since it is more difficult to inject holes into the valence band of bluer QDs, these QDs tend to emit at higher voltages and as a result the white device CIE shifted to the blue with increased voltage.

EL spectra for the red, green, blue, and mixed-monolayer QD-LEDs are measured at near video brightness (Figure 2). The EL spectra of red and green QD-LEDs correspond to the color-saturated PL spectra characteristic of colloidal QDs, with CIE coordinates of (0.65, 0.34) and (0.31, 0.65), respectively. The blue QD-LED spectrum has a dominant QD component and weaker Alq₃ and TPD emission, consistent with energy transfer^{22,23} and downconversion of the deep blue QD luminescence by Alq₃ (expected from the spectral overlap of Alq₃ absorption and blue QD PL). In contrast, spectral overlap of TPD PL and blue QD absorption is insufficient to provide complete quenching of TPD EL via energy transfer from TPD to blue QDs. CIE coordinates of the blue QD-LEDs are (0.19, 0.11). We note that the hole blocking TAZ layer should physically separate the blue QD monolayer Alq₃ film inhibiting QD-to-Alq₃ energy transfer and Alq₃ luminescence. However, the TAZ film is not planar when grown on the QD monolayer,^{5,24} allowing pinholes to form in which some QDs come into contact with the Alq₃ film. This contributes to Alq₃ EL in blue QD-LEDs.

The emission spectrum of the mixed-monolayer QD-LED (Figure 2) shows a pronounced contribution of red, green, and blue QD EL components. The TPD EL signal is largely quenched due to efficient energy transfer to the red and green QDs. Alq₃ still appears to exhibit a weak spectral feature in

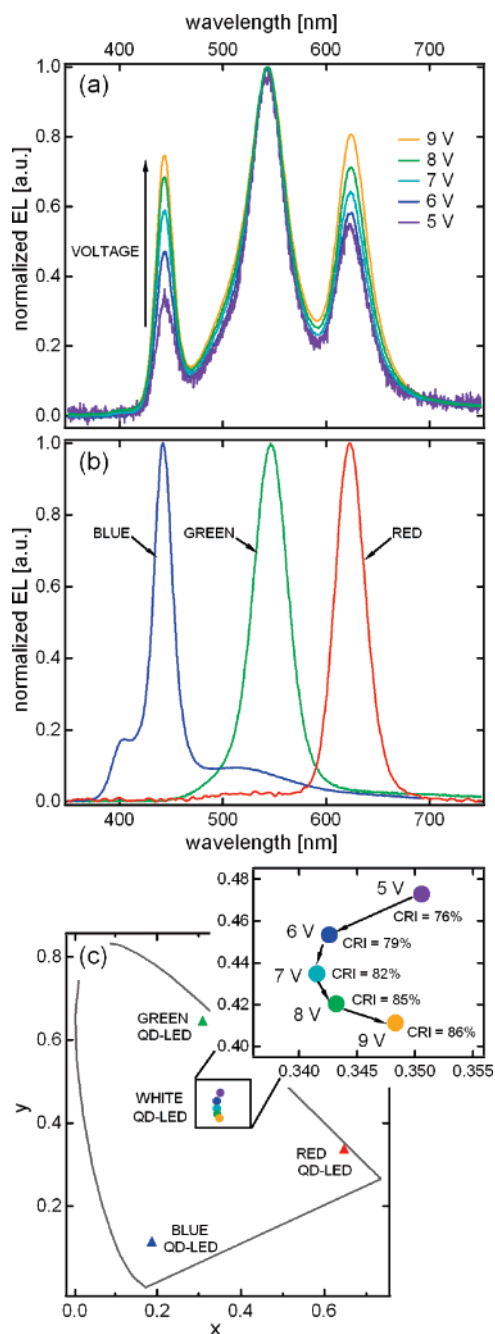


Figure 2. (a) Normalized EL spectra of a white QD-LED for a set of increasing applied voltages. The relative intensities of red and blue QD spectral components increase in comparison to the green QD component at higher biases. (b) Normalized EL spectra of red, green, and blue monochrome QD-LEDs (red, green, and blue lines, respectively). (c) CIE coordinates of the red, green, blue QD-LEDs (triangles). Circle symbols show the evolution of CIE coordinates and CRI of the white QD-LEDs upon increasing applied bias.

the white QD-LED spectrum analogous to the blue QD-LEDs. The mixed-monolayer QD-LED pixels appear uniformly luminescent, look “white” to the eye (Figure 1), with CIE coordinates (0.35, 0.41) at 9 V applied bias and color rendering index (CRI) of 86, when compared to 5500 K black body reference. Such high CRI compares favorably to conventional white light sources such as “cool white”

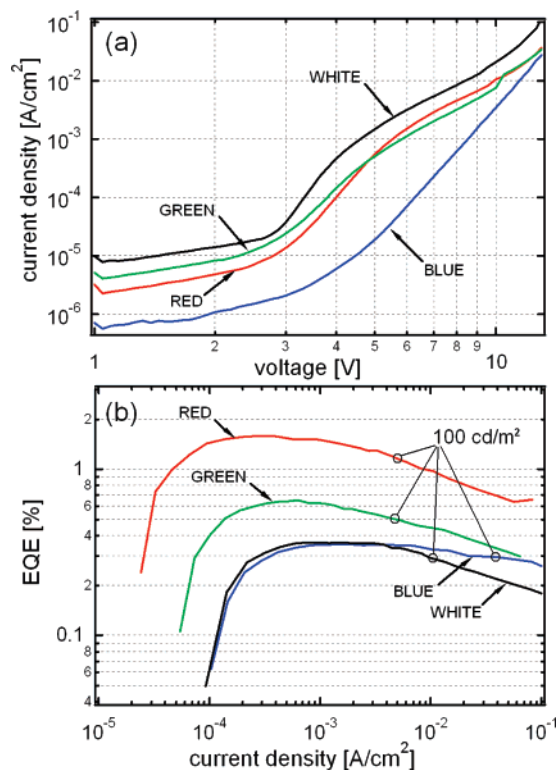


Figure 3. Current–voltage characteristics (a) and external electroluminescence quantum efficiency (b) measured for red, green, blue, and white QD-LEDs labeled with red, green, blue and black lines, respectively. The circled data points indicate device brightness of 100 cd/m².

fluorescent (CRI = 62), incandescent (CRI = 100), and dye-enhanced InGaN/GaN solid-state LEDs (CRI > 80).²⁵

The peak EQE of our monochrome QD-LEDs are measured to be 1.6% at 4.6 V (0.29 mA/cm²) for red devices, 0.65% at 5.2 V (0.63 mA/cm²) for green, and 0.35% at 9.1 V for blue (1.73 mA/cm²) (Figure 3). These values are consistent with previously reported QD-LEDs,^{2–6} with our green and blue QD-LEDs more efficient than those in previous reports.^{4,6} The peak EQE of white QD-LEDs is 0.36% at 5.0 V (1.51 mA/cm²) (Figure 3), which corresponds to 0.9 cd/A and 0.57 lm/W, at a brightness of 13.5 cd/m². At 9 V applied bias, and optimal CIE position, the brightness was 92 cd/m², with efficiencies of 0.28% EQE, 0.7 cd/A, and 0.24 lm/W at 13 mA/cm² current. Maximum brightness topped 830 cd/m² at 14 V and 230 mA/cm².

The significant difference between EQEs of the red, green, and blue QD-LEDs originates from the difference in the QD band structures, which affect the two dominant QD excitation mechanisms in QD-LEDs:

(1) The QD energy band structure alignment with respect to the electron energy levels of neighboring TPD and TAZ layers determines the efficacy of electron and hole injection into the QD layer. From the bulk band structure and electron/hole masses of the QD materials, we expect that the energy barrier to hole injection increases for wider band gap QDs while an electron barrier is nonexistent in all of the structures (see the QD-LED energy band diagram in inset to Figure 4).

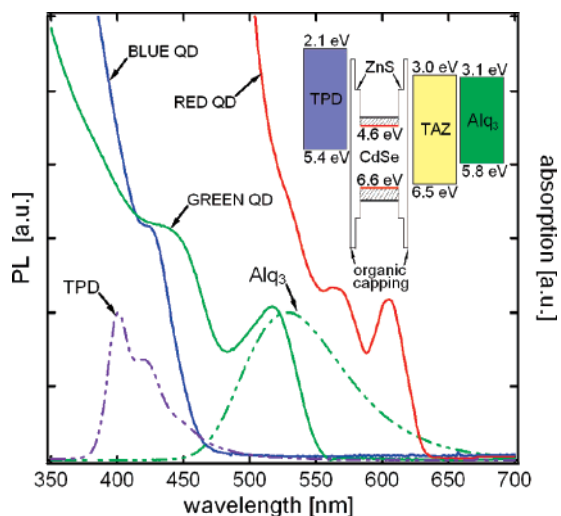


Figure 4. Red, green, and blue QD absorption spectra labeled with red, green, and blue solid lines, respectively, are shown together with TPD and Alq₃ PL spectra labeled with purple and green dashed lines to demonstrate spectral overlaps. (inset) Suggested band diagram for the QD-LEDs of this study. Conduction and valence band position for the red QDs are labeled with red energy levels; the shaded area shows the range of likely energy level positions for the conduction and valence bands of the green and blue QDs.

(2) Resonant exciton energy transfer directs the excitons to the lowest available energy levels, favoring formation of the red excitons over the blue ones. For example, excitons formed on TPD in the vicinity of the QD layer resonantly transfer their energy to the QDs,²³ favoring energy transfer to red and green QDs over blue QDs due to the enhanced spectral overlap between TPD PL and QD absorption (see Figure 4). Also, with imperfections in the TAZ hole blocking layer, the Alq₃ film is in partial contact with the QDs and can either take energy from the more energetic blue QDs or transfer it back to red QDs.

In the red QD-LEDs, both direct charge injection and energy transfer from TPD and Alq₃ can contribute to the high EQEs of these devices. In the green QD-LEDs direct charge injection could be similar as for red QD-LEDs and energy transfer from the TPD to green QDs should be efficient due to the significant overlap of TPD emission and green QD absorption spectra and less efficient from Alq₃ to green QDs (Figure 4). The lower photoluminescence efficiency of the green QD solutions used in these experiments (~70%) as compared to the red QD solutions (90%) may also contribute to the lower EQE of green QD-LEDs (Figure 3).

The lower EQEs of the blue QD-LEDs (Figure 3) could be attributed to the low efficacy of hole injection from TPD into the blue QDs due to the increased potential barrier at this junction (see band lineup in inset to Figure 4) or to the reduced tunneling rate through the organic groups capping the blue QDs. The reduced hole injection is manifested as an increase in the turn-on voltage of blue QD-LEDs (Figure 3), leading to an excess electron charging of the QDs, which reduces the QD PL efficiency.²⁶ Additionally, energy transfer from the TPD film to blue QDs is not as efficient as that for red or green QDs (Figure 4), while at the same time blue

QDs can efficiently transfer their excitons to any Alq₃ molecules located within the Förster radius. The imperfections in the QD monolayer and TAZ film lead to charge transport directly through the organic layers and exciton formation within TPD and Alq₃ layers. In the case of green and red QDs, excitons formed in the organic layer can be resonantly transferred to QDs, but in the case of blue QDs these excitons radiatively recombine in the organic layer contributing to TPD and Alq₃ spectral features in the QD-LED EL spectra.

The mixed-monolayer QD-LEDs contain three types of QDs with different responses to charge injection, leading to a change in the EL spectrum at different driving conditions. Figure 2a shows the EL spectrum color shift in a mixed-monolayer QD-LED as the applied bias increases from 5 to 9 V, resulting in a small change of the CIE coordinates and CRI (see Figure 2c). With increasing voltage we observe an increase of the red and blue QD spectral components in the EL spectrum relative to the initially dominant green QD spectral component. This evolution of spectral features with increasing bias is consistent with the reduced efficacy of hole injection into blue QDs. At low applied bias (5 V) charge injection into the mixed QD film of the mixed-monolayer QD-LED is dominated by injection into the green and red QDs. Resonant energy transfer from green QDs to red QDs is inhibited by the relatively small number of both red and green QDs as compared to blue QDs in the mixed QD monolayer, so that the probability of locating a green QD next to a red QD is small. At higher applied biases charge injection into blue QDs becomes more efficient, and the EL component of the blue QDs becomes more significant. Increased exciton formation on blue QDs also benefits red and green QD luminescence due to exciton energy transfer from blue QDs to red and green QDs. Note that the energy transfer to red QDs is more efficient than that to green QDs due to an increased spectral overlap, with the consequence that with an increase of blue QD luminescence (at higher operating voltages), red QD luminescence rises more than the green QD luminescence. Exciton formation on the more numerous blue QDs governs the overall efficiency of white QD-LEDs which closely tracks the efficiency of the monochrome blue QD-LEDs (Figure 3).

The operation of the mixed-monolayer QD-LED is enabled by the use of identical electron transporting, hole blocking, and hole transporting layers in all of our monochrome QD-LEDs, which also imparts simplicity to color tuning the mixed-monolayer QD-LED sources. Colloidal QDs demonstrate exceptional PL stability exceeding 10⁹ turnovers in the most stable QD structures;²⁷ consequently concern over differential aging of different-color QD samples is minimal, assuring stability of spectral emission, as long as the remaining films that comprise the QD-LED stay unchanged.

Akin to mixing colors in a paint shop, the present work demonstrates that QD solutions can be precisely mixed to achieve a desired QD-LED spectrum at a desired driving condition.

Acknowledgment. This work was supported in part by the NSF-MRSEC Program (DMR-0213282), making use of

its Shared Experimental Facilities, and the U.S. Army through the Institute for Soldier Nanotechnologies (DAAD-19-02-0002) and NIRT (subcontract GLV13-01).

Note Added after ASAP Publication. An incorrect version of Figure 3 appeared in the version published ASAP July 7, 2007; a corrected version was published ASAP July 19, 2007; affiliation line corrections were made in the version posted ASAP July 25, 2007.

Supporting Information Available: Experimental details including synthesis and device fabrication. This material is available free of charge via the Internet at <http://pubs.acs.org>.

References

- (1) Murray, C. B.; Norris, D. J.; Bawendi, M. G. *J. Am. Chem. Soc.* **1993**, *115*, 8706–8715.
- (2) Dabbousi, B. O.; Bawendi, M. G.; Onitsuka, O.; Rubner, M. F. *Appl. Phys. Lett.* **1995**, *66* (11), 1316–1318.
- (3) Coe, S.; Woo, W.-K.; Bawendi, M. G.; Bulović, V. *Nature* **2002**, *420*, 800–803.
- (4) Steckel, J. S.; Snee, P.; Coe-Sullivan, S.; Zimmer, J. P.; Halpert, J. E.; Anikeeva, P.; Kim, L.; Bulovic, V.; Bawendi, M. G. *Angew. Chem., Int. Ed.* **2006**, *45* (35), 5796–5799.
- (5) Coe-Sullivan, S.; Steckel, J. S.; Woo, W.-K.; Bawendi, M. G.; Bulovic, V. *Adv. Funct. Mater.* **2005**, *15*, 1117–1124.
- (6) Steckel, J. S.; Zimmer, J. P.; Coe-Sullivan, S.; Stott, N. E.; Bulović, V.; Bawendi, M. G. *Angew. Chem., Int. Ed.* **2004**, *43*, 2154–2158.
- (7) Mueller, A. H.; Petruska, M. A.; Achermann, M.; Werder, D. J.; Akhaddov, E. A.; Koleske, D. D.; Hoffbauer, M. A.; Klimov, V. I. *Nano Lett.* **2005**, *5*, 1039–1044.
- (8) Caruge, J.-M.; Halpert, J. E.; Bulovic, V.; Bawendi, M. G. *Nano Lett.* **2006**, *6*, 2991–2994.
- (9) Gao, M.; Richter, B.; Kirstein, S. *Adv. Mater.* **1997**, *9*, 802–805.
- (10) Li, Y.; Rizzo, A.; Mazzeo, M.; Carbone, L.; Manna, L.; Cingolani, R.; Gigli, G. *J. Appl. Phys.* **2005**, *97*, 113501 1–4.
- (11) Park, J. H.; Kim, J. Y.; Chin, B. D.; Kim, Y. C.; Kim, J. K.; Park O. *Nanotechnology* **2004**, *15*, 1217–1220.
- (12) Lee, J.; Sundar, V. C.; Heine, J. R.; Bawendi, M. G.; Jensen, K. F. *Adv. Mater.* **2000**, *12*, 1102–1105.
- (13) Bowers, M. J., II; McBride, J. R.; Rosenthal, S. J. *J. Am. Chem. Soc.* **2005**, *127*, 15378–15379.
- (14) Chen, H. S.; Wang, S. J. J.; Lo, C. J.; Chi, J. Y. *Appl. Phys. Lett.* **2005**, *86*, 131905 1–3.
- (15) Anikeeva, P. O.; Halpert, J. E.; Bawendi, M. G.; Bulović, V. Basic Research Needs for Solid-State Lighting, May 22–24, 2006.
- (16) Li, Y.; Rizzo, A.; Cingolani, R.; Gigli, G. *Adv. Mater.* **2006**, *18*, 2545–2548.
- (17) Kagan, C. R.; Murray, C. B.; Nirmal, M.; Bawendi, M. G. *Phys. Rev. Lett.* **1996**, *76*, 1517–1520.
- (18) Crooker, S. A.; Hollingsworth, J. A.; Tretiak, S.; Klimov, V. I. *Phys. Rev. Lett.* **2002**, *89*, 186802 1–4.
- (19) Hines, M. A.; Guyot-Sionnest, P. *J. Phys. Chem.* **1996**, *100*, 468–471.
- (20) Ivanov, S. A.; Nanda, J.; Piryatinski, A.; Achermann, M.; Balet, L. P.; Bezel, I. V.; Anikeeva, P. O.; Tretiak, S.; Klimov, V. I. *J. Phys. Chem. B* **2004**, *108*, 10625–10630.
- (21) Zhong, X.; Feng, Y.; Knoll, W.; Han, M. *J. Am. Chem. Soc.* **2003**, *125*, 13559–13563.
- (22) Förster, Th. *Ann. Phys.* **1948**, *6*, 55–75.
- (23) Kuhn, H. *J. Chem. Phys.* **1970**, *53*, 101–108.
- (24) Huang, H.; Dorn, A.; Bulović, V.; Bawendi, M. G. *Appl. Phys. Lett.* **2007**, *90*, 023110 1–3.
- (25) Krames, M. R.; Bhat, J.; Collins, D.; Gardner, N. F.; Gotz, W.; Lowery, C. H.; Ludowise, M.; Martin, P. S.; Mueller, G.; Mueller-Mach, R.; Rudaz, S.; Steigerwald, D. A.; Stockman, S. A.; Wierer J. *J. Phys. Status Solidi A* **2002**, *192*, 237–245.
- (26) Neuhauser, R. G.; Shimizu, K. T.; Woo, W. K.; Empedocles, S. A.; Bawendi, M. G. *Phys. Rev. Lett.* **2000**, *85*, 3301–3304.
- (27) Nirmal, M.; Dabousi, B. O.; Bawendi, M. G.; Macklin, J. J.; Trautman, J. K.; Harris, T. D.; Brus, L. E. *Nature* **1996**, *383*, 802–804.

NL0703424

Electrically driven light emission from single colloidal quantum dots at room temperature

Hao Huang and August Dorn

Department of Chemistry, Massachusetts Institute of Technology, Cambridge, Massachusetts 02139

Vladimir Bulovic^{a),b)}

Department of Electrical Engineering and Computer Science, Massachusetts Institute of Technology, Cambridge, Massachusetts 02139

Moungi G. Bawendi^{a),c)}

Department of Chemistry, Massachusetts Institute of Technology, Cambridge, Massachusetts 02139

(Received 13 October 2006; accepted 26 November 2006; published online 10 January 2007)

Light emission from single colloidal CdSe/ZnS (core/shell) nanocrystals embedded in electrically driven organic light emitting devices is demonstrated at room temperature. Spectral diffusion and blinking from individual quantum dots were observed both in electro- and photoluminescence. The authors propose a model in which the nanocrystals act as seeds for the formation of current channels that lead to enhanced exciton recombination in the vicinity of the quantum dots. This work demonstrates that individual semiconductor nanocrystals can serve as emissive probes in organic light emitting devices and that they can be used to manipulate device structure and properties at the nanometer scale. © 2007 American Institute of Physics. [DOI: 10.1063/1.2425043]

Colloidal semiconductor nanocrystal quantum dots (QDs), also called “artificial atoms,”¹ have found their way into many potential applications due to their narrow emission spectrum and strong optical absorption, including biological labeling,² quantum dot light emitting devices (LEDs),³ solar cells,⁴ and lasers.^{5–7} Photoluminescence (PL) studies at low laser excitation power have shown that QDs are also potential candidates for nonclassical light sources.^{8–10} Electroluminescence (EL) from single QDs, which is more appealing for practical applications, has only been demonstrated recently at low temperature^{11–13} using self-assembled QDs grown by molecular beam epitaxy (MBE). To date, however, there are no reports of EL from single colloidal quantum dots, which can be synthesized by wet chemical methods enabling processing and integration versatility. In contrast to molecular-beam-epitaxy grown QDs, the size and concentration of colloidal QDs in a device can be controlled independently over a wide range, and mixtures of QDs with different emission wavelengths can be incorporated into a single layer. Furthermore, the organic ligands surrounding colloidal nanocrystals facilitate QD integration into organic LED structures. In previous attempts with layered organic LEDs, EL from single QDs was masked by exciplex emission from the organic films.¹⁴ In the present study, we report spectrally resolved EL emission from single colloidal QDs embedded in layered organic LED structures at room temperature.

Our devices are conceptually similar to the ones reported by Coe *et al.*³ The device substrates were prepared by rf sputtering 80 nm thick indium tin oxide (ITO) strips onto ~0.13 mm cover glasses through a shadow mask. Then a polyethylenedioxythiophene (PEDOT) solution (Baytron CH8000) was spun onto the glass/ITO substrates at 3000 rpm and baked for 30 min. The CdSe/ZnS (core/shell) nanocrystals used in the devices were obtained from Quan-

tum Dot Corporation (QDC, Catalog No. 1002-1), with a PL emission wavelength centered around 655 nm and a quantum yield of 75%.¹⁰ The QDs were precipitated three times with butanol and methanol, and then redispersed in anhydrous chloroform, to which *N,N'*-diphenyl-*N,N'*-bis(3-methylphenyl)-(1,1'-biphenyl)-4,4'-diamine (TPD) was added at a concentration of 10 mg/ml. The resulting TPD-QD solution was spun onto the device substrates at 3000 rpm in a nitrogen glove box forming an ~50 nm thick film. The devices were then transferred into an evaporator, where an ~20 nm thick 3-(4-biphenyl)-4-phenyl-5-tert-butylphenyl-1,2,4-triazole (TAZ) layer, an ~20 nm thick aluminum tris (8-hydroxyquinoline) (Alq₃) layer, and an ~100 nm thick Ag-Mg and an ~20 nm thick Ag layer were evaporated in sequence at a background pressure of 6×10^{-7} Torr. In the device, TPD acts as a hole conducting layer, TAZ as a hole blocking layer, and Alq₃ as an electron conducting layer with Ag-Mg/Ag as the top electrode and ITO as the transparent bottom electrode. A schematic of a cross section of the device (not to scale), is shown in Fig. 1(a). The substrates were then packaged in a nitrogen glove box with glass coverslips and UV curable epoxy to minimize device exposure to oxygen and humidity, and mounted onto an xyz piezostage. The 514 nm line of an Ar-ion laser with an intensity of ~10 W/cm² was used as an excitation source.

Images were taken through the transparent ITO electrode using a 100× oil immersion objective (Nikon) and an intensified charge-coupled device camera (Pentamax, Princeton Instruments). First the objective was focused on the fluorescence signal of the QDs under laser excitation to obtain PL images. The laser was then switched off, and a positive voltage was applied to the ITO bottom electrode while the Ag-Mg/Ag top electrode was grounded. For voltages above 3 V, we observed EL from the organic films, with EL signals from single QDs becoming most pronounced above 8 V. Typical PL and EL images of the same area are shown in Figs. 1(b) and 1(c). Many of the bright spots blinked and appeared both in PL and EL, suggesting that many of them

^{a)}Authors to whom correspondence should be addressed.

^{b)}Electronic mail: bulovic@mit.edu

^{c)}Electronic mail: mgb@mit.edu

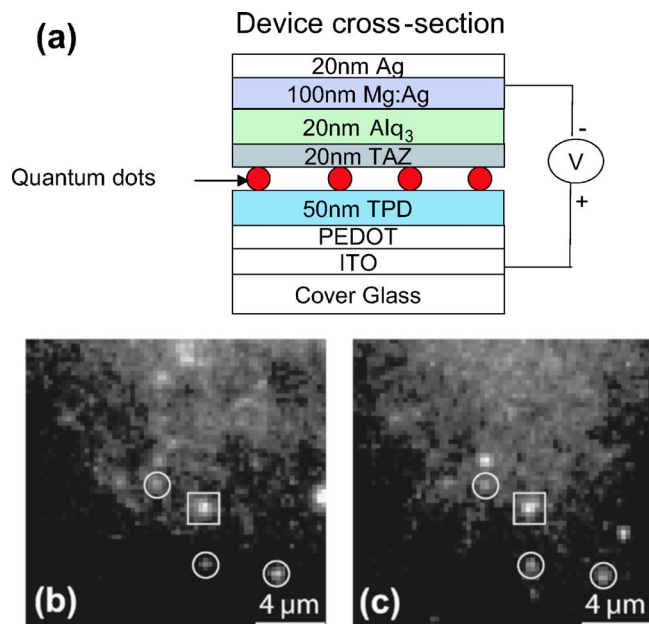


FIG. 1. (Color online) (a) Schematic representation of the cross section of a single quantum dot LED (not to scale). [(b) and (c)] Images of the same device area taken through a bandpass filter from 630 to 680 nm. (b) Photoluminescence image under laser excitation at 514 nm wavelength. (c) Electroluminescence image at a bias of 16 V. The circles highlight QDs that blink both in PL and EL (see supplemental movies), while the bright spot in the square changes its brightness only slightly and probably constitutes a cluster of QDs.

are individual QDs.^{15,16} Some of the brightest spots only varied slightly in intensity, and these are likely clusters of QDs.

Obtaining EL spectra from single QDs is complicated by their low emission intensity and the overlapping red tail of EL from the organic films. An EL spectrum containing a strong contribution from a single QD is shown in Fig. 2(a).

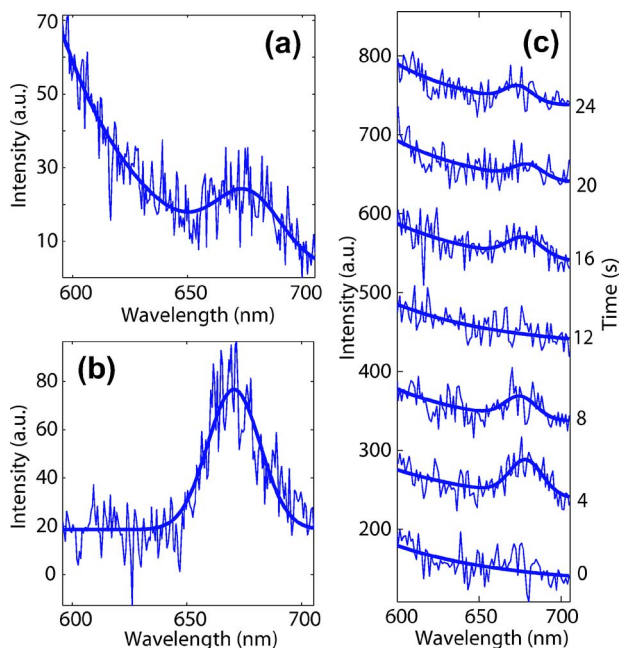


FIG. 2. (Color online) (a) Spectrum of the electroluminescence from a single QD at a bias of 18 V (noisy line). The spectrum was fitted with the sum of a single exponential decay term for the organic background and a Gaussian term for the QD contribution (smooth line). (b) Photoluminescence spectrum of the same QD with a Gaussian fit. (c) Time dependent spectra of the electroluminescence from a single QD with fits as in (a).

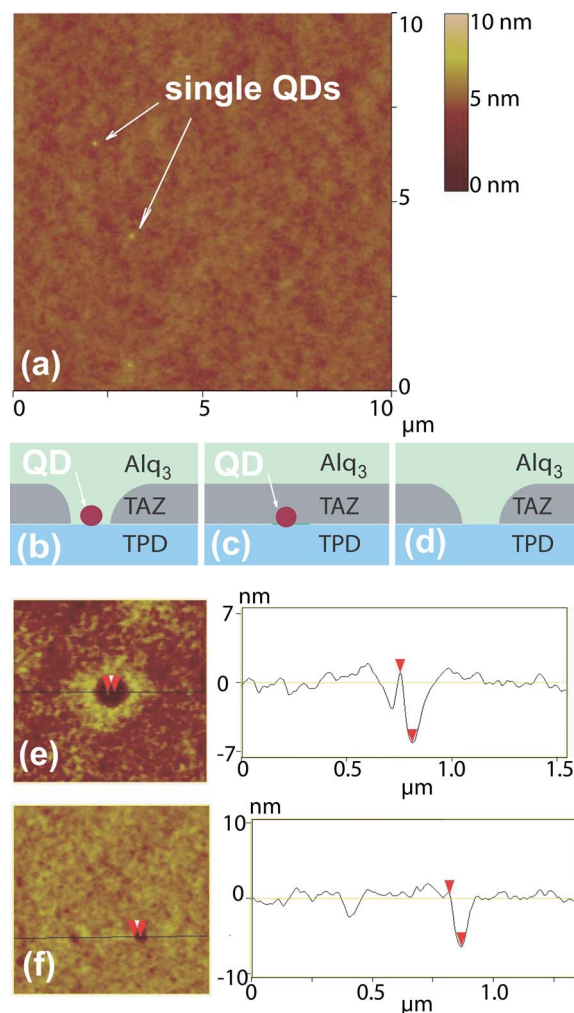


FIG. 3. (Color online) (a) AFM image of several single QDs on the surface of a TPD film after spin casting a TPD-QD solution. [(b)–(d)] Cross sections of hypothetical TPD/TAZ/Alq₃ interfaces (not to scale). [(e) and (f)] AFM images with section analysis showing the surface morphology of TAZ films on top of TPD-QD layers. (e) Possibly a QD in a pinhole of a TAZ film. (f) Pinhole in a TAZ film without an observable underlying QD.

The corresponding spectrum of the same QD in PL is shown in Fig. 2(b). Spectral diffusion and blinking, key features of single quantum dot fluorescence,^{15–17} can be seen in the time resolved spectral traces [Fig. 2(c)]. We note that some bright spots can only be observed either under laser excitation or in EL measurements. The EL from the organic films was also strongly enhanced at the positions of the bright spots as compared to the organic EL background of the rest of the device area.

In the following we present a model related to details of the device fabrication process to explain our findings. After the TPD-QD solution is spun onto PEDOT, the QDs phase separate from the TPD film and form a sparse QD layer on top of TPD, as illustrated in Fig. 3(a). The subsequently evaporated TAZ is chemically incompatible with the organic ligands that coat the surface of each QD, resulting in poor TAZ wetting of the QD sites,³ and consequent formation of channels through the TAZ film, as illustrated in Fig. 3(b). The absence of TAZ reduces the device resistance in the channels, facilitating higher current passage at QD sites, due to enhanced injection of holes from the TPD layer directly into the Alq₃ layer. Part of QD EL may be caused by direct charge injection into the QDs, which is the mechanism for

EL observed in MBE grown devices.¹¹ However, in our case, energy transfer from Alq₃ to the QDs is probably the dominant mechanism due to the proximity of Alq₃ molecules to the QDs in channels. We are able to observe both PL and EL from the QDs located in channels. It is possible that some of the QDs are covered entirely by TAZ, as illustrated by Fig. 3(c) and from these QDs we primarily observe PL and only weak EL, due to diminished energy transfer to QDs. A third possibility is that the TAZ film has pinholes even when no QDs are present [Fig. 3(d)]. The pinholes appear as bright spots in EL without a QD spectral contribution. Some channels could also contain QDs that are dark in PL and only switch on under bias due to charge rearrangement in their local environment.

The model above is supported by the enhanced EL from the organic films at all of the bright spots. Atomic force microscopy (AFM) studies on different layers of the device also support our hypothesis of current channels. The TPD-QD films display a smooth TPD surface [Fig. 3(a)] with a rms roughness of 0.3 nm, while the TAZ films on top of the TPD-QD layers are rougher with pinholes. In some scans [Fig. 3(e)], QDs appear to be located inside the pinholes. We also observed pinholes in TAZ films where no QDs were present [Fig. 3(f)].

In summary, we have observed EL from single colloidal QDs at room temperature. We propose a model in which pinholes form at the sites of individual QDs in the TAZ film. The lower device resistance in the pinholes leads to current channels that enhance the EL from QDs. The exact mechanisms of QD-EL and the electrostatics of single QDs in this environment warrant further investigation. Intentionally introducing channels into the TAZ film, e.g., by nanoindentation with an AFM¹⁸ could be an interesting way to control EL at the nanometer scale.

This research was funded by the HP-MIT Research Alliance, the Packard Foundation, a Presidential Early Career

Award for Scientists and Engineers (PECASE), and the NSF-MRSEC Program at MIT (DMR-D213282), allowing the use of its shared experimental facilities. One of the authors (A.D.) also acknowledges funding from the German National Science Foundation (DFG).

¹L. Brus, Appl. Phys. A: Solids Surf. **53**, 465 (1991).

²M. Han, X. Gao, J. Z. Su, and S. Nie, Nat. Biotechnol. **19**, 631 (2001).

³S. Coe, W.-K. Woo, M. G. Bawendi, and V. Bulovic, Nature (London) **420**, 800 (2002).

⁴W. U. Huynh, J. J. Dittmer, and A. P. Alivisatos, Science **295**, 2425 (2002).

⁵V. I. Klimov, A. A. Mikhailovsky, S. Xu, A. Malko, J. A. Hollingsworth, C. A. Leatherdale, H. J. Eisler, and M. G. Bawendi, Science **290**, 314 (2000).

⁶H.-J. Eisler, V. C. Sundar, M. G. Bawendi, M. Walsh, H. I. Smith, and V. Klimov, Appl. Phys. Lett. **80**, 4614 (2002).

⁷Y. Chan, J.-M. Caruge, P. T. Snee, and M. G. Bawendi, Appl. Phys. Lett. **85**, 2460 (2004).

⁸V. Zwiller, H. Blom, P. Jonsson, N. Panev, S. Jeppesen, T. Tsegaye, E. Goobar, M.-E. Pistol, L. Samuelson, and G. Björk, Appl. Phys. Lett. **78**, 2476 (2001).

⁹B. Lounis, H. A. Bechtel, D. Gerion, P. Alivisatos, and W. E. Moerner, Chem. Phys. Lett. **329**, 399 (2000).

¹⁰B. Fisher, J. M. Caruge, and M. G. Bawendi, Phys. Rev. Lett. **94**, 087403 (2005).

¹¹R. Schmidt, U. Scholz, M. Vitzethum, R. Fix, C. Metzner, P. Kailuweit, D. Reuter, A. Wieck, M. C. Hübner, S. Stufler, A. Zrenner, S. Malzer, and G. H. Döhler, Appl. Phys. Lett. **88**, 121115 (2006).

¹²X. Xu, D. A. Williams, and J. R. A. Cleaver, Appl. Phys. Lett. **85**, 3238 (2004).

¹³Z. Yuan, B. E. Kardynal, R. M. Stevenson, A. J. Shields, C. J. Lobo, K. Cooper, N. S. Beattie, D. A. Ritchie, and M. Pepper, Science **295**, 102 (2002).

¹⁴J. Zhao, J. Zhang, C. Jiang, J. Bohnenberger, T. Basché, and A. Mews, J. Appl. Phys. **96**, 3206 (2004).

¹⁵M. Nirmal, B. O. Dabbousi, M. G. Bawendi, J. J. Macklin, J. K. Trautman, T. D. Harris, and L. E. Brus, Nature (London) **383**, 802 (1996).

¹⁶M. Kuno, D. P. Fromm, H. F. Hamann, A. Gallagher, and D. J. Nesbitt, J. Chem. Phys. **112**, 3117 (2000).

¹⁷S. A. Empedocles and M. G. Bawendi, Science **278**, 2114 (1997).

¹⁸Y. F. Cao, C. Kim, S. R. Forrest, and W. Soboyejo, J. Appl. Phys. **98**, 033713 (2005).

Bias-Induced Photoluminescence Quenching of Single Colloidal Quantum Dots Embedded in Organic Semiconductors

Hao Huang,[†] August Dorn,[†] Gautham P. Nair,[†] Vladimir Bulović,^{*,‡} and Mounji G. Bawendi^{*,†}

Department of Chemistry, Electrical Engineering and Computer Science,
Massachusetts Institute of Technology, Cambridge, Massachusetts 02139

Received September 5, 2007; Revised Manuscript Received November 9, 2007

ABSTRACT

We demonstrate reversible quenching of the photoluminescence from single CdSe/ZnS colloidal quantum dots embedded in thin films of the molecular organic semiconductor *N,N*-diphenyl-*N,N*-bis(3-methylphenyl)-(1,1'-biphenyl)-4,4'-diamine (TPD) in a layered device structure. Our analysis, based on current and charge carrier density, points toward field ionization as the dominant photoluminescence quenching mechanism. Blinking traces from individual quantum dots reveal that the photoluminescence amplitude decreases continuously as a function of increasing forward bias even at the single quantum dot level. In addition, we show that quantum dot photoluminescence is quenched by aluminum *tris*(8-hydroxyquinoline) (Alq₃) in chloroform solutions as well as in thin solid films of Alq₃ whereas TPD has little effect. This highlights the importance of chemical compatibility between semiconductor nanocrystals and surrounding organic semiconductors. Our study helps elucidate elementary interactions between quantum dots and organic semiconductors, knowledge needed for designing efficient quantum dot organic optoelectronic devices.

Colloidal semiconductor nanocrystal quantum dots (QDs) have attracted considerable interest in recent years^{1–3} due to their spectral tunability, photostability, and chemical versatility. Incorporating colloidal nanocrystals into organic optoelectronic components, such as organic light-emitting devices (OLEDs)² and solar cells,^{4,5} has been demonstrated and appears promising. At the ensemble level, Ginger and Greenham have studied the interactions between conjugated polymers and CdSe nanocrystals.⁶ However, to date little is known about how individual nanocrystals are influenced by the surrounding organic semiconductor matrices. Here, we study interactions between single QDs and two archetypical organic semiconductors: the electron-conducting aluminum *tris*(8-hydroxyquinoline) (Alq₃) and the hole-conducting *N,N*-diphenyl-*N,N*-bis(3-methylphenyl)-(1,1'-biphenyl)-4,4'-diamine (TPD). We investigate the photoluminescence (PL) from QDs in solutions containing Alq₃ or TPD as well as from QDs embedded in evaporated thin films of these materials. Electrodes sandwiching the organic semiconductors allow us to apply an external voltage across the composite organic/QD thin films. Reversible modulation of the QD PL is observed under forward bias. We discuss QD PL

quenching mechanisms based on current flow and electric field in the organic/QD films.

The CdSe/ZnS (core/shell) QDs capped with trioctylphosphine oxide were obtained from Quantum Dot Corporation with an emission wavelength centered around $\lambda = 655$ nm. The QDs were first precipitated three times with butanol and methanol and then redispersed in anhydrous chloroform. Alq₃ was purchased from Tokyo Kasei Kogyo Co. Ltd. and purified by resublimation prior to use, while TPD was used as purchased from H.W. Sands Corp.

Quantum dots in solutions containing different concentrations of dissolved Alq₃ or TPD were excited with $\lambda = 525$ nm light generated by a frequency doubled Ti:Sapphire laser. The resulting time-resolved spectra were collected with a streak camera. A band-pass filter ($\lambda = 630$ nm to $\lambda = 680$ nm) was used to suppress emission from the organics and the laser.

The concentration of QDs in chloroform (99%, anhydrous) was ~ 0.04 μ M. Solution A-1 (A-2) was made by adding 1 mg (15 mg) of Alq₃ to 1 mL of QD solution and stirred until the Alq₃ was completely dissolved. Solution A-2 was kept in the dark for ~ 2 h for this mixing process. Equivalently, two other QD/TPD solutions, T-1 and T-2, were prepared by adding TPD to solvated QDs. A streak camera spectral window of $\lambda = 642$ nm to $\lambda = 668$ nm was

* Corresponding authors. E-mail: (M.G.B.) mgb@mit.edu; (V.B.) bulovic@mit.edu.

[†] Department of Chemistry.

[‡] Electrical Engineering and Computer Science.

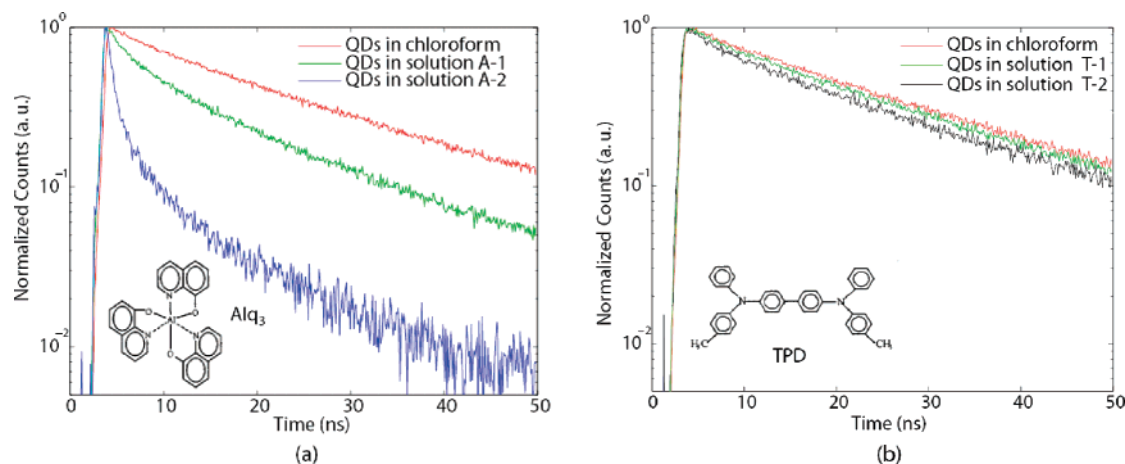


Figure 1. Photoluminescence lifetime measurements of QDs in chloroform solutions containing (a) different concentrations of Alq_3 and (b) different concentrations of TPD. Chemical formulas of Alq_3 and TPD are indicated.

monitored and recorded to determine the luminescence lifetimes of the QDs in different solutions. The PL lifetime of QDs in pure chloroform is ~ 20 ns. As shown in Figure 1, the QD PL lifetimes of QDs are significantly shortened by Alq_3 , while TPD minimally affects QD luminescence. We suspect that 8-hydroxyquinoline functional groups in Alq_3 quench QD PL by interacting with the QD surface. This assumption is consistent with the observation that the PL of QDs in solution is also suppressed when quinoline or 8-hydroxyquinoline is added (data not shown). Förster energy transfer from the QDs to Alq_3 molecules is not probable because of fast exciton relaxation⁷ to the band edge of the QDs, which is to the red of the absorption band of Alq_3 . TPD on the other hand does not have chelating groups, which explains why no quenching of the PL was observed in solutions T-1 and T-2.

All the measurements above were carried out in dilute QD solutions, while in active optoelectronic devices QDs are embedded in thin solid films.^{2,8} To study QD PL in condensed molecular films, we prepared substrates by first RF sputtering 80 nm thick ITO electrode strips through a shadow mask onto 0.13 mm thick cover glass slides. Then a PEDOT solution (BAYTRON CH8000) was spun onto the glass/ITO substrates at 3000 rpm and baked for 30 min. Schematics of the cross-sections of the organic/QD thin film structures with the corresponding electron energy level diagrams are shown in Figure 2. For the device shown in Figure 2a, TPD was added to the QD chloroform solution at a concentration of 10 mg/mL, and the resulting QD/TPD solution was spun onto the device substrates at 3000 rpm in a nitrogen glove box forming a ~ 50 nm thick film.⁸ As described previously, QDs float to the TPD surface due to phase separation.² The substrates were then transferred into an evaporator without exposing them to atmosphere, where a 70 nm thick TPD film was deposited at a background pressure of 6×10^{-7} Torr. Then, 100 nm Ag–Mg/20 nm Ag top electrode strips were evaporated through a shadow mask orthogonal to the ITO strips. Rectangular devices with areas of about 2.3 mm^2 each were formed at the intersections of the top and bottom electrodes. For the device shown in Figure 2b, QDs dissolved in chloroform were spun onto a

paralene-C coated PDMS stamp at 3000 rpm in a nitrogen glove box. The QDs were then stamped onto a 40 nm thick Alq_3 film that had previously been evaporated onto a PEDOT/ITO/glass substrate.⁹ After stamping, a 40 nm thick Alq_3 layer was evaporated onto the QD layer, and Ag–Mg/Ag top electrodes were added as described above. The devices were then packaged in a nitrogen glove box with glass coverslips and UV curable epoxy to minimize device exposure to oxygen and humidity and were mounted onto an xyz piezo-stage for measurement.

The $\lambda = 514$ nm line of an Ar-ion laser with an intensity of $\sim 10 \text{ W/cm}^2$ was used as an excitation source. Images were taken through the transparent ITO electrode using a $100\times$ oil immersion objective (Nikon) and an intensified charge-coupled device camera (Pentamax, Princeton Instruments) with a band-pass filter from $\lambda = 630$ nm to $\lambda = 680$ nm. The objective was focused on the fluorescence signal of the QDs under laser excitation, then a voltage was applied to the ITO electrode while the Ag–Mg electrode was grounded. At zero bias, it was easy to observe luminescence from individual QDs in TPD devices, while QD PL was strongly quenched in Alq_3 devices. These observations are consistent with our solution-based measurements (Figure 1). We note that QD PL quenching was less pronounced when QDs were located at an Alq_3 -glass or Alq_3 -PMMA interface (devices and measurements not shown). This could be due to the presence of dipole layers, surface charges, or a reduced surface coverage of the QDs by Alq_3 . We also find that Alq_3 degrades under laser excitation, leading to more QDs becoming visible as Alq_3 degrades. This was also observed for QDs embedded in TPD, however the effect was much less pronounced.

The PL signal from single QDs in Alq_3 is hard to observe even at zero bias, therefore we report only voltage-dependent PL quenching of QDs in TPD. As illustrated in Figure 3a, the decrease in PL intensity coincides with an increase in current flow through the device under forward bias. Under reverse bias, we do not observe any significant current, and PL from the QDs is not quenched. We expect that under reverse bias most of the voltage drops over a thin charge blocking layer at one or both of the organic/electrode

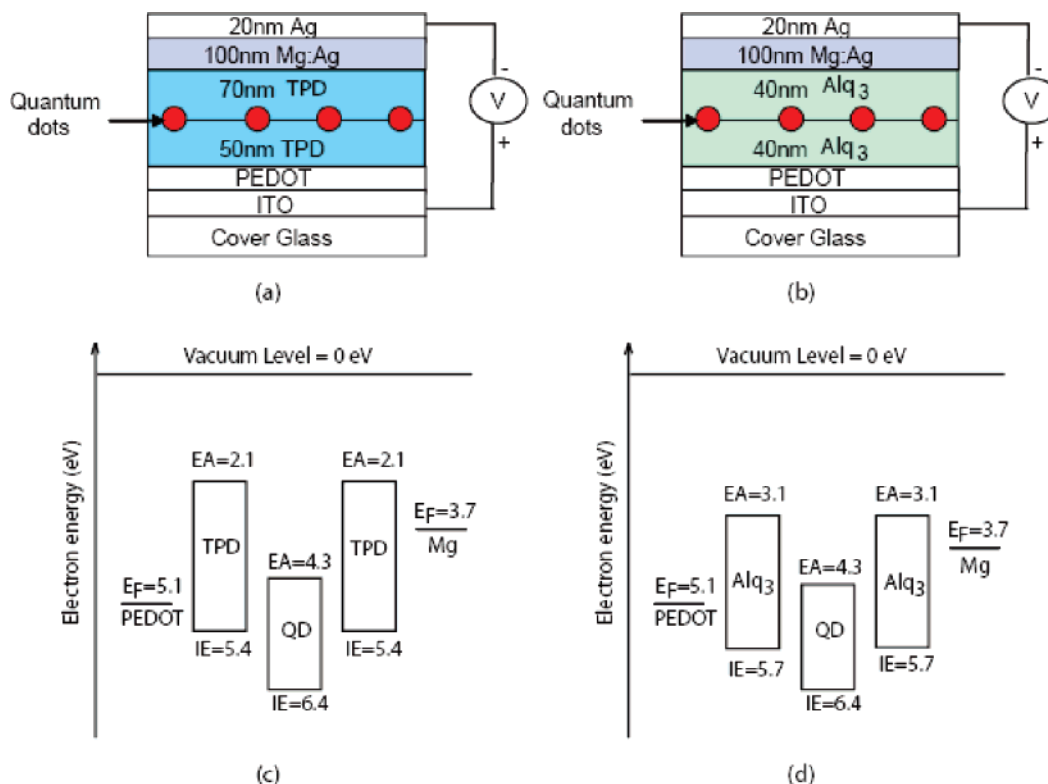


Figure 2. (a,b) Schematic representation of device cross-sections; (c,d) corresponding electron energy level diagrams (not to scale).

interfaces. In this case, the QDs are not exposed to increased electric fields or currents. When a positive voltage is applied to the ITO electrode, the voltage primarily drops across the bulk of the TPD layers, indicating that QDs located approximately at the center of the device are not only subject to an increasing current density, but also to an increasing electric field.¹⁰

The very dilute QD concentration in our devices enables us to monitor the fluorescence of individual QDs as a function of voltage (Figure 3b). This is of interest because it enables us to observe fluorescence intermittency, or “blinking”,^{11,12} of individual QDs as well as details of the turning off process that are lost in ensemble averaging. It should be noted that QDs embedded in TPD do not blink as digitally as QDs deposited on clean glass surfaces. The continuous decrease in intensity observed in Figure 3a could be the average of different single QD turning-off behaviors such as: (A) the QDs continue to blink with constant amplitudes but with longer off times or shorter on times or turn off abruptly at different voltages, as illustrated in Figure 4c, and/or (B) the on time amplitude decreases continuously, as illustrated in Figure 4d.

The voltage-dependent PL traces of individual QDs are compared with the ensemble average in Figure 3b. The PL intensity appears to decrease continuously even at the single QD level. To quantify this observation, we plot PL amplitude histograms of the blinking traces of 8 QDs, which were taken over a time period of 40 s with time bins of 0.1 s at a series of constant voltages (Figure 4g). The maximum PL amplitude of every QD at zero bias is normalized to 1. Therefore, at zero bias digital blinking (Figure 4a) leads to two distinct peaks: an “on time amplitude peak” close to 1, and an “off

time amplitude peak” close to 0 (Figure 4b). A shrinking on time amplitude peak, which remains fixed at a constant amplitude with increasing bias (schematic in Figure 4e), would indicate longer off times, shorter on times, or abrupt switching off of individual QDs, as proposed in (A). A continuous downward shift in amplitude of the on time amplitude peak (schematic in Figure 4f) on the other hand points toward a continuous decrease in single QD PL intensity, as proposed in (B). As shown in Figure 4g, the on time amplitude peak continuously shifts downward rather than remaining fixed at a constant amplitude and shrinking. This supports the picture proposed in (B).

Because the absorption cross section of QDs is not significantly altered by electric fields,¹³ the continuous decrease in PL intensity is the result of a field dependent increase in the ratio of nonradiative to radiative relaxation rates. The field-dependent quenching could be due to the following three mechanisms: (I) Excitons in the QDs are dissociated by the electric field, thus preventing radiative recombination.^{14,15} (II) Charge carriers hopping on and off the QDs quench the fluorescence when an excess charge resides in the QD due to an Auger process.^{16–18} (III) Excitons in the QDs transfer their energy to the loosely bound charge carriers participating in current flow through the surrounding organic. This mechanism is conceptually similar to the quenching of fluorophores on a metal surface.^{19,20}

Jarosz et al.¹⁵ have demonstrated that electric fields in excess of 10⁶ V/cm are necessary to completely field ionize excitons in QD films without ligand treatment. However, cap exchanging with shorter ligands can lead to complete exciton ionization at fields as low as 2 × 10⁵ V/cm.¹⁵ In our device, the electrical field strength at the position of the QDs

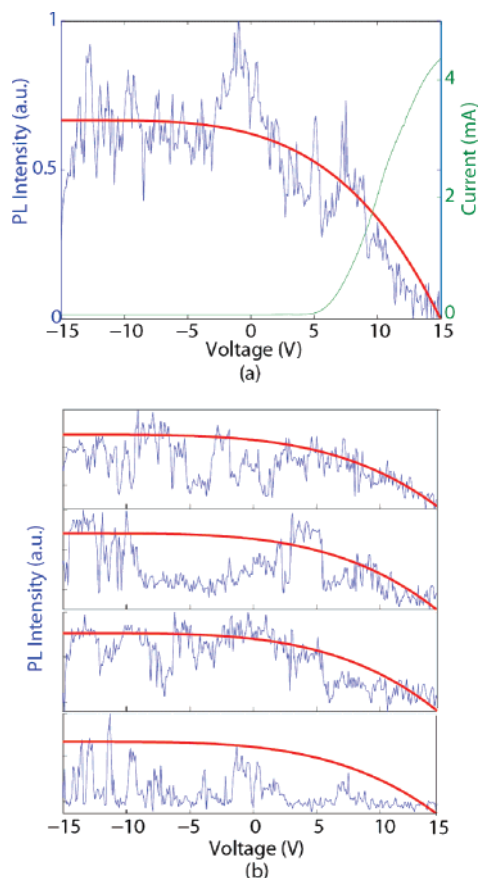


Figure 3. (a) Current–voltage characteristic of the TPD/QD/TPD device of Figure 2a (green curve) and corresponding voltage-dependent PL intensity (blue curve) averaged over 13 QDs. The solid red curve serves as a guide to the eye. (b) PL intensity voltage traces (blue curves) of four individual quantum dots contained in the ensemble. The red curves have the same intensity profile as the red curve in (a).

is linearly approximated as $E = U/d$ under forward bias,¹⁰ where U is the voltage applied across the electrodes and d is the thickness of the organic film. In Figure 3a, we observe near complete QD PL quenching at 15 V corresponding to a field of 10^6 V/cm. Field-induced exciton ionization is more efficient in our devices than in untreated QD films due to the shorter tunneling distance from a QD to a TPD molecule, as compared to the tunneling distance from one QD to the next as considered by Jarosz et al. It is also energetically more favorable for holes to tunnel from a QD to TPD (Figure 2c) than to a neighboring QD. As bias increases, the tunneling rate also increases resulting in PL quenching of the QDs. An increasing exciton ionization rate with increasing bias is also consistent with a continuous decrease in PL amplitude at the single QD level.

To understand the possible contributions from quenching mechanisms II and III, we consider the charge carrier density and the current density at complete quenching around 15 V. TPD thin films are primarily hole conducting with a hole mobility $\mu \sim 10^{-3}$ cm²/Vs.²¹ The hole density ρ is given by

$$\rho = \frac{I}{qS\mu E}$$

where q , S , and I represent unit charge, device area, and

current, respectively. At a bias of 15 V, the hole density is on the order of $\sim 10^{15}$ holes/cm³, which corresponds to one charge carrier in a cube with a side length of ~ 100 nm. According to the energy band diagram in Figure 2c, the valence band energy level offset between the QDs and TPD impedes hole-injection into the QDs. However, even if hole injection into the QDs were not impeded, for example, due to Fermi level pinning or the presence of surface dipoles, the rate j of holes passing through the cross section of a QD is given by

$$j = \mu E \pi R^2 \rho$$

where R denotes the radius of a QD, which is ~ 4 nm. The device shows nearly complete QD PL quenching at a bias of 15 V and a current of ~ 4 mA (Figure 3a), which corresponds to $j = 5 \times 10^5$ hole/s. Within the exciton lifetime of a QD, ~ 20 ns as measured in solution, there are only $\sim 10^{-2}$ holes passing through the cross-sectional area of a QD. Therefore, charging of the QDs due to current should result at most in quenching on the order of 1%. If holes do not pass through the QDs but remain trapped in the QDs for longer periods of time, this value could be significantly higher. However, the continuous decrease in PL amplitude at the single QD level indicates that the trapping time for charge carriers in a QD must be significantly lower than the binning time of 0.1 s. In addition, it is energetically unfavorable for holes to reside on the QDs, due to the band alignment between the QDs and the surrounding TPD as shown in Figure 2c. Therefore, this scenario appears unlikely. Nearby charge carriers can also quench the QDs through energy transfer. In this case, the QD radius has to be replaced by the Förster radius between a charge carrier and a QD. Assuming a Förster radius of ~ 5 nm,²² which is close to the radius of a QD, the probability of energy transfer from a QD to a charge carrier is of the same order of magnitude as for charge injection, which is $\sim 1\%$.

The quenching process is reversible, as demonstrated in Figure 5. The averaged intensity of many individual QDs could be reversibly modulated by $\sim 90\%$ (Figure 5a,c). The turning on and off times are below 5 s and are limited by a convolution of the RC constant of the device, charge rearrangement, and trap filling in the TPD, as well as the time constants of the quenching mechanisms. The continuous decrease in on-time amplitude of individual QDs with increasing electric field as discussed above indicates that the time scale of the quenching mechanism is faster than the binning time of 0.1 s. Therefore, the time constant of the quenching mechanism is not the limiting factor for the turning on and off times.

Given the relatively low carrier density and unfavorable charge injection into QDs, it is therefore likely that electric field-induced exciton ionization is the dominant PL quenching mechanism under forward bias. This interpretation is consistent with results on the electric field-induced quenching of the emission from phosphorescent organic solid-state molecular systems²³ as well as QD films.¹⁵ However, some contributions from quenching mechanisms II and III cannot be ruled out.

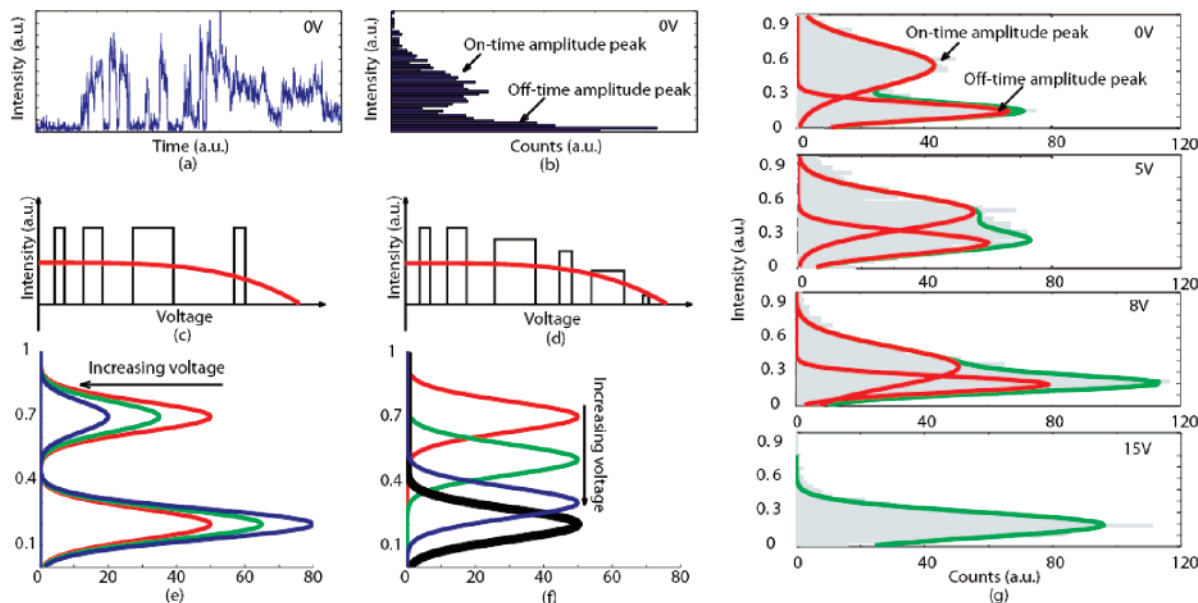


Figure 4. (a) PL intensity trace as a function of time (blinking trace) of an individual QD at 0 V and (b) the corresponding histogram of the PL intensity. (c,d) Schematics illustrating two different turning-off behaviors of individual QDs resulting in the same ensemble averaged PL intensity voltage trace (red curve) and (e,f) corresponding schematics of histograms of the PL intensity at three constant voltages (red, green, and blue). The black curve in (f) is the off-time amplitude peak, which does not vary with voltage. (g) Histograms of the PL intensity distribution of 8 individual QDs at four different constant voltages. At 0, 5, and 8 V, the histograms are fitted with two Gaussians (red curves) representing the on-time and off-time amplitude peaks; the green curves are the sum of the two red curves. At 15 V all the QDs are assumed to be off, so the histogram is fitted with one Gaussian only (green curve).

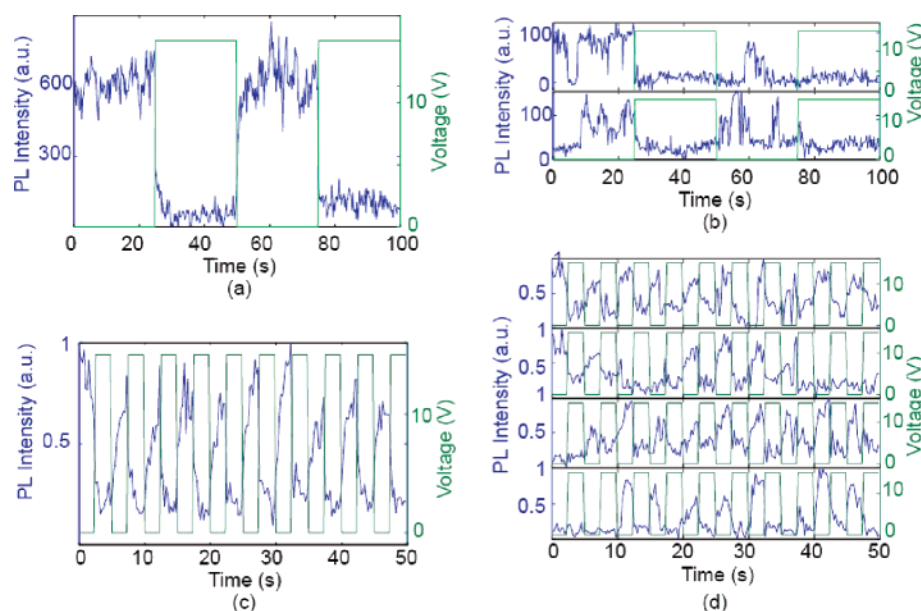


Figure 5. (a,c) Reversible modulation of the PL intensity averaged over 13 individual QDs as a function of voltage. (b,d) Blinking traces of individual QDs under voltage modulation contained in the ensemble averages shown in (a,c), respectively.

We studied the photophysics of quantum dots in solutions and thin film devices containing Alq₃ and TPD. In solution, the fluorescence lifetime of QDs is significantly shortened in the presence of Alq₃, while TPD has little effect. Solutions of quinoline or 8-hydroxyquinoline (the chelating group contained in Alq₃) also quench QD PL. This result highlights the importance of chemical compatibility for devices containing organics and QDs. The solution-based results are consistent with our measurements on QDs embedded in solid-state devices at zero bias. By applying a bias across

devices containing QDs embedded in TPD, we can reversibly modulate the photoluminescence intensity of the QDs by 90%. An analysis of several possible quenching mechanisms indicates that field-induced ionization dominates QD PL quenching, which implies that QDs should not be placed in high electric field regions within QD-LED structures. Voltage-dependent PL traces of individual QDs demonstrate that the on-time amplitude of individual QDs decreases continuously as the forward bias increases, consistent with electric field-induced ionization of QD excitons.

Acknowledgment. This research was funded by the HP-MIT Research Alliance, a Presidential Early Career Award for Scientists and Engineers (PECASE), the NSF-MRSEC Program at MIT (DMR-0213282), making use of its shared experimental facilities, the NSF-NSEC Program (DMR-0117795), and an NSF-NIRT (CHE-0507147). A.D. also acknowledges funding from the German National Science Foundation (DFG).

References

- (1) Alivisatos, A. P.; Gu, W.; Larabell, C. *Ann. Rev. Biomed. Eng.* **2005**, *7*, 55.
- (2) Coe, S.; Woo, W.-K.; Bawendi, M. G.; Bulovic, V. *Nature* **2002**, *420*, 800.
- (3) Konstantatos, G.; Howard, I.; Fischer, A.; Hoogland, S.; Clifford, J.; Klem, E.; Levina, L.; Sargent, E. H. *Nature* **2006**, *442*, 7099.
- (4) Greenham, N. C.; Peng, X.; Alivisatos, A. P. *Phys. Rev. B* **1996**, *54*, 17628.
- (5) Huynh, W. U.; Dittmer, J. J.; Alivisatos, A. P. *Science* **2002**, *295*, 2425.
- (6) Ginger, D. S.; Greenham, N. C. *Phys. Rev. B* **1999**, *59*, 10662.
- (7) Klimov, V.; McBranch, D. W. *Phys. Rev. Lett.* **1998**, *80*, 4028.
- (8) Huang, H.; Dorn, A.; Bulovic, V.; Bawendi, M. G. *Appl. Phys. Lett.* **2007**, *90*, 023110.
- (9) Kim, L. Master Thesis, Massachusetts Institute of Technology, Cambridge, MA, 2006.
- (10) Schwoerer, M.; Wolf, H. C. *Organische Molekulare Festkorper*; WILEY-VCH: New York, 2005.
- (11) Nirmal, M.; Dabbousi, B. O.; Bawendi, M. G.; Macklin, J. J.; Trautman, J. K.; Harris, T. D.; Brus, L. E. *Nature* **1996**, *383*, 802.
- (12) Kuno, M.; Fromm, D. P.; Johnson, S. T.; Gallagher, A.; Nesbitt, D. *J. Phys. Rev. B* **2003**, *67*, 125304.
- (13) Sacra, A. Doctoral Thesis, Massachusetts Institute of Technology, Cambridge, MA, 1996.
- (14) Rothenberg, E.; Kazes, M.; Shaviv, E.; Banin, U. *Nano Lett.* **2005**, *5*, 1581.
- (15) Jarosz, M. V.; Porter, V. J.; Fisher, B. R.; Kastner, M. A.; Bawendi, M. G. *Phys. Rev. B* **2004**, *70*, 195327.
- (16) Woo, W. K.; Shimizu, K. T.; Jarosz, M. V.; Neuhauser, R. G.; Rubner, M. A.; Bawendi, M. G. *Adv. Mater.* **2002**, *14*, 1068.
- (17) Efros, A. L.; Rosen, M. *Phys. Rev. Lett.* **1997**, *78*, 1110.
- (18) Shim, M.; Wang, C. J.; Guyot-Sionnest, P. *J. Phys. Chem. B* **2001**, *105*, 2369.
- (19) Chance, R. R.; Prock, A.; Silbey, R. J. *Adv. Chem. Phys.* **1978**, *37*, 1.
- (20) Barnes, W. L. *J. Mod. Opt.* **1998**, *45*, 661.
- (21) Stolka, M.; Janus, J. F.; Pai, D. M. *J. Phys. Chem.* **1984**, *63*, 4707.
- (22) Kagan, C. R.; Murray, C. B.; Nirmal, M.; Bawendi, M. G. *Phys. Rev. Lett.* **1996**, *76*, 1517.
- (23) Kalinowski, J.; Stampor, W.; Mezyk, J.; Cocchi, M.; Virgili, D.; Fattori, V.; Di Marco, P. *Phys. Rev. B* **2002**, *66*, 235321.

NL072263Y

Micropatterning metal electrode of organic light emitting devices using rapid polydimethylsiloxane lift-off

Jennifer Yu^{a)} and Vladimir Bulović

Laboratory of Organic Optics and Electronics, Electrical Engineering and Computer Science Department, Massachusetts Institute of Technology, Cambridge, Massachusetts 02139

(Received 22 May 2007; accepted 25 June 2007; published online 23 July 2007)

The authors demonstrate a subtractive stamping technique for patterning metal electrodes of organic light emitting devices. Patterning is achieved by placing a relief patterned polydimethylsiloxane stamp in contact with a planar metal electrode film and subsequently peeling off the stamp. A fast peel rate increases the weak adhesion energy of the stamp to the metal so that no surface treatment, pressure, or temperature control is necessary to lift-off the metal film in contact with the stamp. Patterning is dependent on metal film thickness, geometry of the features, and peel direction of stamp release. The minimum feature size patterned is 13 μm wide stripes within $<1 \mu\text{m}$ in-plane edge roughness and 0.1 μm height transition region of the patterned edge. © 2007 American Institute of Physics. [DOI: 10.1063/1.2759466]

Fabrication of high resolution arrays of organic electronic devices, in particular, organic light emitting devices (OLEDs), would benefit from the ability to pattern micron sized features of top array electrodes. Presently, the dominant commercial technique for patterning top electrodes is a low-pressure physical deposition of metal vapor through a shadow-mask stencil, a technique which is, unfortunately, limited in resolution and scalability. The thickness of the stencil and the control of the stencil proximity to the substrate set the pattern quality, where for the highest resolution thin shadow masks are needed, but these are susceptible to warping and distortion under their own weight, limiting the ability to scale shadow-mask processing to large array areas. Although it is possible to implement a scalable shifting shadow mask to pattern minimum feature sizes of 30 μm , as needed for a subpixel in a high resolution display, it is not without added complexity and cost.^{1,2} In addition, rigid masks are hard to adapt to patterning of curved substrate, as might be needed for roll-to-roll fabrication of structures on flexible substrates. Some alternative techniques for patterning the top electrode of OLEDs include pixel patterning through laser ablation,³ electrode lift-off,⁴ integrated shadow mask,⁵ and epoxy mold release.⁶ Each of these methods exhibits some shortcomings: the serial process of laser ablation is not readily scalable to large areas, electrode lift-off requires a wet etch that is potentially damaging to the organic layers, the integrated shadow mask relies on a geometry primarily used for patterning passive matrix displays, and epoxy mold release requires temperature and pressure control.

It has consequently been suggested that for a scalable electrode patterning solution one can use contact-stamping techniques where a relief stamp patterns the electrode on the raised features of the stamp.⁷ For example, in one proven contact-stamping method, cold-welding mechanism was used to promote adhesion of an unpatterned silver film to the rigid silver-coated silicon relief stamps under high contact pressures (290 MPa). The high pressure was required for fracturing the metal film at the pattern edges and for obtain-

ing intimate contact of a rigid stamp to the electrode surface in the presence of impurities.⁷ To reduce required pressures (to 190 MPa) and to eliminate the need to fracture the metal electrode during patterning, an additive stamping method was also demonstrated with a rigid gold-coated stamp and applied to patterning organic field effect transistors (OFETs).⁸ Improvement on this technique used a flexible stamp made of polydimethylsiloxane (PDMS), a two-part silicone elastomer with a low Young modulus, to dramatically lower the pressure required to make conformal contact with the electrode (to 180 kPa).⁹ Finally, additive transfer of OFET electrodes relying on temperature controlled adhesion has been demonstrated but without the release layer for the relief PDMS stamp because of the poor adhesion of the metal to the PDMS.¹⁰

Simplifying further the earlier contact-stamping techniques, the present work demonstrates subtractive contact stamping for patterning OLED electrodes using a relief PDMS stamp and, in contrast to earlier studies, requiring no applied pressure, temperature control, or stamp surface modification.¹¹ The patterning is enabled by the kinetically controlled adhesion of the PDMS relief stamp to the surface to be patterned. For example, patterning of a planar metal film coating a substrate is accomplished by forming a mechanical contact with the PDMS relief stamp, where the strength of the PDMS/metal film bond is controlled by the rate of peel of PDMS away from the substrate. When PDMS stamp is rapidly separated from the substrate, the energy release rate of PDMS can increase by an order of magnitude, ensuring strong PDMS/metal adhesion, and portion of the metal film in contact with PDMS will be pulled away from the substrate forming a pattern. It has already been demonstrated that the adhesion to the stamp can be sufficiently strong to enable removal of planar structures that are even ionically bonded to the donor substrate.¹² A subtractive patterning technique which relies on the same adhesion mechanism has been recently developed for patterning organic layers of an OFET.¹³

Our subtractive electrode stamping technique is applied

^{a)}Electronic mail: jenyu@mit.edu

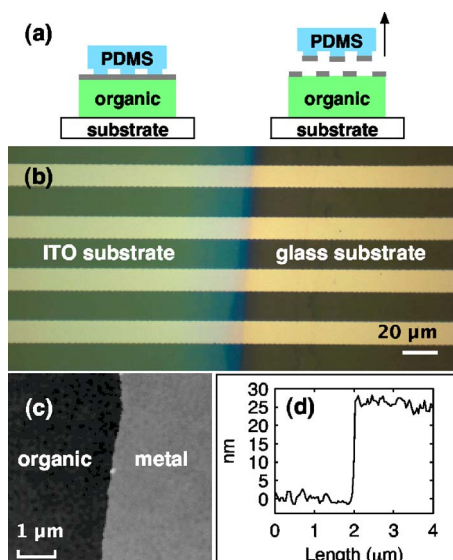


FIG. 1. (Color online) Schematic depiction of PDMS lift-off technique for patterning metal electrodes in organic devices. Metal layer deposited on top of organic substrate is detached from the substrate surface when (a) patterned PDMS relief stamp makes conformal contact with the surface and is followed with a rapid peel off. (b) 13 μm wide lines of patterned 20 nm thick Mg:Ag on top of 50 nm thick Tris-(8-hydroxyquinoline)aluminum (Alq₃)/50 nm thick *N,N'*-Bis(3-methylphenyl)-*N,N'*-bis(phenyl)-benzidine (TPD)/poly(3,4-ethylenedioxythiophene)poly(styrenesulfonate) (PEDOT:PSS)/ITO/glass on left and on top of glass substrate on right (c) atomic force microscope (AFM) image of a sample similar to that in (b) with a corresponding AFM cross section shown in (d).

in ambient conditions to patterning a metal electrode in an OLED stack (Fig. 1). We first form the PDMS stamp by mixing a 1:10 weight ratio of PDMS (Dow Corning Sylgard® 184 silicone elastomer) curing agent to base. This mixture is then poured into a petri dish containing the silicon masters with a relief pattern of 2 μm depth, placed under low vacuum until no bubbles are observed escaping out of the viscous PDMS mixture, and baked at 60 °C for at least 5 h. The cured stamp is then released from the petri dish and silicon masters and sectioned into 1 cm³ cubes. For peel direction experiments, the stamp thickness was reduced to 0.2 cm. The PDMS relief stamp is then placed in a mechanical contact with the metal electrode of the OLED thin film stack, with the raised features of the stamp establishing a conformal contact with the metal electrode, without any applied pressure. The conformal contact occurs even on surfaces that are not flat, such as a glass/indium tin oxide (ITO) step.

With a slow peel rate of the PDMS stamp away from the substrate (~10 mm/s), the metal film remains intact and is not lifted off, which is consistent with static interfacial adhesion analysis, since the static PDMS-metal work of adhesion ($W_{\text{PDMS,Mg:Ag}} = 16\text{--}18 \text{ mJ/m}^2$) is smaller than metal-organic ($W_{\text{Mg:Ag,Alq}_3} = 65\text{--}96 \text{ mJ/m}^2$), organic-organic ($W_{\text{Alq}_3,\text{TPD}} = 43\text{--}54 \text{ mJ/m}^2$), or organic-substrate work of adhesion ($W_{\text{TPD,ITO}} = 36\text{--}42 \text{ mJ/m}^2$).¹¹ However, with a rapid peel rate of the PDMS stamp away from the substrate ($\geq 10 \text{ mm/s}$), the adhesion between the PDMS and metal interface increases due to the kinetic increase in the adhesion strength, and is able to overcome adhesion between the metal or organic interfaces, allowing lift-off of the metal film from the substrate. Besides our work,¹¹ the same adhesion analysis

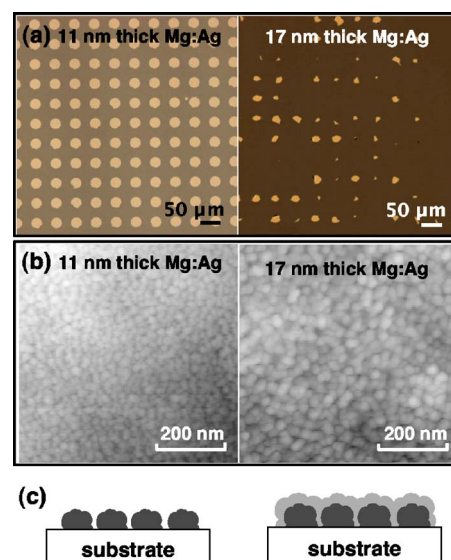


FIG. 2. (Color online) (a) Optical micrograph of 25 μm diameter circles patterned from Mg:Ag on top of 50 nm thick Alq₃/40 nm thick *N,N'*-Bis(3-methylphenyl)-*N,N'*-bis(phenyl)-9,9-spirobifluorene/PEDOT:PSS/glass with metal thickness indicated in the figure. For a given pattern, increasing metal film thickness results in lift-off but not patterning of the metal film. (b) Corresponding AFM images of metal electrode surface indicate larger grain size for thicker film. (c) Cartoon depiction of the difficulty in patterning thicker films due to the increased grain size and continuous nature of the film.

has recently been applied to quantifying pattern formation in pentacene OFET films.¹³ Note that our work of adhesion calculation is based on contact angle measurements¹⁴ using ethylene glycol and water on various surfaces. Maximum and minimum contact angles were used in the work of adhesion calculation, resulting in the above stated range of values.

To generate a pattern with this subtractive contact-stamp patterning method, metal film fracture must occur at the edges of the stamp relief features, similar to the cold-welding process.⁷ Externally applied pressure across the PDMS stamp is ineffective in forming the metal layer fracture, as it simply leads to the distortion of the flexible stamp. Consequently, in our demonstrations we use thin layers of metal which are easy to fracture in a lift-off process because of reduced cross sectional area of the film, less continuity in the film, and smaller grain sizes of the metal that constitutes the film. We find that the ability to pattern a metal film is also dependent on the geometry of the pattern. As an example in Fig. 2, we show good pattern transfer in metal films with layer thickness of 11 nm for 25 μm diameter circle pattern. Increasing metal film thickness leads to complete metal electrode removal instead of patterned removal of the film during the PDMS lift-off process (Fig. 2). We find that in transfer of line patterns, better quality image transfer occurs when the peel direction of separating the PDMS stamp away from the substrate is aligned with the relief line pattern. Peeling along the line pattern direction assists propagation of the metal film fracture. In contrast, peeling in the direction perpendicular to the relief stamp line pattern leads to poor pattern definition, since the breakage and release of the metal film must repeatedly occur in a discontinuous fashion. Examples of the peel-dependent pattern transfer quality are shown in Fig. 3. We note that the metal films become increasingly difficult to lift-off as the film thickness is decreased below 10 nm.

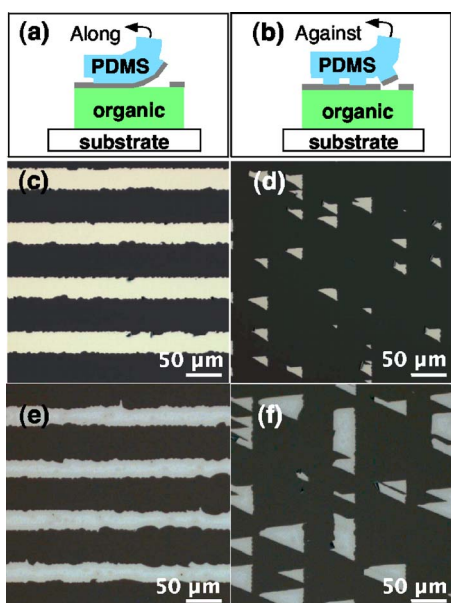


FIG. 3. (Color online) Peel direction along (a) or perpendicularly against (b) line pattern of the relief stamp affects patterning lift-off of 20 nm thick Ag [(c) and (d)] or 12.5 nm thick Mg:Ag [(e) and (f)] film on top of 50 nm thick Alq_3 /50 nm thick TPD/ITO/glass. Optical micrographs show that peel along [(c) and (e)] the line pattern results in patterning of 30 μm wide lines with edge roughness of up to $\pm 5 \mu\text{m}$, while peel against [(d) and (f)] the line pattern does not result in good pattern transfer.

Using the PDMS lift-off process, we patterned the top electrode of an OLED and compared the operating characteristics to an OLED whose top electrode is patterned by shadow masking. The two devices are grown on the same $1 \times 1 \text{ in.}^2$ substrate using shadow-mask patterning on half of the substrate. After device growth, half of the substrate is patterned using PDMS lift-off technique. Figure 4 shows nearly identical current density versus voltage and electroluminescence quantum efficiency characteristics for the two devices, indicating equivalent quality of the PDMS lift-off and shadow-masked structures.

In summary, we demonstrated a simple and scalable method for patterning thin Mg:Ag or Ag electrodes using a PDMS stamp and no externally applied pressure or chemical surface treatment. Unlike previous demonstrations of subtractive patterning of electrodes, this technique does not rely on cold welding or pressure-induced electrode fracture. We applied the relief stamp peel-off method in patterning OLED electrodes, demonstrating equivalent performance to the OLEDs patterned by shadow masking.

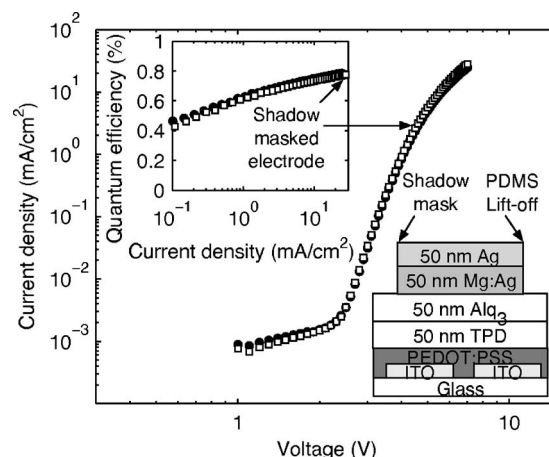


FIG. 4. Current density vs voltage characteristics of a 2.81 mm^2 area organic light emitting device (OLED) patterned by PDMS lift-off. The completed device consists of 50 nm thick Mg:Ag/50 nm thick Ag on top of 50 nm thick Alq_3 /50 nm thick TPD/PEDOT:PSS/ITO/glass. Also shown are current density vs voltage characteristics of a 4.34 mm^2 area OLED patterned by conventional shadow-mask method. (Inset) External electroluminescence quantum efficiency vs current density for the same devices. Device structure is shown on the bottom right.

The authors gratefully acknowledge the funding support from MIT, Institute for Soldier Nanotechnologies, and Presidential Early Career Award for Scientists and Engineers (PECASE).

- ¹P. F. Tian, V. Bulovic, P. E. Burrows, G. Gu, S. R. Forrest, and T. X. Zhou, *J. Vac. Sci. Technol. A* **17**, 2975 (1999).
- ²K. Utsugi, M. Tamegai, and E. Hasegawa, *SID 2000 Digest*, 2000, p. 640.
- ³S. Noach, E. Z. Faraggi, G. Cohen, Y. Avny, R. Neumann, D. Davidov, and A. Lewis, *Appl. Phys. Lett.* **69**, 3650 (1996).
- ⁴P. F. Tian, P. E. Burrows, and S. R. Forrest *Appl. Phys. Lett.* **71**, 3197 (1997).
- ⁵Z. H. Huang, G. J. Qi, X. T. Zeng, and W. M. Su, *Thin Solid Films* **503**, 246 (2006).
- ⁶Z. Wang, R. Xing, J. Zhang, J. Yuan, X. Yu, and Y. Han, *Appl. Phys. Lett.* **85**, 831 (2004).
- ⁷C. Kim, P. E. Burrows, and S. R. Forrest, *Science* **288**, 831 (2000).
- ⁸C. Kim, M. Shtein, and S. R. Forrest, *Appl. Phys. Lett.* **80**, 4051 (2002).
- ⁹C. Kim and S. R. Forrest, *Adv. Mater. (Weinheim, Ger.)* **15**, 541 (2003).
- ¹⁰Z. Wang, J. Yuan, J. Zhang, R. Xing, D. Yan, and Y. Han, *Adv. Mater. (Weinheim, Ger.)* **15**, 1009 (2003).
- ¹¹J. Yu and V. Bulovic, 2006 Materials Research Society Fall Meeting, 2006 (unpublished), p. S2.5.
- ¹²M. A. Meitl, Z.-T. Zhu, V. Kumar, K. J. Lee, X. Feng, Y. Y. Huang, I. Adesida, R. G. Nuzzo, and J. A. Rogers, *Nat. Mater.* **5**, 33 (2005).
- ¹³K.-H. Kim, K.-W. Bong, and H. H. Lee, *Appl. Phys. Lett.* **90**, 093505 (2007).
- ¹⁴Z. Wang, J. Zhang, R. Xing, J. Yuan, D. Yan, and Y. Han, *J. Am. Chem. Soc.* **125**, 15278 (2003).

Colloidal quantum-dot light-emitting diodes with metal-oxide charge transport layers

J. M. CARUGE^{1†}, J. E. HALPERT^{1†}, V. WOOD^{2†}, V. BULOVIĆ^{2*} AND M. G. BAWENDI¹

¹Department of Chemistry, Massachusetts Institute of Technology, Cambridge, Massachusetts 02139, USA

²Department of Electrical Engineering, Massachusetts Institute of Technology, Cambridge, Massachusetts 02139, USA

[†]These authors contributed equally to this work.

*e-mail: bulovic@mit.edu

Published online: 16 March 2008; doi:10.1038/nphoton.2008.34

Colloidal quantum dots, with their tunable luminescence properties, are uniquely suited for use as lumophores in light-emitting devices for display technologies and large-area planar lighting^{1–10}. In contrast to epitaxially grown quantum dots, colloidal quantum dots can be synthesized as highly monodisperse colloids and solution deposited over large areas into densely packed, solid-state multilayers, which have shown promise as efficient optical gain media¹¹. To be a viable platform for colour-tunable electrically pumped lasers, the present-generation quantum-dot LEDs must be modified to withstand the extended, high-current-density operation needed to achieve population inversion. This requirement necessitates a quantum-dot LED design that incorporates robust charge transport layers. Here we report the use of sputtered, amorphous inorganic semiconductors as robust charge transport layers and demonstrate devices capable of operating at current densities exceeding 3.5 A cm^{-2} with peak brightness of $1,950 \text{ Cd m}^{-2}$ and maximum external electroluminescence efficiency of nearly 0.1%, which represents a 100-fold improvement over previously reported structures^{8,10}.

Previous efforts at building colloidal quantum-dot (QD) LEDs with inorganic charge transport layers have demonstrated only limited quantum dot (QD) electroluminescence (EL) efficiency. One study placed a multilayer of QDs between indium tin oxide (ITO) and silver electrodes¹⁰. The low luminescence efficiency ($10^{-3} \text{ Cd A}^{-1}$) of these structures could be attributed to a number of sources, including luminescence quenching of the QDs by plasmon modes in the highly conductive electrodes¹², luminescence quenching by QD charging¹³, or low efficiency due to imbalance in the polarity of charges injected into the device, which could lead to excess background current¹⁴. More recent work using doped GaN transport layers surrounding colloidal QDs reported external quantum efficiencies (EQEs) of 0.001–0.01%, although much of the observed EL arose from the GaN (ref. 8). These devices exhibited non-uniform emission across the pixel area, and fabrication required the specialized deposition technique of energy-neutral atomic-beam lithography or epitaxy. In contrast to this early attempt, in the present work we demonstrate the first general method that reproducibly fabricates patterned, all-inorganic optoelectronic devices with functional QD

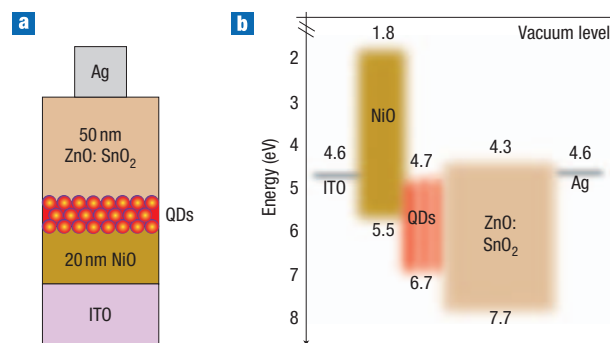


Figure 1 Quantum-dot light-emitting diode design. **a**, Schematic of the device structure showing the ITO anode, the Ni HTL, the QD active luminescent layer, the ZnO:SnO₂ ETL and the silver cathode. **b**, A band diagram determined from UV photoemission spectroscopy and optical absorption measurements, giving the approximate electron affinities and ionization energies of the QD-LED materials.

lumophores. We use amorphous, radiofrequency (RF)-sputtered metal oxides as QD-LED charge transport layers, deposited at room temperature to be broadly compatible with colloidal QDs and many other constituent films. With this advance, all-inorganic, QD-containing devices can, for the first time, be systematically engineered, as exemplified by our demonstration of QD-LEDs that manifest 100-fold higher EQEs than previously reported all-inorganic colloidal QD-LED structures.

We follow three main guidelines in the choice and preparation of the metal oxide charge transport layers. First, we chose mechanically smooth and compositionally amorphous films to prevent electrical shorts or the formation of preferred current channels through the device structure. Second, we grew semiconducting oxide films with low free-carrier concentrations to minimize quenching of the QD EL through free-carrier plasmon modes. Third, the hole transport layer (HTL) and the electron transport layer (ETL) were chosen to have similar free-carrier concentrations and energy-band offsets to the QDs so that electron and hole injection into the QD layer was balanced. An excess of one type of carrier in the QD region results in QD

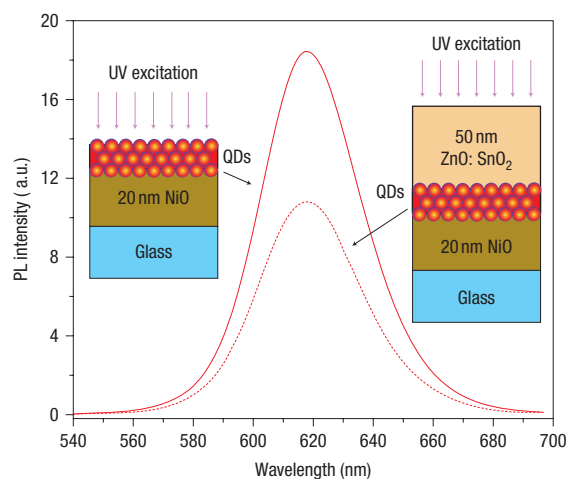


Figure 2 Effect of ZnO:SnO₂ layer deposition. Photoluminescence spectra before (solid line) and after (dotted line) deposition of a 50-nm-thick ZnO:SnO₂ layer onto ZnCdSe QDs on NiO. All the materials were deposited with the same conditions used for device fabrication, although this QD batch had a slightly different peak emission wavelength. Both samples were excited within the same optical geometry using a UV lamp. We measured a 40% drop in the PL intensity on average.

charging, which increases the likelihood of non-radiative three-body Auger relaxations¹² and therefore decreases EL efficiency. These requirements highlight the important benefits in using metal oxides as versatile charge transport layers; metal oxides offer a range of deposition-determined morphologies as well as tunable conductivities and adjustable ionization energies through doping and physical co-deposition.

The cross-section of our QD-LED is depicted in Fig. 1a with the approximate electronic band structure of constituent layers shown in Fig. 1b. Following our previous work on hybrid organic–inorganic QD-LED structures¹, the HTL of the present QD-LEDs was a 20-nm-thick film of NiO deposited on ITO. The resistivity of the NiO film was tuned to 5 Ω cm by adjusting the oxygen concentration in the Ar:O₂ plasma during the RF magnetron sputtering process^{15,16}. Hot-probe and X-ray-diffracted measurements indicate that as-grown NiO films are amorphous and p-type. Atomic force microscope (AFM) characterization of the NiO layer on top of the ITO electrodes revealed a root-mean-square roughness of <0.5 nm, which enables deposition of smooth monolayers of self-assembled QDs onto the NiO.

The luminescence layer of QD-LEDs consisted of ZnCdSe alloyed QDs with an emission peak at wavelength $\lambda = 638$ nm, a full-width at half-maximum (FWHM) of 40 nm, and a colloidal solution photoluminescence (PL) quantum yield of $50 \pm 10\%$. The thin-film photoluminescence efficiency is lower by an order of magnitude. The QDs were spin-coated onto the NiO substrate so as to form a 30 ± 5 nm film consisting of from 3 to 4 close-packed QD monolayers. We chose ZnCdSe cores over more traditional CdSe/ZnS core/shell QDs owing to their ease of production and because ZnCdSe alloyed QDs, which are not overcoated with a wide-bandgap ZnS layer, should enable easier charge injection into the QDs. In this study, our highest EL efficiencies were measured for QD-LEDs containing ZnCdSe QDs; however, devices containing CdSe/ZnS QDs show efficiencies within an order of magnitude.

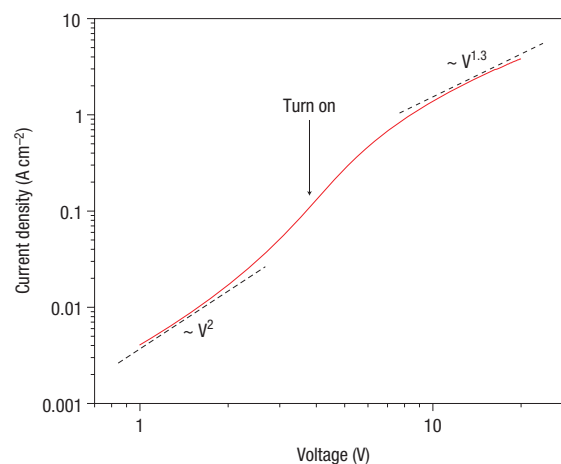


Figure 3 Quantum-dot light-emitting diode current–voltage characteristics. Current density versus voltage log–log plot for the QD-LED of Fig. 1a. Three different regimes of conduction are clearly visible. At low voltages the device shows space-charge-limited conduction. At 3 V, the slope of the J – V plot increases as both holes and electrons are injected into the QD, and the onset of EL is observed at 3.8 V. At higher V , the J – V behaviour tends to ohmic conduction.

For the ETL, we selected a 50-nm-thick, optically transparent film of alloyed ZnO and SnO₂, with a resistivity of 10 Ω cm. ZnO:SnO₂ alloy is an n-type semiconductor and, as shown schematically in Fig. 1b, its conduction-band level allows injection of electrons into the ZnCdSe QD conduction band. Whereas pure ZnO or SnO₂ films tend to be polycrystalline with pronounced grain boundaries, AFM and X-ray diffraction measurements indicate that ZnO:SnO₂ films are relatively smooth (with <0.5 nm r.m.s. roughness) and crystallographically amorphous, reducing the likelihood of morphologically induced electrical shorts in the device. Our choice of ZnO:SnO₂ also reflects the requirement that the ETL be sputtered directly onto the QDs without damaging them. Introducing O₂ into the sputtering gas, as with NiO, could oxidize the organic ligands capping the QDs and produce trap sites that facilitate non-radiative recombination of QD excitons. The ZnO:SnO₂ ratio determines the film conductivity, eliminating the need for excess oxygen in the sputtering process. To determine whether the ZnO:SnO₂ deposition causes physical damage to the QDs, we compared the UV-excited PL intensity from QDs on NiO and from QDs embedded in a NiO/QD/ZnO:SnO₂ structure. As shown in Fig. 2, we observed a 40% drop in intensity as a result of the ZnO:SnO₂ deposition, which indicates that sputtering the ETL on the QDs largely preserves the passivating ligands. In fact, much of the decrease in QD luminescence can be attributed to additional quenching by the free carriers in the ETL. A silver cathode was chosen to allow electron injection into the conduction band of the ZnO:SnO₂ layer.

All our QD-LEDs were tested in air over several days. The devices were tested as-made, without additional environmental packaging, and were stored in atmospheric conditions between experiments. Figure 3 shows the forward biased current density versus voltage (J – V) log–log plot for the QD-LED described above. The J – V slope with a gradient of two between 1 V and 3 V is indicative of space-charge-limited conduction for one of the carriers. The increase in the J – V slope at 3 V coincides with

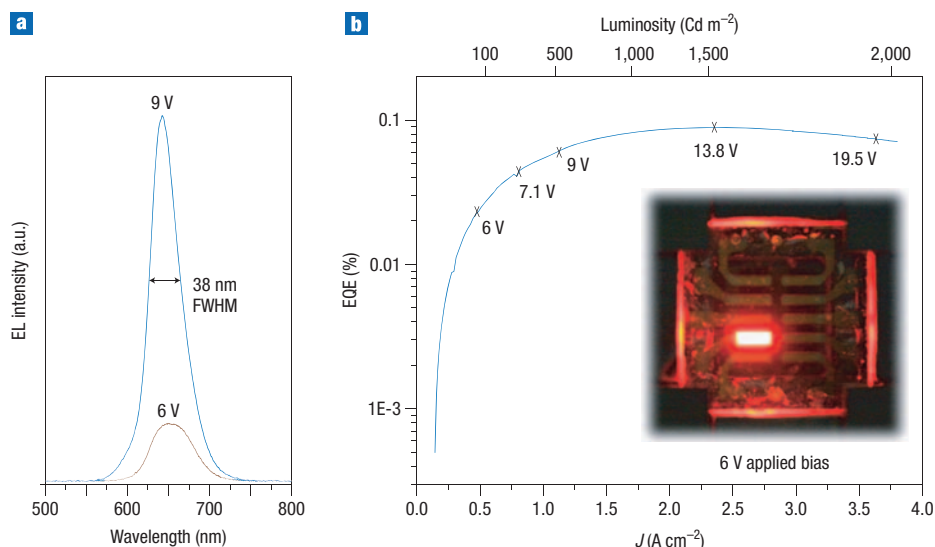


Figure 4 Quantum-dot light-emitting diode EL spectrum and efficiency. **a**, Electroluminescence spectra of the QD-LED of Fig. 1a at 6 V (0.46 A cm⁻²) and 9 V (1.14 A cm⁻²) applied bias. **b**, Plot of the QD-LED EQE measured from the front face of the device as a function of J . A maximum EQE of 0.09% and a luminance of 1,500 Cd m⁻² were reached at 13.8 V, 2.33 A cm⁻². The inset shows a photograph of a bright and uniform pixel at 6 V applied bias. A significant amount of additional light was guided through the glass substrate and emitted at the four substrate edges, as is evident from the photograph. The presence of the edge-emitted light is not reflected in the stated EQE measurements.

the onset of QD-LED EL, which is first observed at 3.8 V, and is therefore associated with the onset of both electron and hole injection into the QDs. The elevated current and J - V slope of 1.3 for applied voltages greater than 10 V is a signature of the combined J - V characteristics for injected electrons and holes, with one or both of the carriers tending to ohmic conduction. These QD-LEDs sustain steady-state current densities of up to 3.5 A cm⁻², which corresponds to a carrier injection rate of 1×10^7 carriers per second per QD and a maximum exciton density per QD of 0.1.

Figure 4a shows a characteristic QD EL peak centred at $\lambda = 642$ nm with a FWHM of 38 nm. The similarity between the EL spectrum and the PL of QDs in solution (FWHM = 40 nm) indicates that the device emission is due entirely to the QDs. Figure 4b shows the EQE of the QD-LED as a function of J , which, at its maximum of 0.09%, is almost two orders of magnitude higher than previous reports of devices with QDs embedded between doped inorganic transport layers⁸. At 6 V, 0.46 A cm⁻², pixel brightness is uniform at 74 Cd m⁻², with emission entirely from the QDs. Standard video brightness (200 Cd m⁻²) occurs in our device at 7.15 V, 0.71 A cm⁻². The peak brightness is measured to be 1,950 Cd m⁻² when J is 3.73 A cm⁻² (19.5 V), and the peak luminescence efficiency is 0.064 Cd A⁻¹ when J is 2.33 A cm⁻² (13.8 V). Comparable brightness and J - V characteristics were observed when the devices were tested after being stored in air for four days, in contrast to unpackaged organic QD-LEDs, which cannot withstand prolonged atmospheric exposure. The EQE of the QD-LED reported here is probably limited by Förster energy transfer between QDs and Auger recombination due to QD charging, which results from electron energy-band alignment of the constituent QD-LED layers. The QD-LED response to sinusoidally modulated drive voltage is plotted in Fig. 5, with the amplitude of the modulation in the light output showing a 3-dB frequency of 1.2 MHz, corresponding to a QD-LED response faster than 1 μ s.

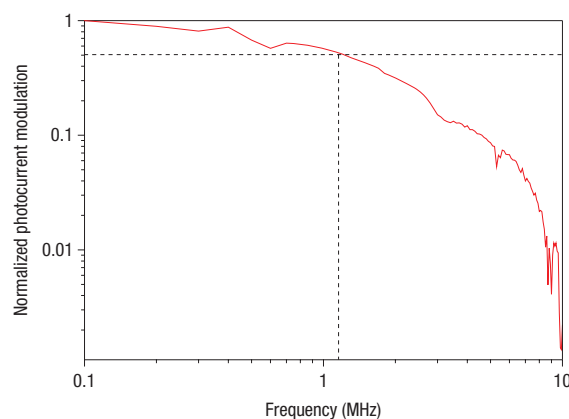


Figure 5 Quantum-dot light-emitting diode RC time-constant measurement. Plot of the modulation in QD-LED EL intensity (noted as the normalized photocurrent in the EL photodetector) operated at $V = V_{dc} + V_m \sin(\omega t)$, with $V_{dc} = 9$ V, $V_m = 5$ V and ω indicated on the abscissa. The half-power point of the curve corresponds to the 3-dB cutoff frequency of 1.2 MHz.

To study the exciton dynamics in our devices and determine whether electrically pumped lasing of QDs in QD-LED structures is feasible, we performed time-resolved PL measurements on the charge transport layers and the QDs. No PL signal was measured from optically excited 50-nm-thick NiO and ZnO:SnO₂ thin films, indicating that non-radiative processes faster than 10 ps dominate exciton relaxation in the metal-oxide transport layers. This implies that the dominant mechanism for generating EL in our QD-LEDs was direct charge injection into the QD layer rather than energy transfer from weakly bound metal-oxide Wannier excitons to excitons in the QDs. To achieve biexciton lasing in colloidal QD films, the exciton generation rate must

compete with non-radiative processes such as the Auger decay^{11,13}. With time-resolved PL we measured a biexciton lifetime of 1.3 ns for the CdZnSe QDs. Therefore, for the onset of the biexciton lasing action an average charge-carrier injection rate of nearly 1×10^9 electrons per second per QD is needed, which is 100 times higher than the maximum steady-state J obtained in this study. To reach the elevated current densities that might lead to lasing action, the QD-LEDs could be run in pulsed mode, as previously demonstrated in experiments with organic LEDs ref. 17. Note that additional optical absorption due to proposed high carrier density in the QD layers¹⁸ might necessitate even larger drive currents, which further emphasizes the need for robust inorganic devices as the first step in the demonstration of electrically pumped colloidal QD lasers.

In conclusion, this work demonstrates that metal oxides and colloidal QDs can be combined to fabricate bright, monochrome LEDs with uniform pixel emission of saturated colour and high peak luminance. The brightness of the devices reported here matches that of the best organic-based QD-LEDs, but with the benefit of improved shelf-life robustness inherent in the environmental stability of metal-oxide charge transport layers. The stable operation under a high carrier-injection rate should enable evolution of the QD-LEDs to device designs that will be needed to demonstrate electrically pumped colloidal QD lasers. Such devices would be able to take full advantage of the tunability and the ease of fabrication and processing of colloidal QDs to provide simple, tunable, coherent light sources.

METHODS

METAL OXIDE AND QUANTUM DOT CHARACTERIZATION

Atomic-force-microscope characterizations of the metal oxide and QD thin films were done with the Digital Instruments Dimension 3000 in the tapping mode. X-ray diffraction measurements were performed with the Rigaku Powder 250 mm diffractometer. Hot-point probe measurements to determine the semiconductor type involved a standard multimeter with one contact heated using a soldering iron.

COLLOIDAL QUANTUM-DOT LIGHT-EMITTING DIODE FABRICATION

To fabricate a colloidal QD-LED, cleaned glass substrates were patterned with a 60-nm-thick ITO anode deposited through a shadow mask using RF magnetron sputtering in an inert argon environment at a pressure of 5 mtorr and a rate of 0.06 Å s^{-1} . The substrate was heated to $\sim 250^\circ\text{C}$ during deposition to increase the ITO conductivity. The slow growth rate prevents surface roughness on the ITO electrode, which can induce roughness in the HTL, leading to electrical shorts through the device structure. The 20-nm-thick, p-type, NiO HTL was sputtered onto the ITO at a deposition rate of 0.2 Å s^{-1} in a 2:100 oxygen to argon atmosphere at a pressured 6 mtorr pressure and using 200 W of RF power.

Building on earlier work^{19,20}, the colloidal QDs were synthesized by injecting triethylphosphine selenide into a pot of ZnO, CdO, oleic acid and 1-octadecene at 310°C . The ZnCdSe QDs were precipitated twice with acetone and redispersed in chloroform. The correct concentration of QD solution to yield three to four layers of QDs on the NiO was approximated using optical absorption measurements and confirmed using an AFM. Quantum dots were spin-deposited onto the NiO in a nitrogen atmosphere.

The ETL was deposited on the QDs by simultaneously sputtering ZnO at 15 W and SnO₂ at 9 W in a pure argon environment at a pressure of 5 mtorr. This corresponds to a combined deposition rate of 0.2 Å s^{-1} , which is sufficiently slow to minimize damage to the QD underlayer. A 40-nm-thick silver cathode was then thermally evaporated through a shadow mask onto the ZnO:SnO₂ at a rate of 1.5 Å s^{-1} .

Each 12 mm \times 12 mm substrate was patterned to yield 10 devices, each with an area of 0.012 cm^2 .

COLLOIDAL QUANTUM-DOT LIGHT-EMITTING DIODE CHARACTERIZATION

Our devices were measured without environmental packaging and in atmospheric conditions. Current–voltage characteristics of the QD-LED were recorded using a computer-controlled Keithley 2612 current/voltage source

meter. To calculate the EQEs, the EL from the front face of the device was detected using a calibrated Newport 2112 silicon photodetector at the same time that the J – V characteristics were measured. Electroluminescence spectra were taken with an Ocean Optics spectrometer with bias applied to the device using the Keithley 2612.

To calculate the exciton density per QD in a hexagonally close-packed film, we used the measured current density and approximated the QD cross-sectional area. We assumed equal hole and electron currents and that all charge carriers flow through the QDs and not the ligands. We used a QD lifetime of 5 ns in a close-packed film, a QD radius of 4 nm, and a ligand length of 1 nm.

For the time-resolved PL measurements, samples were excited with 100-fs-long optical pulses with a wavelength of 400 nm, generated by a Ti:sapphire regenerative laser amplifier with a frequency doubler. The PL was detected with a 10-ps resolution streak camera. The biexciton lifetimes were calculated as described in ref. 18.

The resistance–capacitance (RC) time constant of the device was measured by applying a fixed d.c. bias, V_{dc} , to the device using a Keithley 2612 and a sinusoidal modulated voltage, V_{m} , using an Agilent 33250A waveform generator, such that the total applied voltage was given by $V = V_{\text{dc}} + V_{\text{m}}\sin(\omega t)$. The angular frequency, ω , was varied, and the decrease in the modulation of the EL intensity was detected as described above.

Received 21 August 2007; accepted 17 January 2008;
published 16 March 2008.

References

- Caruge, J.-M., Halpert, J. E., Bulović, V. & Bawendi, M. G. NiO as an inorganic hole-transporting layer in quantum-dot light emitting devices. *Nano Lett.* **6**, 2991–2994 (2006).
- Coe, S., Woo, W. K., Bawendi, M. & Bulović, V. Electroluminescence from single monolayers of nanocrystals in molecular organic devices. *Nature* **420**, 800–803 (2002).
- Coe-Sullivan, S., Steckel, J. S., Woo, W. K., Bawendi, M. G. & Bulović, V. Large-area ordered quantum-dot monolayers via phase separation during spin-casting. *Adv. Funct. Mater.* **15**, 1117–1124 (2005).
- Coe-Sullivan, S., Woo, W. K., Steckel, J. S., Bawendi, M. G. & Bulović, V. Tuning the performance of hybrid organic/inorganic quantum dot light-emitting devices. *Organic Electron.* **4**, 123–130 (2003).
- Schlamp, M., Peng, X. & Alivisatos, A. P. Improved efficiencies in light emitting diodes made with CdSe(CdS) core/shell type nanocrystals and a semiconducting polymer. *J. Appl. Phys.* **82**, 5837–5842 (1997).
- Steckel, J. S. *et al.* Blue luminescence from (CdS)/ZnS core–shell nanocrystals. *Angew. Chem. Int. Edn* **43**, 2154–2158 (2004).
- Zhao, J. *et al.* Efficient CdSe/CdS quantum dot light-emitting diodes using a thermally polymerized hole transport layer. *Nano Lett.* **6**, 463–467 (2006).
- Mueller, A. H. *et al.* Multicolor light-emitting diodes based on semiconductor nanocrystals encapsulated in GaN charge injection layers. *Nano Lett.* **5**, 1039–1044 (2005).
- Colvin, V. L., Schlamp, M. C. & Alivisatos, A. P. Light-emitting diodes made from cadmium selenide nanocrystals and a semiconducting polymer. *Nature* **370**, 354–357 (1994).
- Hikmet, R. A. M., Talapin, D. V. & Weller, H. Study of conduction mechanism and electroluminescence in CdSe/ZnS quantum dot composites. *J. Appl. Phys.* **93**, 3509–3514 (2003).
- Klimov, V. I. *et al.* Optical gain and stimulated emission in nanocrystal quantum dots. *Science* **290**, 314–317 (2000).
- Shimizu, K. T., Woo, W. K., Fisher, B. R., Eisler, H. J. & Bawendi, M. G. Surface-enhanced emission from single semiconductor nanocrystals. *Phys. Rev. Lett.* **89**, 117401 (2002).
- Klimov, V. I., Mikhailovsky, A. A., McBranch, D. W. & Bawendi, M. G. Quantization of multiparticle Auger rates in semiconductor quantum dots. *Science* **287**, 1011–1013 (2000).
- Malliaras, G. G. & Scott, J. C. The roles of injection and mobility in organic light emitting diodes. *J. Appl. Phys.* **83**, 5399–5403 (1998).
- Yamada, S., Yoshioka, T., Miyashita, M., Urabe, K. & Kitao, M. Electrochromic properties of sputtered nickel oxide. *J. Appl. Phys.* **63**, 2116–2119 (1987).
- Yoshimura, K., Miki, T. & Tanemura, S. Nickel oxide electrochromic thin films prepared by reactive dc magnetron sputtering. *Jpn J. Appl. Phys.* **34**, 2440–2446 (1995).
- Kozlov, V. G. *et al.* Structures for organic diode lasers and optical properties of organic semiconductors under intense optical and electrical excitations. *IEEE J. Quant. Electron.* **36**, 18–26 (2000).
- Fisher, B. R., Caruge, J.-M., Chan, Y. T., Halpert, J. E. & Bawendi, M. G. Multiexciton fluorescence from semiconductor nanocrystals. *Chem. Phys.* **318**, 71–81 (2005).
- Zhong, X., Feng, Y., Knoll, W. & Han, M. Alloyed Zn_{1-x}Cd_xS nanocrystals with highly narrow luminescence spectral width. *J. Am. Chem. Soc.* **125**, 13559–13563 (2003).
- Zhong, X., Han, M., Dong, Z., White, T. J. & Knoll, W. Composition-tunable Zn_{1-x}Cd_x-Se nanocrystals with high luminescence and stability. *J. Am. Chem. Soc.* **125**, 8589–8594 (2003).

Acknowledgements

The authors would like to thank G. Nair and G. Chen for their technical assistance and P. Mardilovich for insightful discussions. This work was supported in part by the National Science Foundation Materials Research Science and Engineering Center at (NSF-MRSEC) the Massachusetts Institute of Technology (MIT) Program (DMR-0213282), making use of its Shared Experimental Facilities, the Harrison Spectroscopy Laboratory (NSF-CHE-011370), the U.S. Army through the Institute for Soldier Nanotechnologies (DAAI-19-02-0002), National Science Foundation Nanoscale Interdisciplinary Research Team (NSF NIRT) (CHE-0507147), and a Presidential Early Career Award for Scientists and Engineers (PECASE).

Correspondence and requests for materials should be addressed to V.B.

Reprints and permission information is available online at <http://npg.nature.com/reprintsandpermissions/>

Contact Printing of Quantum Dot Light-Emitting Devices

LeeAnn Kim,[†] Polina O. Anikeeva,[†] Seth A. Coe-Sullivan,[‡] Jonathan S. Steckel,[‡] Mounji G. Bawendi,^{*,§} and Vladimir Bulović^{*,†}

Laboratory of Organic Optics and Electronics, Department of Electrical Engineering and Computer Science, Massachusetts Institute of Technology, Cambridge Massachusetts 02139, and Department of Chemistry, Massachusetts Institute of Technology, Cambridge, Massachusetts 02139

Received August 18, 2008; Revised Manuscript Received October 3, 2008

ABSTRACT

We demonstrate a solvent-free contact printing process for deposition of patterned and unpatterned colloidal quantum dot (QD) thin films as the electroluminescent layers within hybrid organic-QD light-emitting devices (QD-LEDs). Our method benefits from the simplicity, low cost, and high throughput of solution-processing methods, while eliminating exposure of device structures to solvents. Because the charge transport layers in hybrid organic/inorganic QD-LEDs consist of solvent-sensitive organic thin films, the ability to avoid solvent exposure during device growth, as presented in this study, provides a new flexibility in choosing organic materials for improved device performance. In addition, our method allows us to fabricate both monochrome and red–green–blue patterned electroluminescent structures with 25 μm critical dimension, corresponding to 1000 ppi (pixels-per-inch) print resolution.

Exceptional luminescent properties of colloidal QDs¹ such as the narrow emission spectra tunable throughout the entire visible spectrum (corresponding to highly saturated emission colors) and the high photoluminescence efficiencies suggest the use of QD films in electroluminescent devices and pixilated full-color displays. The pioneering demonstrations of QD applications in light-emitting devices (LEDs) utilized conjugated polymer–QD blends as emissive layers and exhibited low efficiencies as compared to polymer LEDs.^{2,3} The subsequent significant increase in the external quantum efficiency (EQE) (reaching EQE of 0.5% to 2%^{4–6}) of hybrid organic/inorganic QD-LEDs was demonstrated in structures that used a single monolayer of QDs⁴ surrounded by organic transport layers. The use of QD monolayers minimized the negative impact of QD charging and resistive power losses associated with poor QD-to-QD charge transport^{8,9} characteristic of the earlier devices that utilized QD multilayers.¹⁰ These technical advances highlighted the need for development of a reproducible method of formation of close-packed QD monolayers, with a preference of generating laterally patterned QD films, as would be needed in full-color pixilated structures.

Large area (several cm^2) QD monolayers can be assembled out of solution, either by Langmuir–Blodgett^{11,12} or by spin-

casting (phase segregation)⁵ techniques. The critical limitation of the Langmuir–Blodgett assembly technique is in its low throughput and cumbersome implementation that appears incompatible with industrial-scale production. The spin-casting assembly technique has two critical limitations: (1) it cannot be applied to patterning of QD monolayers, and (2) it places solvent compatibility requirements on the device fabrication process. Consequently, adaption of the technique to the fabrication of active electronic devices, such as QD-LEDs requires the devices to be designed around the deposition technique that demands solvent compatibility and can lead to nonideal device structures of inferior performance. The lack of simple methods for in-plane patterning of pixilated QD-LEDs has largely been ignored in published literature¹³ and is the topic of the present work. In this Letter we demonstrate that contact printing^{12,14} can be used to deposit patterned, solvent-free QD monolayers. We demonstrate the flexibility of the approach and its functional use by inserting patterned and unpatterned QD monolayers into active QD-LED structures.

The QD printing process follows the steps schematically shown in Figure 1: (1) poly(dimethylsiloxane) (PDMS) is molded using a silicon master; (2) resulting PDMS stamp is conformally coated with a thin film of parylene-C, a chemical-vapor deposited (CVD) aromatic organic polymer (chemical structure is shown in the inset of Figure 2); (3) parylene-C coated stamp is inked via spin-casting of a solution of colloidal QDs suspended in an organic solvent;

* Corresponding authors.

[†] Laboratory of Organic Optics and Electronics, Department of Electrical Engineering and Computer Science.

[‡] Present address: QD Vision Inc., Watertown, MA 02472.

[§] Department of Chemistry.

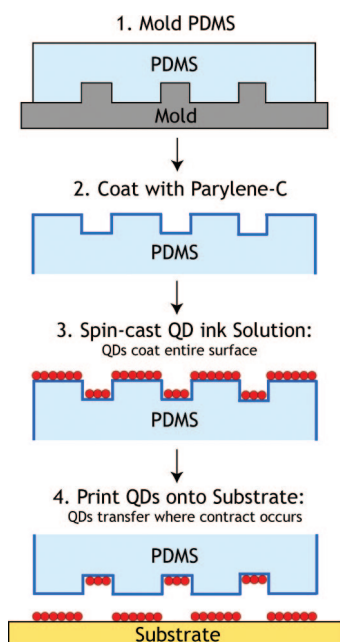


Figure 1. Schematic shows the four-step contact printing process.

(4) after the solvent evaporates, the formed QD monolayer is transferred onto the substrate (e.g., on top of the first few layers of a multilayer device) by contact printing.

Chemical compatibility between the organic solvents used in QD processing and the elastomer stamp critically influences the QD film morphology and, consequently, QD-LED performance. Previously, it has been shown that QDs can form continuous close-packed monolayers upon spin-casting and phase separation from chloroform or chlorobenzene solutions.⁵ These solvents are compatible with a variety of hydrophobic organic ligands used for QD surface passivation during organometallic synthesis. However, a plain PDMS surface is chemically incompatible with chloroform solutions of QDs, which is manifested in nonuniform QD films, caused by chloroform dewetting from PDMS during spin-casting. Figure 2a shows the atomic force microscope (AFM) image of a QD film printed onto *N,N'*-

bis(3-methylphenyl)-*N,N'*-bis(phenyl)benzidine (TPD) underlayer using a plain PDMS stamp. The film is discontinuous and exhibits morphology characteristic of spinodal dewetting. The peak-to-peak roughness of QD films in this case is >160 nm and rms is >20 nm, too rough for QD-LED fabrication. The characteristic organic charge transporting layers that are on the order of 50 nm in thickness are likely to be electrically shorted by the rough QD layers, yielding inoperable devices.

We find that coating the elastomer stamp with parylene-C results in a chemical surface, which is compatible with spreading of colloidal QDs solvated in chloroform. The contact angle measurements show that chloroform wets the parylene-C surface more efficiently than plain PDMS as indicated by the decrease in the contact angle from $28^\circ \pm 1^\circ$ for chloroform on plain PDMS to $6^\circ \pm 1^\circ$ for chloroform on parylene-C-coated PDMS. Chloroform evaporates during the spin-casting of chloroform-solvated QDs on parylene-C-coated PDMS, leaving a monolayer of QDs in contact with the parylene-C surface.

Parylene-C is an aromatic polymer; therefore, its surface is suboptimal for minimizing the surface energy of the QD monolayer, since QDs are generally capped with aliphatic organic ligands (such as trioctylphosphine and oleic acid). The aromatic parylene-C is therefore a good release layer for the aliphatic-capped QDs and facilitates their transfer from the PDMS stamp onto the substrate during the printing process. If instead of parylene-C we employed an aliphatic surfactant on the PDMS stamp, we expect that ensuing strong interaction between QDs and a stamp surface would impede QD release.

AFM image in Figure 2b shows a close-packed monolayer of QDs printed onto TPD film using a parylene-C-coated PDMS stamp. Peak-to-peak roughness of ~ 5 nm indicates a controlled deposition of a single QD layer. Low rms ≈ 0.5 nm enables these films to be used in thin (<100 nm thick) hybrid optoelectronic devices. The height distribution analysis of AFM images allows us to determine the number of QD layers deposited via contact printing, which we then use to precisely tune the concentration of QD solution needed

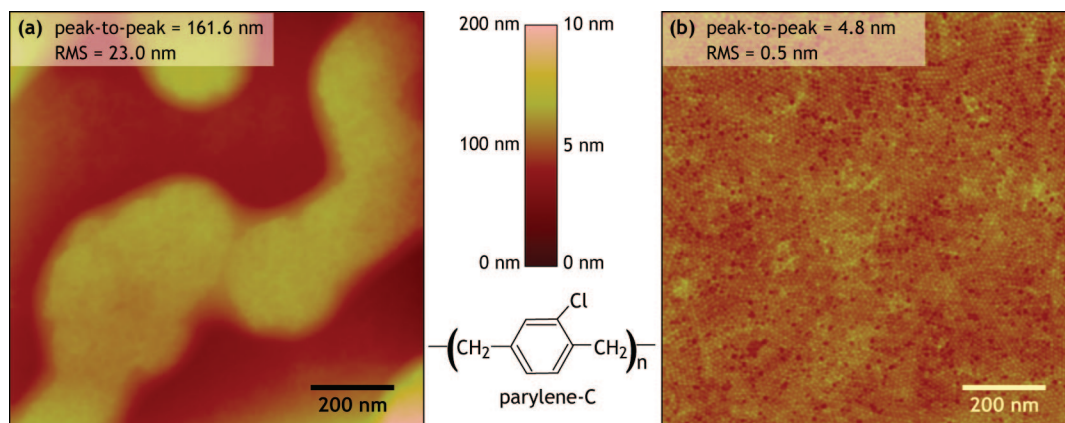


Figure 2. AFM images show QD films deposited on top of the TPD layer using (a) a plain PDMS stamp and (b) a parylene-C-coated PDMS stamp. QD films on plain PDMS exhibit spinodal decomposition pattern with high surface roughness (rms = 23.0 nm), while on parylene-C-coated PDMS QDs form smooth hexagonally close-packed monolayers (rms = 0.5 nm). The chemical formula of parylene-C is shown in the inset.

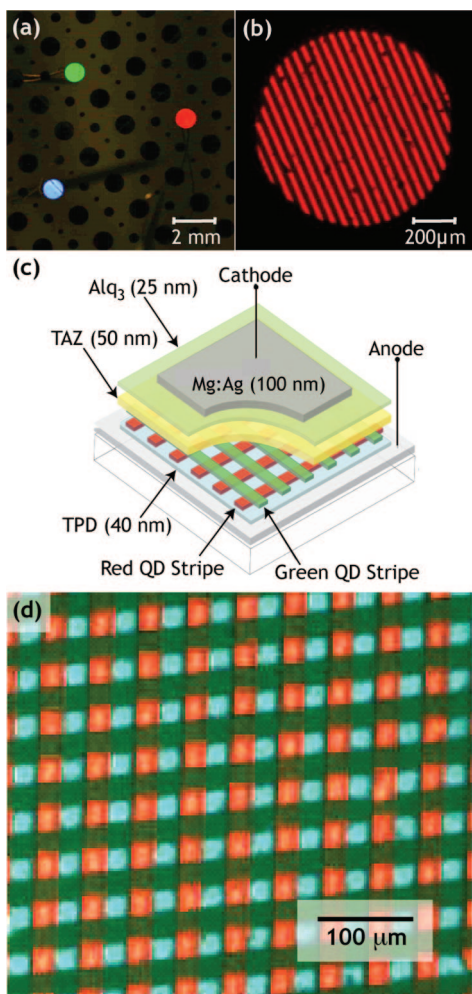


Figure 3. (a) Electroluminescent red and green QD-LED pixels are fabricated on the same substrate. A blue pixel is the result of TPD emission in the area where QDs were not deposited. (b) Electroluminescent QD-LED pixel is patterned with $25\ \mu\text{m}$ wide stamp features. (Bias voltage is 5 V.) (c) Schematic diagram shows the structure of a QD-LED with an emissive layer consisting of $25\ \mu\text{m}$ wide stripes of green and red QD monolayers. (d) Electroluminescence (EL) of the structure shown in (c) at 7 V of applied bias. Blue emission is due to TPD hole-transporting underlayer. The background TPD emission is not present in the image (b) due to lower applied bias. Corresponding EL spectra can be found in the Supporting Information.

to achieve smooth close-packed QD monolayers (see Supporting Information).

Figure 3a shows the application of the contact printing to fabrication of multiple QD-LED colors on the same substrate. QD-LED structure consists of a transparent indium tin oxide (ITO) anode coated with a hole injecting polymer poly(3,4-ethylenedioxythiophene):poly(styrenesulfonate) PEDOT:PSS, followed by 40 nm thick TPD hole transporting layer (HTL), printed QD monolayer, 15 nm thick 3,4,5-triphenyl-1,2,4-triazole (TAZ) hole blocking layer, 25 nm thick tris(8-hydroxyquinoline) (Alq_3) electron transporting layer (ETL), and 100 nm thick Ag/Mg cathode with a 20 nm thick Ag protective overlayer. The red (CdSe/ZnS core-shell¹⁵) and green (ZnSe/CdSe/ZnS core-double-shell^{16,17}) QDs are separately printed onto blanket TPD film, and the structure is completed by blanket deposition of the remaining charge

transport layers. The red and green pixels exhibit electroluminescence (EL) solely due to QD emission, while a blue pixel is the result of TPD EL in the absence of QDs.

In panels b and d of Figure 3, we demonstrate patterning of close-packed, monochrome (b) and multicolor QD-LED pixels (d) as small as $25\ \mu\text{m}$ (1000 dpi). We use elastomer stamps with a relief pattern to deposit the $25\ \mu\text{m}$ wide intersecting stripes of red and green QD monolayers in a QD-LED structure shown in Figure 3c. EL of red and green QDs and blue TPD is simultaneously observed when the QD-LED is biased at 7 V. This demonstration presents the first use of contact printing of QDs in the fabrication of patterned EL devices, a critical step toward the realization of pixilated, full color, high-resolution QD-LED displays.

The solvent-free deposition of the QD monolayers is compatible with a wide variety of organic semiconductors that are not compatible with solution processing methods. Figure 4a shows red (CdSe/ZnS core-shell¹⁵), green (ZnSe/CdSe/ZnS core-double shell^{16,17}), and blue (CdS/ZnS core-shell¹⁸) QD-LED pixels fabricated in the identical device structure shown in Figure 4b, in which wide band gap organic semiconductor, 4,4'-*N,N'*-dicarbazole-biphenyl (CBP), replaced TPD as a hole transport material. The wide band gap of CBP contributes to more efficient charge and exciton confinement, and an improvement in color saturation of the QD-LEDs, yielding CIE coordinates (0.66, 0.34), (0.21, 0.70), (0.18, 0.13) for the red, green, and blue QD-LEDs, respectively (shown in Figure 4d), with corresponding EQEs of 1.0%, 0.5%, and 0.2% at video brightness ($\sim 100\ \text{cd/m}^2$). The normalized EL spectra are shown in Figure 4e, with the spectra of green and red QD-LEDs solely due to the QD emission and blue QD-LED EL spectrum showing a minor contribution from organic thin film EL. EQE and current-voltage characteristics for QD-LEDs in Figure 4 are available in the Supporting Information.

Contact printing can also be used to create mixed-color and white QD-LEDs,^{6,7} since this method is compatible with a variety of colloidal QDs synthesized via different procedures and passivated by different organic ligands. Using the printing method, in recent publications we demonstrated record EQE of 2.3% for red,¹⁹ 0.65% for green,^{6,7} and 0.35% for blue^{6,7} printed QD-LEDs. In contrast to previously reported high-efficiency QD-LEDs that use spin-casting to deposit multiple QD layers to achieve saturated QD-LED emission,^{20–22} our method allows us to minimize the use of QDs (reducing the cost of fabrication and operating device voltage) while maintaining QD-LED EL color purity. The demonstrated large color gamut from QD-LEDs exceeds the performance of both LCD and organic LED (OLED) technologies, suggesting future use of QD-LEDs in high definition, accurate color flat panel displays and in general lighting sources.⁶

The present work demonstrated a contact printing method for depositing patterned QD monolayer films that are formed by spin-casting QDs onto chemically functionalized PDMS stamps. The method enables insertion of QD monolayers into arbitrary thin film device structures without exposing the constituent thin films to solvents or resorting to phase

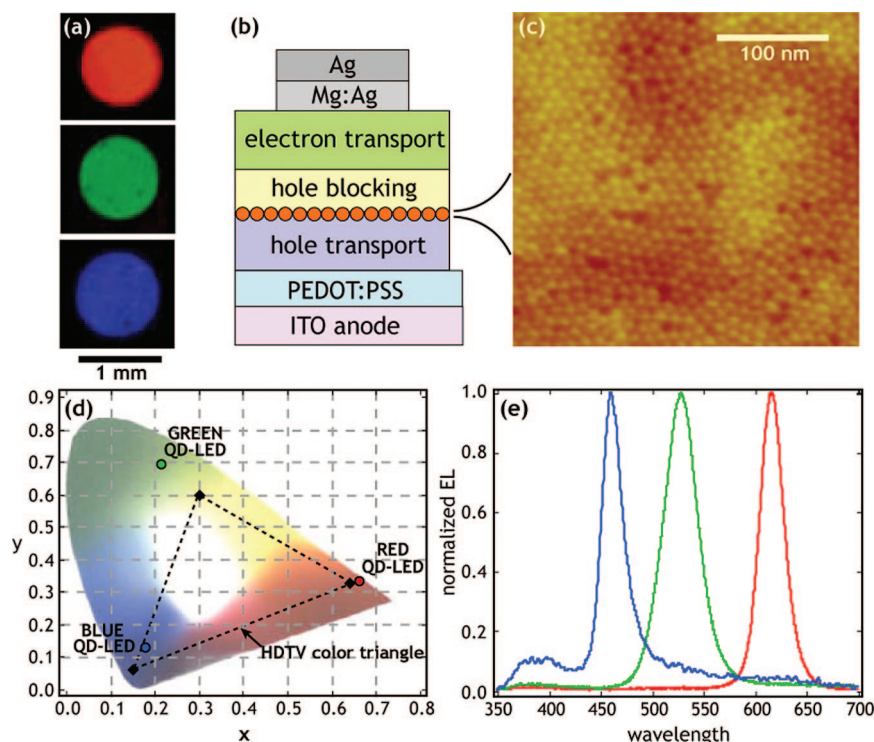


Figure 4. (a) Electroluminescent red, green, and blue QD-LED pixels with the device structure shown in (b). (b) Schematic diagram shows the cross section of an archetypical QD-LED. (c) A high-resolution AFM micrograph shows a close-packed monolayer of QDs deposited on top of the CBP hole transporting layer prior to deposition of hole blocking and electron transporting layers. Here unpatterned elastomer stamps are used to produce continuous QD monolayers. (d) Chromaticity diagram shows the positions of red, green, and blue QD-LED colors, an HDTV color triangle is shown for comparison. (e) Normalized EL spectra of fabricated QD-LEDs corresponding to the CIE coordinates in (d). QD-LED images and EL spectra are taken at video brightness (100 cd/m^2), which corresponds to the applied current density of 10 mA/cm^2 for red QD-LEDs, 20 mA/cm^2 for green QD-LEDs, and 100 mA/cm^2 for blue QD-LEDs.

separation methods to form QD layers. Inherent to this printing method is the ability to form patterned QD monolayer features, which in this work we used to demonstrate multicolor QD-LED structures with electroluminescent area resolution of $25 \mu\text{m}$. (See the Supporting Information for the demonstration of additional QD film features as small as 150 nm .) The demonstrated printing technique now enables formation of arbitrarily complex multilayer structures containing QDs, which can elucidate the physical operating mechanisms that govern operation of QD optoelectronics and lead to design of QD-containing structures of superior performance.¹⁹

Materials and Methods. We prepare PDMS elastomer stamps by mixing PDMS base with a curing agent (Dow Corning Sylgard 184 silicone elastomer) at the ratio of 10:2. The mixture is then poured into a Petri dish that may contain silicon masters with relief patterns if patterned films are desired. The dish is then placed under low vacuum at room temperature to eliminate air pockets generated by the mixing process. After air pockets have collapsed, the mixture is brought to atmospheric pressure and cured at room temperature for ~ 7 to 10 days. The curing process can be accelerated by baking the mixture at 60°C for $\sim 5 \text{ h}$. The cured PDMS block is then released from the Petri dish and silicon masters and cut into $\sim 1 \text{ cm}^3$ cubes.

We use CVD to deposit between 150 and 200 nm thick layers of parylene-C onto PDMS stamps; the CVD precursor (dimer, $n = 2$ in the chemical structure shown in the inset

of Figure 2) is purchased from PARA TECH Coating, Inc.

Colloidal QDs are synthesized and purified according to the procedures reported in ref 15 (for red CdSe/ZnS core shell QDs), ref 17 (for green ZnSe/CdSe/ZnS core–double shell QDs), and ref 18 (for blue CdS/ZnS core–shell QDs).

During QD-LED fabrication PEDOT:PSS (H.C. Starck, Inc.) is deposited via spin-casting onto ITO-coated glass (Thin Film Devices, Inc.) The organic charge transport layers (TPD, CBP, TAZ and Alq₃ purchased from H. W. Sands Corp.) and Ag/Mg cathode are deposited by physical vapor deposition at pressures $< 10^{-6}$ Torr and evaporation rates $< 0.2 \text{ nm/s}$.

Acknowledgment. This research was funded in part by the NSF-MRSEC program, PECASE grant, MIT Institute for Soldier Nanotechnologies, and DMR. This work made use of MIT MRSEC Shared Facilities supported by the National Science Foundation. Authors would like to thank Alexi Arango, Ioannis Kymissis, Preston Snee, and Vanessa Wood for their technical assistance.

Supporting Information Available: Description of patterning QD films by molding, calibrating QD solutions by AFM, plots of the electroluminescence spectra of patterned QD-LEDs of Figure 3d, and electronic characteristics of QD-LEDs employing CBP as a hole-transporting layer. This material is available free of charge via the Internet at <http://pubs.acs.org>.

References

- (1) Murray, C. B.; Norris, D. J.; Bawendi, M. G. *J. Am. Chem. Soc.* **1993**, *115*, 8706–8715.
- (2) Colvin, V. L.; Schlamp, M. C.; Alivisatos, A. P. *Nature* **1994**, *370*, 354–357.
- (3) Dabbousi, B. O.; Bawendi, M. G.; Onitsuka, O.; Rubner, M. F. *Appl. Phys. Lett.* **1995**, *66* (11), 1316–1318.
- (4) Coe, S.; Woo, W.-K.; Bawendi, M. G.; Bulović, V. *Nature* **2002**, *420*, 800–803.
- (5) Coe-Sullivan, S.; Steckel, J. S.; Woo, W.-K.; Bawendi, M. G.; Bulović, V. *Adv. Funct. Mater.* **2005**, *15*, 1117–1124.
- (6) Anikeeva, P. O.; Halpert, J. H.; Bawendi, M. G.; Bulović, V. *Nano Lett.* **2007**, *7*, 2196–2200.
- (7) As a part of the development process of our contact printing technique, we employed this procedure in fabrication of QD-LEDs reported in ref 6. Although, not explicitly stated in ref 6 all QD-LEDs described in that letter contain printed QD monolayers.
- (8) Leatherdale, C. A.; Kagan, C. R.; Morgan, N. Y.; Empedocles, S. A.; Kastner, M. A.; Bawendi, M. G. *Phys. Rev. B* **2000**, *62*, 2669–2680.
- (9) Ginger, D. S.; Greenham, N. C. *J. Appl. Phys.* **2000**, *87*, 1361–1368.
- (10) Schlamp, M. C.; Peng, X.; Alivisatos, A. P. *J. Appl. Phys.* **1997**, *82*, 5837–5842.
- (11) Dabbousi, B. O.; Murray, C. B.; Rubner, M. F.; Bawendi, M. G. *Chem. Mater.* **1994**, *6*, 216–219.
- (12) Santhanam, V.; Andres, R. P. *Nano Lett.* **2004**, *4*, 41–44.
- (13) Coe-Sullivan, S.; Steckel, J. S.; Kim, L.; Bawendi, M. G.; Bulović, V. *Proc. SPIE* **2005**, *5739*, 108–115.
- (14) Kumar, A.; Whitesides, G. M. *Appl. Phys. Lett.* **1993**, *63*, 2002–2004.
- (15) Dabbousi, B. O.; Rodriguez-Viejo, J.; Mikulec, F. V.; Heine, J. R.; Mattoussi, H.; Ober, R.; Jensen, K. F.; Bawendi, M. G. *J. Phys. Chem. A* **1997**, *101*, 9463–9475.
- (16) Ivanov, S. A.; Nanda, J.; Piryatinski, A.; Achermann, M.; Balet, L. P.; Bezel, I. V.; Anikeeva, P. O.; Tretiak, S.; Klimov, V. I. *J. Phys. Chem. B* **2004**, *108*, 10625–10630.
- (17) Steckel, J. S.; Snee, P.; Coe-Sullivan, S.; Zimmer, J. P.; Halpert, J. E.; Anikeeva, P.; Kim, L.; Bulović, V.; Bawendi, M. G. *Angew. Chem., Int. Ed.* **2006**, *45* (35), 5796–5799.
- (18) Steckel, J. S.; Zimmer, J. P.; Coe-Sullivan, S.; Stott, N. E.; Bulović, V.; Bawendi, M. G. *Angew. Chem., Int. Ed.* **2004**, *43*, 2154–2158.
- (19) Anikeeva, P. O.; Madigan, C. F.; Halpert, J. E.; Bawendi, M. G.; Bulović, V. *Phys. Rev. B* **2008**, *78*, 085434.
- (20) Zhao, J.; Bardecker, J. A.; Munro, A.; Liu, M. S.; Niu, Y.; Ding, I. K.; Luo, J.; Chen, B.; Jen, A. K.-Y.; Ginger, D. S. *Nano Lett.* **2006**, *6*, 463–467.
- (21) Niu, Y.-H.; Munro, A. M.; Cheng, Y.-J.; Tian, Y.; Liu, M. S.; Zhao, J.; Bardecker, J. A.; Jen-La Plante, I.; Ginger, D. S.; Jen, A. K.-Y. *Adv. Mater.* **2007**, *19*, 3371–3376.
- (22) Sun, Q.; Wang, Y. A.; Li, L. S.; Wang, D.; Zhu, T.; Xu, J.; Yang, C.; Li, Y. *Nat. Photonics* **2007**, *1*, 717–722.

NL8025218

Inkjet-Printed Quantum Dot–Polymer Composites for Full-Color AC-Driven Displays

By Vanessa Wood, Matthew J. Panzer, Jianglong Chen, Michael S. Bradley, Jonathan E. Halpert, Mounqi G. Bawendi, and Vladimir Bulović*

We demonstrate print-deposition of high resolution, patterned, multicolored thin films of luminescent colloidal quantum dot (QD)-polymer composites and use the printed patterns in fabricating robust, bright, full-color AC-driven displays. The benefits of AC electroluminescent (EL) displays include simple, low-cost fabrication and high reliability; however, finding efficient and stable phosphors for full-colored displays remains a major challenge.^[1] Today, red-, green-, and blue-light-emitting (RGB) phosphors for AC-EL comprise different material systems and can have luminous efficiencies that span an order of magnitude, rendering manufacture of a multicolor display with balanced RGB components difficult.^[1–3] While there has been substantial research on stacked and patterned devices, one of the most feasible strategies for realizing RGB AC-EL displays is color filtering of white, ZnS-based phosphors.^[1,2] Filtering, however, wastes up to 90% of the output optical power to achieve color saturation, which requires that the display be operated at ten times video brightness in order to meet the RGB color standard.^[4] This results in greater power consumption, faster pixel degradation, and shorter display lifetimes.^[1]

To achieve full-color AC-EL displays, in this study we use colloiddally synthesized QDs to print patterns of robust, solution-processable, luminescent light-converting thin films for AC-EL displays. QDs offer narrow-band luminescence that can be tuned across the visible spectrum by varying their size and chemical composition.^[5] This property motivated the use of QD luminescent centers in thin-film light-emitting diode (LED) structures, in which QDs were electrically excited to demonstrate low-power, color-saturated devices, with side-by-side patterning of RGB pixels enabled by microcontact printing of the QD layers.^[6] In alternate device designs, QDs can also be optically excited, where, for example, the small Stokes shift of red- and green-light-emitting QDs enables their optical excitation by blue light. This property of QDs led to the demonstration of optical

down-conversion using blue GaN LEDs to excite QDs in poly(arylmethacrylate) (PLMA), and the generation of point sources of saturated-color light.^[7] In the present work, we demonstrate a planar, full-color AC-EL display that comprises luminescent thin films of QDs that absorb blue electroluminescence from a commercial phosphor powder and then emit photons at a longer wavelength characteristic of the QD band gap. Emission and absorption spectra for the QDs and EL phosphors

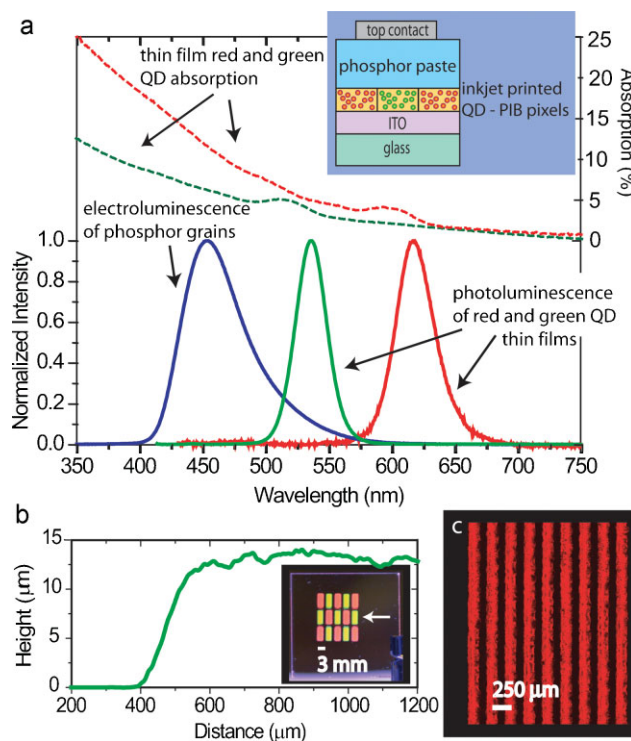


Figure 1. a) Absorption and photoluminescence spectra of spin-coated thin films of red and green QDs and the electroluminescence spectrum of the blue-phosphor paste powered by 50 kHz AC excitation demonstrate the spectral overlaps needed to achieve optical down-conversion of phosphor emission to QD-film luminescence. The inset schematic depicts the cross-section of an AC powder EL device structure with QD-PIB pixels. b) 1 mm profilometry scan of the edge of a green rectangular pixel measuring 3 mm × 5 mm demonstrates the edge definition and top-surface uniformity of an average pixel. The inset is a photograph of a multicolor QD-PIB pattern inkjet printed on 1 inch × 1 inch ITO-coated glass and illuminated with $\lambda = 365$ nm light. c) Luminescence microscopy photograph of a series of parallel lines printed to be 100 μm wide at 250 μm pitch demonstrates the feasibility of printing high-resolution patterns.

[*] Prof. V. Bulović, V. Wood, Dr. M. J. Panzer, Dr. J. Chen, M. S. Bradley
Department of Electrical Engineering and Computer Science
Massachusetts Institute of Technology
77 Massachusetts Avenue
Cambridge, MA 02139 (USA)
E-mail: bulovic@mit.edu

Dr. J. E. Halpert, Prof. M. G. Bawendi
Department of Chemistry
Massachusetts Institute of Technology
77 Massachusetts Avenue
Cambridge, MA 02139 (USA)

DOI: 10.1002/adma.200803256

used in our work are shown in Figure 1a. In contrast to the earlier work by Taylor et al., which uses a white phosphor and poly[2-methoxy-5-(2'-ethyl-hexyloxy)-1,4-phenylene vinylene] (MEH-PPV) to absorb phosphor luminescence, forming MEH-PPV excitons that are then energy-transferred to QDs,^[8] our devices operate based entirely on long-range radiative energy transfer, with no short-range Förster energy transfer expected. Consequently, as shown in Figure 1a, we are not limited to red QDs, but can optically excite any QD that has a first absorption peak at a wavelength longer than $\lambda = 450$ nm.

To deposit thin films of colloiddally synthesized QDs in an AC-EL device, we inkjet-print QD solutions. Inkjet printing is an attractive deposition technique for any large-area electronics application because it minimizes material use and allows for multiple depositions of high-resolution patterned layers of materials. Our experiments show that it is possible to directly inkjet print QDs dispersed in a solvent, but that the structural and luminescent properties of the QD layer are improved if the QDs are embedded in an optically transparent polymer matrix.^[9] In this paper, we use inkjet printing to deposit well-defined, uniform thin films of QDs suspended in a polyisobutylene (PIB) matrix that exhibit enhanced photoluminescence (PL) efficiency over thin films of QDs. The selection of polyisobutylene (PIB) dissolved in hexane and octane as a base for the QD ink is discussed in the Experimental section and in the Supporting Information. Over a period of several months, we observed no aggregation of QDs in the QD-PIB ink stored in a sealed glass vial, and no degradation or phase separation in printed QD-PIB thin films kept in ambient conditions, indicating a high degree of compatibility between QDs and PIB.

One challenge in inkjet printing a uniform thin film is avoiding the "coffee ring" phenomenon, whereby solutes migrate to the edge of a printed drop during the drying process, forming a thin film of uneven thickness.^[10] Previous studies have shown that two-solvent techniques can be used to achieve greater uniformity of inkjet printed films and to facilitate deposition of QDs.^[11] We tune the hexane to octane ratio in the QD-PIB ink solution to reduce nonuniform drying patterns and enable thin films with QDs evenly suspended in a PIB matrix (Supporting Information). A profilometry scan 1 mm long from the indium tin oxide (ITO) to the top surface of a 3 mm \times 5 mm QD-PIB feature (Fig. 1b) demonstrates the edge definition and top-surface uniformity achievable using large droplet sizes and high-speed printing. This feature is comprised of 15 layers of QD-PIB composite printed with 280 pL droplets at a 50 μ m pitch. Figure 1c, which presents a fluorescence microscopy image of a series of parallel lines printed using 120 pL droplets at a pitch of 250 μ m, indicates the feasibility of high-resolution patterns. Here, the QD-PIB ratio is tuned to result in lines 100 μ m wide, where each line is composed of 14 layers of the printed composite to produce printed features 2 μ m thick. The lack of drift in the printed pattern over the 14 layers and the absence of "coffee ring" features highlight the level of accuracy, uniformity, and repeatability afforded in printing with a QD-polymer composite.

As previous research has shown, embedding QDs in an insulating polymer matrix decreases the amount of QD-luminescence quenching observed in closed-packed QD structures.^[7,12] We measure, on average, a factor of 2.5 increase in

the PL efficiency for QDs in the PIB matrix as compared to a spin coated, neat thin film of QDs. For both red and green nanoparticles, we inkjet print 10 mm \times 14 mm rectangles of QD-PIB composite and spin-coat solutions of the same nanoparticles on quartz substrates. We measure the PL for each QD-PIB and QD-only sample excited with a $\lambda = 408$ nm laser, and adjust for the absorption of the sample at $\lambda = 408$ nm. The PL measurement is performed in 10 different locations across each sample, to account for any nonuniformities across the spin-coated and inkjet printed features. The PL efficiency measurements of the nanoparticle films with and without a PIB binder are described further in the Experimental section.

The basic thin-film AC-EL device structure is shown schematically in the inset of Figure 1a. A detailed description of the device fabrication is provided in the Experimental section, but a brief description is given here. Ink solutions of PIB and QDs in a mixture of hexane and octane are deposited using a Hewlett-Packard thermal inkjet picofluidic dispensing system (TIPS) onto conductive, transparent ITO-coated glass or flexible polyethylene terephthalate (PET). Inkjet printing was demonstrated with a series of PIB-stabilized inks that were formulated for optimized viscosity by mixing PIB with core/shell CdSe/ZnS QDs from QD Vision Inc. and Evident Technologies, as well as with in-house-synthesized QDs and nanorods. The inkjet-printed films of QD-PIB composite were covered with a thin film of ZnS:Cu powder in an electrically insulating, transparent binder from Osram-Sylvania, which is doctor-blade deposited and dried at 50 °C. A conductive adhesive tape serves as the top electrode and defines the working device area.

All fabrication and testing was done in ambient conditions and without device packaging. We observed long device shelf lives with no degradation or decrease in brightness during intermittent device testing over one year. The spectra and photographs in Figure 2 show both the blue electroluminescence of the ZnS:Cu phosphors and the green and red QD spectra of optically down-converted QD emission, which is visible when an AC power is applied across the device structures. Because our printing technique results in PIB/QD films of uniform thickness, we were able to demonstrate spectral purity in the optically down-converted QD light with minimal contribution from the blue-phosphor EL emission. When plotted on a Commission International d'Eclairage (CIE) chromaticity diagram (Fig. 2c), the CIE coordinates of our devices define a color triangle that is comparable to the International Telecommunication Union high-definition television (HDTV) standard. Previous work has shown that a solution of mixed QDs can be used to obtain colors inside the space defined by CIE coordinates of the individual QD luminescence.^[11,13] Now, we demonstrate that by varying the thickness of the printed QD-PIB layer, a single QD-ink solution can be used to achieve the set of colors on the trajectory between the CIE coordinates of the blue phosphor and the CIE coordinates of the particular QD lumophore. For a given printed QD-PIB thickness, we observe little change in the CIE coordinates over the entire range of applied voltages (50–430 V_{rms}). While the data in Figure 2 highlights the color uniformity of large (8 mm \times 10 mm) rectangular pixels, it is also possible to fabricate working AC-EL devices with high-resolution features, such as the lines in Figure 1c. Figure 3a is a photoluminescence photograph of a complete device structure on a flexible ITO-coated PET substrate

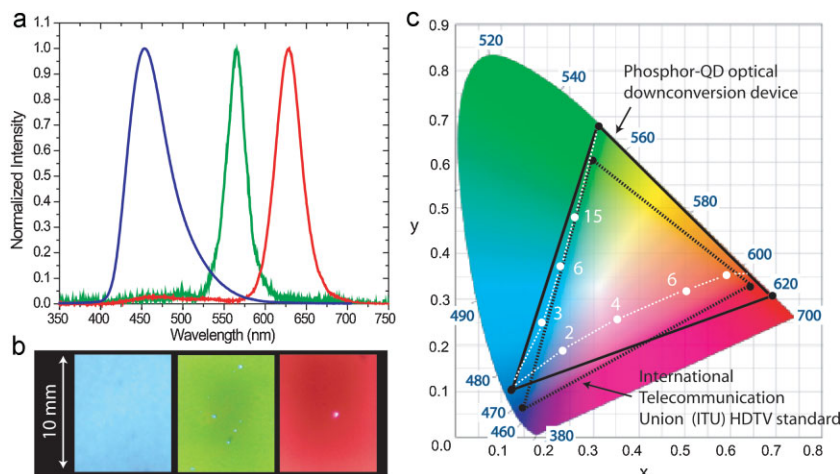


Figure 2. a,b) Electroluminescence spectra and photographs of red, green, and blue 80 mm² pixels. c) Device CIE coordinates plotted on a chromaticity diagram show that the optical down-conversion devices subtend a color triangle (solid black line) comparable to that of the International Telecommunication Union HDTV standard (dotted black line). The dotted white lines indicate two examples of possible ranges of color that can be obtained by simply varying the thickness of the printed QD-PIB layer fabricated with a single QD-ink solution. The numbers written next to the white data points indicate the number of layers of the QD-PIB ink used to achieve the designated color.

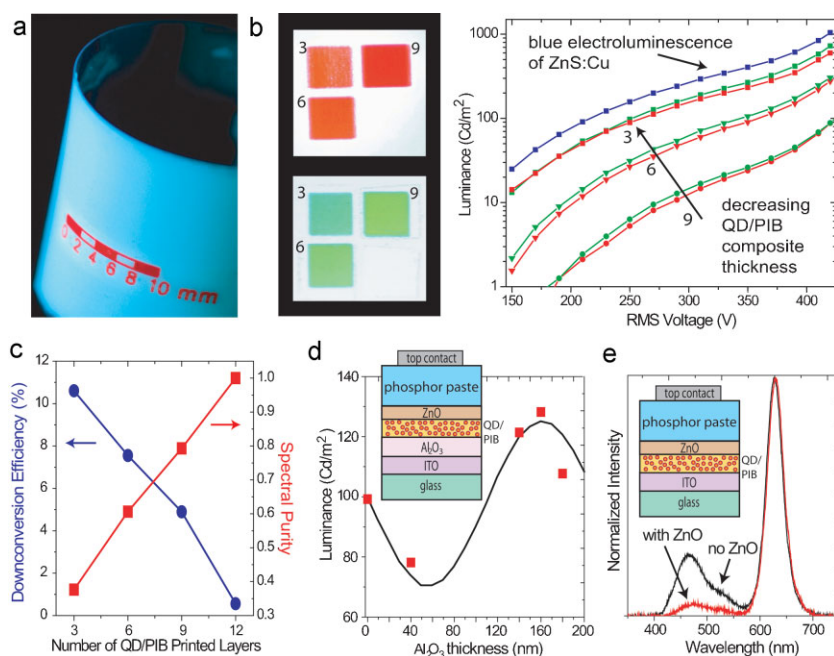


Figure 3. a) Photograph of a complete device on a flexible substrate under $\lambda = 365$ nm wavelength illumination. The ruler pattern printed with red QD-PIB ink is to scale. b) Photographs of the photoluminescence devices with three, six, and nine layers of inkjet-printed QD-PIB under $\lambda = 365$ nm wavelength illumination, provide a visual indication of the color purity. The plot shows luminance versus applied RMS voltage for a blue (ZnS:Cu phosphor only) pixel as well as the red and green pixels with three, six, and nine layers of QD-PIB. c) Plot of the spectral purity and down-conversion efficiency as a function of QD-PIB-layer thicknesses. d) Data are taken from devices with ZnO layers 50 nm thick and variable thickness of Al₂O₃ transparent metal oxide layers, positioned as shown with the inset schematic. The plot shows measured (data points) and modeled (black line) device luminance as a function of Al₂O₃ layer thickness. The data follow the oscillatory trend predicted by the model described in the text. e) The electroluminescence spectra for devices with and without a 20 nm ZnO layer indicate that the ZnO contributes to wave-guiding of the phosphor electroluminescence in the plane of the substrate, which facilitates an improved color purity of the emission. The inset schematic shows the placement of the ZnO layer in the device structure.

with a ruler pattern that marks off 2 mm divisions for a 1 cm shape printed to scale.

We measure luminance as a function of applied AC voltage for devices with different numbers of printed red and green QD-PIB layers, as well as for blue (ZnS:Cu phosphor only) devices (Fig. 3b). The luminance versus RMS-voltage plot highlights the tradeoff between spectral purity and brightness at a specific driving voltage. As shown in Figure 3c, the spectral purity, defined as the fraction of the device electroluminescence spectrum comprised of QD emission, increases as a function of the number of QD-PIB layers. The down-conversion efficiency, which we define as the ratio of the watts of QD emission collected to the watts of the phosphor emission created, decreases as a function of the number of QD-PIB layers. These trends provide insight into the performance of our devices. For a thin QD-PIB layer (2 μ m thick), we measure down-conversion efficiencies near 12%. This is consistent with the 15% PL efficiency of the QDs in the PIB matrix with additional losses due to QD light self-absorption. As the thickness of the QD-PIB layer increases, less blue light reaches the QDs furthest from the phosphor layer, while lower-energy emission from the layer of QDs closest to the phosphor is subject to more scattering and reabsorption.

The luminous efficiency of our devices is approximately 0.1 lm W⁻¹ for the blue phosphor driven with 420 V_{rms} at 31 kHz, which is comparable to commercially available AC-power EL devices.^[1] The electronic properties of the device are dominated by the thick phosphor layer (500 μ m in thickness), so small changes in the QD-PIB layer thickness do not contribute substantially to variation in the input power needed to drive the device.

Device luminance can be increased when additional transparent metal oxide layers are inserted into the device structure. We limit our choice of metal oxides to materials that are robust insulators, and investigate device structures with metal oxides on either side of the QD-PIB composite layer, such as the one shown schematically in the inset of Figure 3d. To determine the layer thicknesses of the metal oxides needed to simultaneously maximize absorption of the phosphor luminescence by the QDs and the transmission of the QD luminescence through the glass to the viewer, we model the device as a dielectric stack.^[14] We use a transmission and propagation numerical-simulation matrix method and integrate over all emission angles to account for off-normal transmission and reflection, as

well as wave-guided luminescence. The simulation also accounts for the wavelength dependence of the absorption and emission profiles of the different layers. We apply the Maxwell–Garnett mixing rule relation to determine values of the index of refraction for the phosphor ($n = 2.3$) and the QD–PIB layer ($n = 1.8$).^[1,15] The complex part of the QD index of refraction is calculated from the absorption data of QD–PIB films printed on glass substrates. We find that ZnO, which has an index of approximately 2.0 in the visible-light wavelength range, is a desirable buffer layer between the phosphor and the QD–PIB matrix, as it laterally waveguides some of the phosphor electroluminescence, which facilitates an improved color purity of the top-surface QD emission. To minimize wave-guiding of the QD emission in the ITO layer (refractive index ≈ 2.0), the lower index Al_2O_3 (≈ 1.6) can be inserted between the ITO and the QD–PIB layer. Our model indicates that transmission of QD luminescence to the viewer is maximized using a layer of ZnO 50 nm thick and a layer of Al_2O_3 160 nm thick.

To demonstrate that predicted trends in luminance are indeed observed, we fabricate devices with layers of ZnO and/or Al_2O_3 . We deposit the metal oxides with radio frequency magnetron sputtering, which has been shown to be compatible with QDs in a LED structure and is a common, low-cost, and low-temperature technique for depositing thin-film coatings.^[6c] We fabricate devices, as shown in Figure 3d, with Al_2O_3 -film thicknesses of 0, 40, 140, 160, and 180 nm on ITO, followed by nine inkjet-printed QD–PIB layers, and 50 nm of ZnO. Figure 3d plots luminance measured at 420 V_{rms} and 31 kHz versus Al_2O_3 thickness for these devices. The data follow the oscillatory trend predicted by the optical modeling. To demonstrate the wave-guiding effect in the ZnO layer, we fabricate devices with and without a 20 nm layer of ZnO on top of the QD–PIB composite. As shown by the device electroluminescence spectra in Figure 3e, the ZnO layer wave-guides the phosphor emission in the plane of the substrate, decreasing the transmission of blue light to the viewer while still allowing excitation of the QDs. The demonstrated use of sputtered metal oxide films in the device structures confirms that the inkjet-printing technique is compatible with AC thin-film EL devices in which two thick insulating layers, such as Al_2O_3 , surround a crystalline phosphor layer.^[1]

In conclusion, we have demonstrated a simple and scalable method to achieve patterned pixels for flexible, full-color, large-area, AC-driven displays operating at video brightness. We have shown that a QD–polymer composite can be printed using stable ink solutions, and that it contributes to an efficient and robust device architecture. Optimization of the QD–polymer composite layer thickness can be used to tune luminance and color for specific applications. Finally, our inkjet-printing technique is well-suited for integration with metal oxide dielectric layers, which can enable improved optical and electrical performance.

Experimental

The QD–PIB ink solution is a mixture of PIB and colloidal QDs dispersed in hexane and octane. 400 000 molecular-weight PIB (Acros #17818) was dissolved in hexane and octane (0.1 g PIB per 10 mL hexane and 1 mL of octane). The appropriate ratio of hexane to octane was

determined experimentally, as described in the Supporting Information. This PIB solution was then mixed with a solution with 2 mg mL^{−1} concentration of QDs in hexane in proportions of one part PIB solution to between two and four parts QD solution. The exact optimal proportion for inkjet printing was based on desired drop size and QD-loading fraction. Successful prints were demonstrated with inks that used nanoparticles from a variety of sources. CdSe/ZnS QDs were obtained from QD Vision Inc. and from Evident Technologies Inc., with solution photoluminescences of the various QDs peaked at wavelengths of 530 nm, 547 nm, 612 nm, and 614 nm. To remove excess ligands, the QDs were repeatedly crashed out in methanol and then redispersed in hexane. In-house-synthesized CdSe/ZnS QDs and nanorods with solution photoluminescences peaked at wavelengths of 608 and 630 nm were also used.

Devices were fabricated with a layer-by-layer approach that was compatible with flexible substrates. The QD–PIB inks were printed on conductive ITO. The ITO was obtained on glass substrates from Thin Films Inc. or on flexible polyethylene terephthalate (PET) substrates from Sheldahl Inc. Printing was realized with a Hewlett–Packard Thermal Inkjet Picofluidic dispensing System (TIPS) operated in conjunction with a Labview controlled precision movable stage. Patterns in this work were formed with 50–300 pL drop volumes, deposited at a 50 μm to 100 μm pitch.

The blue phosphor used in this study was Type 813 ZnS:Cu powder dispersed in electroluminescent binder from Osram-Sylvania. This phosphor was doctor-blade-deposited with a 500 μm thickness using a disposable mask to define the active device area and the bottom ITO contacts. The sample was dried at 50 °C for 2 h. Top contacts were produced using conductive tape from 3M (# 9713). This basic device structure was assembled and tested entirely in ambient conditions.

Al_2O_3 and ZnO metal oxide layers were deposited using radio-frequency magnetron sputtering in an inert Ar environment at 4 mTorr (1 Torr = 133.32 Pa). The metal oxide layers were deposited using sputtering targets with 3 inch diameter mounted on US Inc. sputtering guns with a power of 150 W used for the Al_2O_3 deposition and 25 W for the ZnO deposition, corresponding to deposition rates of 0.4 Å s^{−1} and 0.2 Å s^{−1}, respectively.

Photographs of PL were taken with the sample illuminated with a UV lamp at a wavelength of 365 nm. PL spectral measurements were obtained with the sample excited using a 408 nm wavelength laser. The electroluminescence and PL spectra were taken with an Acton Research SpectraPro 300i. Absorption was determined from reflection and transmission measurements taken using a Cary 500i spectrophotometer. The diffuse reflectance accessory was used to measure the absorption of the QD–PIB matrix. PL efficiencies of the spun-cast QD thin films and the inkjet-printed QD–PIB layers were determined by comparing the number of photons emitted from the samples and the sample absorption at $\lambda = 408$ nm against the same measurements on a tris-(8-hydroxyquinoline) aluminum (Alq_3) standard.

Voltage-dependent measurements were performed with a 31 kHz AC signal provided by a JKL inverter (BXA-24529). Lower-voltage, frequency-dependent measurements were taken using a Hewlett–Packard 3245A Universal Source. Luminance measurements and CIE coordinates were obtained using a Konica–Minolta CS-200 luminance and color meter. Input power to the device was calculated measuring the voltage drops across the device and a series resistor and the phase angle between the two signals using a Tectronix TDS 3054B oscilloscope.

Acknowledgements

The authors thank QD Vision Inc. for supplying quantum dots used in this work and Sheldahl Inc. for providing flexible ITO-coated PET substrates. We also thank Dr. M. Chaparala (Hewlett Packard), G. Su, and P. Anikeeva for their assistance and helpful discussions. This work made use of MRSEC Shared Experimental Facilities at MIT, supported by the National Science Foundation under award number DMR-02-13282. Funding for this project was provided by the Institute for Soldier Nanotechnologies, the DARPA

MIT-OSU-HP Focus Center on Non-Lithographic Technologies for MEMS/NEMS, a Presidential Early Career Award for Scientists and Engineers, and a NDSEG Fellowship. Supporting Information is available online from Wiley InterScience or from the author.

Received: November 5, 2008

Revised: December 23, 2008

Published online: March 4, 2009

-
- [1] Y. A. Ono, *Electroluminescent Displays*, World Scientific, Singapore **1995**.
 [2] C. N. King, *J. Vac. Sci. Technol. A* **1996**, *14*, 1729.
 [3] a) T. Minami, *Solid-State Electron.* **2003**, *47*, 2237. b) K. Tanaka, Y. Kimura, S. Okamoto, Y. Inoue, K. Sato, *Jpn. J. Appl. Phys. Part 1* **1998**, *37*, 3350.
 [4] P. E. Burrows, G. Gu, V. Bulović, Z. Shen, S. R. Forrest, M. E. Thompson, *IEEE Trans. Electron Devices* **1997**, *44*, 1188.
 [5] C. B. Murray, D. J. Norris, M. G. Bawendi, *J. Am. Chem. Soc.* **1993**, *115*, 8706.
 [6] a) S. Coe, W.-K. Woo, M. G. Bawendi, V. Bulović, *Nature* **2002**, *420*, 800. b) J. S. Steckel, J. P. Zimmer, S. Coe-Sullivan, N. E. Stott, V. Bulović, M. G. Bawendi, *Angew. Chem. Int. Ed.* **2004**, *43*, 2154. c) S. Coe-Sullivan, J. S. Steckel, L. A. Kim, M. G. Bawendi, V. Bulović, *Light-emitting Diodes: Research, manufacturing, and Applications IX*, Proc. SPIE (Eds: S. A. Stockman, H. W. Yao, E. F. Schubert), San Jose **2005**, pp. 108–115. d) J. S. Steckel, P. Snee, S. Coe-Sullivan, J. P. Zimmer, J. E. Halpert, P. Anikeeva, L. A. Kim, V. Bulović, M. G. Bawendi, *Angew. Chem. Int. Ed.* **2006**, *45*, 5796. e) J. M. Caruge, J. E. Halpert, V. Wood, V. Bulović, M. G. Bawendi, *Nat. Photonics* **2008**, *2*, 247.
 [7] J. Lee, V. C. Sundar, J. R. Heine, M. G. Bawendi, K. F. Jensen, *Adv. Mater.* **2000**, *12*, 1102.
 [8] R. M. Taylor, K. H. Church, M. I. Sluch, *Displays* **2007**, *28*, 92.
 [9] M. Böberl, M. V. Kovalenko, S. Gamerith, E. J. W. List, W. Heiss, *Adv. Mater.* **2007**, *19*, 3574.
 [10] a) R. D. Deegan, O. Bakajin, T. F. Dupont, G. Huber, S. R. Nagel, T. A. Witten, *Nature* **1997**, *389*, 827. b) R. D. Deegan, O. Bakajin, T. F. Dupont, G. Huber, S. R. Nagel, T. A. Witten, *Phys. Rev. E* **2000**, *62*, 756.
 [11] a) S. Coe-Sullivan, J. S. Steckel, W. K. Woo, M. G. Bawendi, V. Bulović, *Adv. Funct. Mater.* **2005**, *15*, 1117. b) E. Tekin, P. J. Smith, S. Hoeppener, A. M. J. van de Berg, A. S. Susha, A. L. Rogach, J. Feldmann, U. S. Schubert, *Adv. Funct. Mater.* **2007**, *17*, 23. c) J. A. Lim, W. H. Lee, H. S. Lee, J. H. Lee, Y. D. Park, K. Cho, *Adv. Funct. Mater.* **2008**, *18*, 229.
 [12] D. E. Fogg, L. H. Radzilowski, R. Blanski, R. R. Schrock, E. L. Thomas, M. G. Bawendi, *Macromolecules* **1997**, *30*, 417.
 [13] P. O. Anikeeva, J. E. Halpert, M. G. Bawendi, V. Bulović, *Nano Lett.* **2007**, *7*, 2196.
 [14] J. A. Kong, *Electromagnetic Wave Theory*, EMW Publishing, Cambridge **2000**.
 [15] A. Sihvola, *Subsurf. Sens. Technol. Appl.* **2000**, *1*, 393.
-

Alternating Current Driven Electroluminescence from ZnSe/ZnS:Mn/ZnS Nanocrystals

Vanessa Wood,^{†,‡} Jonathan E. Halpert,^{†,§} Matthew J. Panzer,[‡]
Moungi G. Bawendi,[§] and Vladimir Bulović^{*,‡}

Department of Electrical Engineering and Computer Science and Department of Chemistry, Massachusetts Institute of Technology, Cambridge, Massachusetts 02139

Received March 20, 2009; Revised Manuscript Received April 17, 2009

ABSTRACT

We present a novel technique for room temperature, solution-based fabrication of alternating current thin-film electroluminescent (AC-TFEL) devices using phosphor-doped nanocrystals. Synthesis for stable ZnSe/ZnS:Mn/ZnS nanocrystals that exhibit a quantum yield of $65 \pm 5\%$ is outlined, and their electroluminescence is demonstrated in structures consisting of only wide band gap ceramic layers. Both the nanocrystal and the ceramic films have minimal absorption across the visible light spectrum, enabling us to demonstrate transparent AC-TFEL devices.

Alternating current thin-film electroluminescent (AC-TFEL) devices already occupy a segment of the large area, high-resolution, flat panel display market. AC-TFEL displays are robust, possess long lifetimes, and offer high luminance with relatively low power consumption.¹ AC-TFEL devices consist of a phosphor layer, such as manganese-doped zinc sulfide (ZnS:Mn), vertically sandwiched between two insulators that are contacted by electrodes. When a sufficiently high voltage is applied across the electrodes, electrons trapped at interfaces between the layers are injected into the conduction band of the phosphor, where they are accelerated by the field and can excite the luminescent dopant centers in the phosphor layer via impact excitation and ionization mechanisms.^{2,3}

While fabrication of AC-TFEL devices have been the subject of considerable study over the past 3 decades, challenges remain. Development of multicolor displays with balanced red, green, and blue (RGB) emission has proven difficult as the most efficient red, green, and blue phosphors comprise different materials systems that require different deposition and annealing steps.^{1,4,5} Additionally, differences in luminous efficiencies of different colors can span an order of magnitude, complicating electronic driving of balanced color displays.^{1,4,5} Transparent AC-TFEL displays have recently been demonstrated by Sharp, Inc.; however, the processing of the phosphor to achieve transparency is difficult and has not yet been developed for phosphors other than ZnS:Mn.⁶

In this Letter, we present a novel materials system for the active phosphor layer in transparent AC-TFEL devices. We use colloiddally synthesized Mn-doped nanocrystals to demonstrate electroluminescence (EL) from a solution-deposited active layer in an AC-TFEL device fabricated at room temperature. Wide band gap host nanocrystals and wide band gap metal oxides enable transparent device structures without additional processing steps beyond the room-temperature layer-by-layer deposition of each material set.

To date, colloidal nanocrystals have successfully been doped with transition metals (such as Fe, Ni, Mn, Cu) and lanthanides (such as Eu, Er, Tm, Tb) to alter their electronic, optical, or magnetic properties.^{7–12} If the excitation energy of the dopant is smaller than the band gap of the host material, the photoluminescence of the doped nanocrystal is determined by the dopant atoms; light emission is independent of the band gap of the host material and largely immune to thermal and chemical variations of the surrounding medium.¹³ For example, by using different dopants or various synthetic procedures,¹⁴ the emission wavelength of doped ZnSe nanocrystals can be tuned from the blue through the red, suggesting the possibility of developing multicolored AC-TFEL displays. However, until now, there has been no demonstration of EL from phosphor impurity dopants in ZnSe or other wide band gap host nanocrystals. Luminescence of CdS:Mn/ZnS nanocrystals embedded into a polymer-LED was observed;¹⁵ however, color-tunable doping or a transparent device is challenging to achieve with this structure because of the relatively small band gap of CdS. In order for these doped nanocrystals to be luminescent at the colors of the dopant, the excitation energy of the dopant

* Corresponding author, bulovic@mit.edu.

[†] These authors contributed equally to this work.

[‡] Department of Electrical Engineering and Computer Science.

[§] Department of Chemistry.

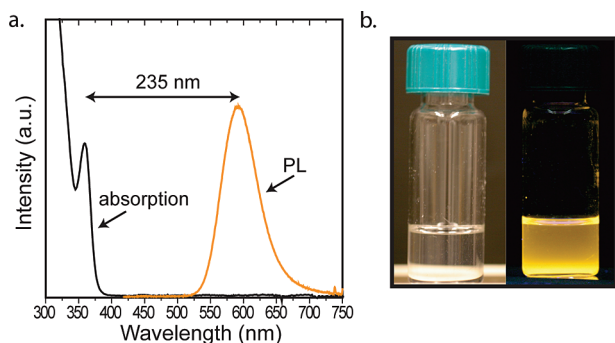


Figure 1. (a) The absorption (black line) and photoluminescence (orange line) spectra of the ZnSe/ZnS:Mn/ZnS nanocrystals in solution show a large (235 nm) Stokes shift. (b) Photographs of a vial of ZnSe/ZnS:Mn/ZnS nanocrystals in chloroform under room lighting (left) and under UV illumination (right) provide visual confirmation of the spectra shown in panel a, which indicate that these orange-emitting nanocrystals exhibit no absorption in the visible wavelength regime.

needs to be smaller than the band gap of the host material to enable energy transfer of an exciton on the nanocrystal core to the impurity dopant. Furthermore, when the nanocrystal host material is a wide band gap semiconductor such as ZnSe, thin films of nanocrystals do not absorb in the visible wavelength region (see Figure 1a), making them compatible with the construction of transparent devices. Such devices could be used for displays with two-way, heads-up viewing capabilities.

Colloidal solutions of doped nanocrystals also bring a key advantage to the fabrication of AC-TFEL displays. Solution processing of nanocrystalline colloids enables a wide range of deposition techniques such as spin-casting,^{16,17} microcontact printing,¹⁸ inkjet printing,¹⁹ and electrospray²⁰ to be employed for their integration into electroluminescent devices. Previously, some of these printing techniques have been used to demonstrate side-by-side patterning of nanocrystals of different emission colors with up to 1000 dpi pattern resolution (25 μm features), as would be necessary for high-resolution displays.¹⁸ In our demonstration of the transparent AC-TFEL device we use multilayer spin-casting of phosphor-doped nanocrystal solutions for the active emissive layer.

We choose to work with Mn-doped nanocrystals as Mn is the most commonly used phosphor dopant in AC-TFEL devices. We report a synthesis of ZnSe/ZnS:Mn/ZnS nanocrystals that offers the stability and high quantum yield needed for AC-TFEL applications. The high quantum yield of these ZnSe/ZnS:Mn/ZnS nanocrystals is due to their thick ZnS shell, which localizes the excited state on the Mn-dopant atom by preventing energy transfer to surface states or the surrounding medium. The thick shell also improves the stability of the nanocrystal, preventing migration of the Mn dopant.

The synthesis of ZnSe/ZnS:Mn/ZnS nanocrystals used in this study is adapted from Thakar et al.²¹ The ratio of Zn and S precursors in the overcoating step, the final ZnS shell thickness, and the ligand chemistry possible account for the greater quantum yield in our nanocrystals. ZnSe cores are

prepared by injecting 96 mg of diethyl zinc and 0.67 mL of trioctylphosphine (TOP) selenide into a flask of 10 mL of oleylamine, degassed at 140 °C. After the mixture was heated at 270 °C for 90 min, the flask is cooled to 170 °C and a solution of 45 mg of manganese stearate, 76 mg of diethyl zinc, and 160 mg of hexamethyldisilathiane in 6 mL of TOP is added at a rate of 1 drop/s. These ZnSe/ZnS:Mn particles are precipitated twice using methanol and butanol and redispersed in hexane. This solution is then added to a degassed flask containing 10 g of trioctylphosphine oxide (TOPO) and 0.4 g of *n*-hexylphosphonic acid (HPA) at 80 °C. The hexane is removed under vacuum. The flask is then placed under argon and heated to 170 °C. A solution of 80 mg of diethyl zinc and 160 mg of hexamethyldisilathiane in 5 mL of TOP is added dropwise, and the flask is cooled to room temperature. Four milliliters of hexane and 4 mL of butanol are then added. The ZnSe/ZnS:Mn/ZnS nanocrystals are finally precipitated twice using methanol and butanol and redispersed in chloroform.

Figure 1a shows the absorption and photoluminescence (PL) spectra for these nanocrystals in solution. As discussed previously, the nanocrystals do not absorb in the visible wavelength region because the host material, ZnSe, is a wide band gap semiconductor. The PL spectrum is centered at wavelength $\lambda = 590$ nm, which is characteristic of the Mn $^4\text{T}_1 \rightarrow ^6\text{A}_1$ phosphor transition.²¹ Streak camera measurements of this luminescence reveal an excited state lifetime in excess of 1 ms, consistent with the expected phosphorescent emission decay mechanism. The photographs of the nanocrystals in room light and under UV illumination (Figure 1b) provide a visual indication of the transparency of the nanocrystals as well as their high quantum yield (QY), which we measure to be $65 \pm 5\%$ for the nanocrystals in solution. A direct measurement of QY by comparing the solution to an organic dye is not possible due to the large Stokes shift in the ZnSe/ZnS:Mn/ZnS nanocrystals. The QY measurement is therefore performed by comparing the nanocrystal solution to a solution of orange emitting CdSe/ZnS quantum dots with a QY of 65%, previously calibrated to a solution of Rhodamine 610 (QY = 95%). In addition to having a high QY, the ZnSe/ZnS:Mn/ZnS nanocrystal solution also exhibits a long shelf life. Figure 1b shows a nanocrystal solution synthesized over 1 year prior to the date of the photographs.

The AC-TFEL device structure that enables electrical excitation of the doped nanocrystals is shown schematically in Figure 2a. It is fabricated using room temperature radio frequency (rf) magnetron sputtered ceramics and solution-deposited nanocrystals. We begin by sputtering 80 nm of an insulating metal oxide of either Al_2O_3 or HfO_2 onto commercially deposited indium tin oxide (ITO) on glass from Thin Film Devices, Inc. Both the bottom and top insulating layers are sputtered in an inert Ar environment at 4 mTorr with a power of either 150 W (for Al_2O_3) or 100 W (for HfO_2). The sputter-deposited insulating films are complete and planar, as revealed by atomic force microscopy (AFM) characterization. For a device consisting of Al_2O_3 layers, for example, we measure a root-mean-square (rms) surface roughness of 0.3 nm for the bottom layer and a surface

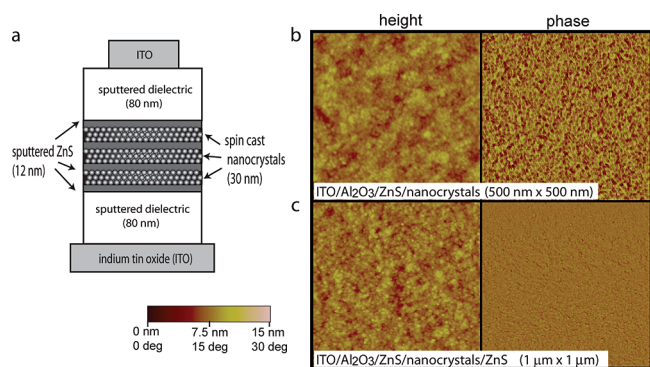


Figure 2. (a) A schematic of the doped nanocrystal-based AC-TFEL device structure. AFM topographic and phase images show (b) the first layer of nanocrystals spin-cast on ZnS and (c) a subsequent layer of ZnS sputtered on top of the nanocrystals. Comparison of the phase images in panels b and c shows that the nanocrystals are completely covered by the 12 nm layer of ZnS.

roughness of 0.9 nm (rms) for the top layer. The observation of sub-1-nm roughness over a $5\ \mu\text{m} \times 5\ \mu\text{m}$ area of the top insulating layers indicates that the multiple ZnS and nanocrystal layers in the middle of the device structure maintain planarity throughout the multilayer growth.

The active layer of the device consists of alternating layers of sputtered ZnS and spin-cast ZnSe/ZnS:Mn/ZnS nanocrystals. Each layer of ZnS is 12 nm thick and is sputter-deposited with a power of 25 W in 4 mTorr of Ar. A thickness of 12 nm of ZnS is chosen because it is enough to form a complete layer that is not damaged upon subsequent spin-casting of the next nanocrystal layer. Thicker ZnS layers, while also complete and capable of withstanding the subsequent spin-casting steps, increase the turn on voltage of the device. The layers of nanocrystals are spin-cast in a nitrogen glovebox onto the ZnS at a speed of 1200 rpm from chloroform. Cross sectional AFM scans indicate that the total thickness of each layer of nanocrystals is approximately 30 nm, corresponding to approximately four to five layers of nanocrystals. Panels b and c of Figure 2 show AFM topography and phase images of the nanocrystal layer and the first ZnS layer on top of the nanocrystals. Figure 2b reveals a highly monodisperse film of 5 nm diameter nanocrystals. The rms roughnesses of the two layers are 1 and 0.8 nm, respectively, indicating that both the nanocrystals and the ZnS form smooth, complete layers. The contrast between the phase images in panels b and c of Figure 2 (right-hand panel) further confirms the completeness of the ZnS layer on top of the nanocrystals. The device is completed with a second, 80 nm thick insulating layer and a 150 nm thick top electrode of either ITO or Al, which are sputtered at 35 W in 4 mTorr of Ar. Use of top ITO electrodes results in a highly transparent completed structure.

In the AC-TFEL architecture presented here, the alternating layers of ZnS and nanocrystals are necessary for device electroluminescence (EL). To confirm that the ZnS layers are critical to device operation, we fabricate four devices with continuous 30 or 90 nm thick layers of ZnSe/ZnS:Mn/ZnS nanocrystals sandwiched between both Al_2O_3 and HfO_2 dielectric layers. The 90 nm thick layer is spin-cast using a

more concentrated solution of nanocrystals, and its thickness and uniformity are characterized by AFM, as described previously. No EL is observed from these devices, indicating that the device luminescence is determined by the number of ZnS layer–nanocrystal interfaces and not by the number of luminescent impurity centers.

To determine the optimal number of ZnS layers within the device, we fabricate structures with two, three, four, or five 12 nm thick ZnS layers (sandwiching one, two, three, or four layers of nanocrystals, each of which is 30 nm thick). Eighty nanometer thick Al_2O_3 layers are used as the dielectrics for the four devices with Al as the top contact. EL is measured while the devices are biased with a square-wave pulse at a frequency of 30 kHz and peak-to-peak voltage (V_{pp}) of 110 V. The trend in EL response is shown in Figure 3a. The luminescence from the device with two layers of ZnS is below our reliable detection threshold. We find four layers of ZnS to be optimal; devices with three and five layers of ZnS (containing two or four layers of nanocrystals, respectively) exhibit lower EL intensity than the device with four ZnS layers. The device with five layers of ZnS (and four layers of nanocrystals) can operate at the same brightness as the four ZnS layer device but requires an increased operating voltage to do so because of the additional voltage drop across the insulating layers of ZnS and nanocrystals. Likewise, devices with multiple 90 nm thick nanocrystal layers exhibit electroluminescence but require higher operating voltages than devices with 30 nm thick nanocrystal layers to achieve the same field drop across the nanocrystal layers. These results demonstrate the importance of maximizing both the number of interfaces and the electric field dropped across the nanocrystal layers.

The following results pertain to transparent devices with four layers of ZnS and three 30 nm thick layers of nanocrystals, depicted schematically in Figure 2a. The photographs in Figure 3b provide a visual indication of device transparency, as well as the uniform illumination at $2\ \text{Cd/m}^2$ of a $1\ \text{mm} \times 2\ \text{mm}$ pixel with an applied voltage of $170\ V_{\text{pp}}$ at 30 kHz. We test our device using an HP 3254A function generator, which enables us to sweep frequency across a large range with voltages up to $200\ V_{\text{pp}}$. We observe that our devices show EL emission at frequencies greater than 10 kHz and with voltages as low as $110\ V_{\text{pp}}$ (for operation at 30 kHz). Trends of increasing EL intensity as a function of both increasing voltage and increasing frequency are shown in Figure 3c. While these trends are consistent with impact excitation of the Mn impurity dopant whereby electrons are accelerated across the sputtered ZnS layers, the trends also suggest a possible mechanism in which the high electric field causes an electron to be removed from the valence band of the nanocrystal, leaving a hole behind. An electron from a neighboring nanocrystal, aided by the field, can then couple with the hole to form an exciton on the ZnSe core whose energy can be transferred to the Mn impurity dopant. Further experiments are needed to probe in detail the operating mechanism of these devices.

Figure 3d shows the normalized EL spectra for a device with Al_2O_3 (solid orange line) and HfO_2 (dashed orange line)

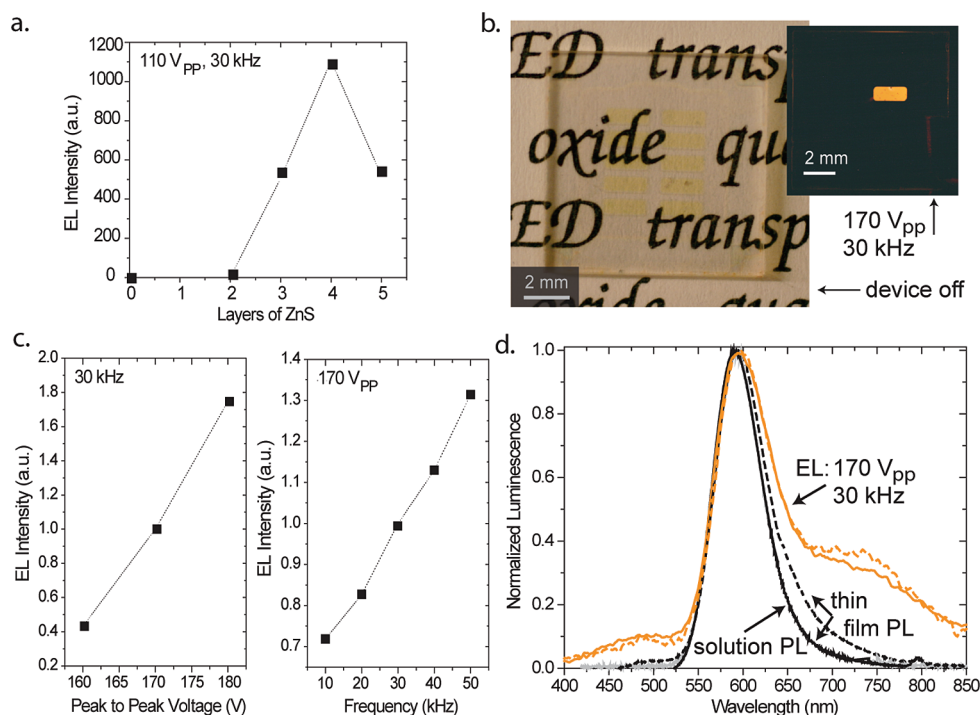


Figure 3. (a) Plot of the electroluminescent (EL) intensity versus the number of layers of ZnS in the device structure. We find that for a given bias condition (here, 110 V_{pp} at 30 kHz), devices with four layers of ZnS (and three 30 nm thick layers of nanocrystals) give the largest EL response. (b) A photograph of a 0.5 in. × 0.5 in. glass substrate containing 10 1 mm × 2 mm AC-TFEL devices, with no bias applied. The substrate is pictured on top of printed text to demonstrate the transparency of the AC-TFEL device architecture. The inset shows the uniformity of pixel illumination (in the dark) with the device operating at 170 V_{pp} and 30 kHz. (c) Plots of the EL response as a function of drive voltage and frequency. Values are normalized with respect to the EL response at 170 V_{pp} and 30 kHz. (d) The EL spectra for devices with Al₂O₃ and HfO₂ insulating layers are presented by the solid and dashed orange curves, respectively. The bias conditions are 170 V_{pp} and 30 kHz. A photoluminescence (PL) spectrum of an incomplete device structure (ITO/Al₂O₃/ZnS/30 nm nanocrystals) (solid black curve) matches solution PL spectrum of the nanocrystals in chloroform (solid gray curve). The PL spectrum of a more complete device (consisting of ITO/Al₂O₃/ZnS/30 nm nanocrystals/ZnS) in which ZnS has been sputtered onto the nanocrystals is shown with the dashed black line.

insulating layers, both operating at 30 kHz and 170 V_{pp}. The overlap of these spectra confirms that the insulating layer does not contribute to or affect the observed EL spectral shape. The dominant peaks in the two EL spectra overlap with the solution PL spectrum (gray line), indicating that the phosphor ⁴T₁ → ⁶A₁ transition accounts for the EL response. The broad background emission that spans from 450 nm wavelength into the near-IR is likely a result of electrical excitation of ZnSe defect states that could be created during the sputtered ZnS layer deposition. These defect states could similarly be excited by exciton energy transfer from the ZnSe core. A PL spectrum (black line) of an incomplete device structure (ITO/Al₂O₃/ZnS/30 nm nanocrystals) matches the solution PL spectrum and shows no evidence of defect states. However, the PL spectrum of a more complete structure consisting of ITO/Al₂O₃/ZnS/30 nm nanocrystals/ZnS (dashed black line) exhibits broadening of the red and blue edges of the nanocrystal luminescence, which is indicative of defect states. The defect states are more prominent in the EL spectra than in the PL spectrum, suggesting that the PL excitation probes all nanocrystals while the EL signal is dominated by nanocrystals at the ZnS interface. While the shape of the EL spectrum is the same regardless of the insulating layer used, the EL intensity is a factor of 2 less for devices using HfO₂ instead of Al₂O₃. This observation is consistent with a field-driven excitation

mechanism for the doped nanocrystals. Since the static dielectric constant of HfO₂ is approximately twice that of Al₂O₃, we expect that the field drop will be larger across the HfO₂ layers than across the Al₂O₃ layers in otherwise comparable device structures. This implies a reduction in the electric field across the nanocrystals and ZnS in the HfO₂-containing structures, which is consistent with the observed lower EL intensity of HfO₂-containing structures.

In summary, we demonstrated ac-driven electroluminescence from highly efficient and stable ZnSe/ZnS:Mn/ZnS nanocrystals. Our device structures contain standard wide band gap ceramic materials which eliminate charge injection into the devices, limiting the electrical excitation of the nanocrystals to field-driven mechanisms. Because the demonstrated device architecture is comparable to existing AC-TFEL technology, our use of spin-casting to deposit the nanocrystals in multilayer stacks highlights the viability of solution-based techniques for depositing the active phosphor layer in AC-TFEL devices, which could enable print fabrication of transparent multicolor AC-TFEL displays.

Acknowledgment. The authors thank Dr. Gerry Chen and Dr. Steve Kooi for their assistance. This work is supported by the Institute for Soldier Nanotechnologies (DAAD-19-02-0002), a Presidential Early Career Award for Scientists and Engineers, and a National Defense

Science and Engineering Graduate Fellowship. This work also made use of MRSEC Shared Experimental Facilities at MIT, supported by the National Science Foundation under Award Number DMR-02-13282.

References

- (1) Ono, Y. A. *Electroluminescent Displays*; World Scientific: River Edge, NJ, 1995.
- (2) Keir, J. P.; Wager, J. F. *Annu. Rev. Mater. Sci.* **1997**, *27*, 223.
- (3) Dur, M.; Goodnick, S. M.; Pennathur, S. S.; Wager, J. F.; Reigrotzki, M.; Redmer, R. *J. Appl. Phys.* **1998**, *83*, 3176.
- (4) Li, D.; Clark, B. L.; Keszler, D. A.; Keir, P.; Wager, J. F. *Chem. Mater.* **2000**, *12*, 268.
- (5) King, C. *Electroluminescent Displays*; Planar Systems: Beaverton, OR, 2003.
- (6) Abileah, A.; Harkonen, K.; Pakkala, A.; Smid, G. *Transparent Electroluminescent (EL) Displays*, Planar Systems: Beaverton, OR, 2008.
- (7) Alivisatos, A. P. *Science* **1996**, *271*, 933.
- (8) Shim, M.; Guyot-Sionnest, P. *Nature* **2000**, *407*, 981.
- (9) Levy, L.; Hocheppied, J. F.; Pileni, M. P. *J. Phys. Chem.* **1996**, *100*, 18322.
- (10) Hanif, K. M.; Meulenber, R. W.; Strouse, G. F. *J. Am. Chem. Soc.* **2002**, *122*, 2532.
- (11) Wang, Y.; Herron, N.; Moller, K.; Bein, T. *Solid State Commun.* **1991**, *77*, 33.
- (12) Norris, D. J.; Yao, N.; Charnock, F. T.; Kennedy, T. A. *Nano Lett.* **2007**, *1*, 3.
- (13) Pradhan, N.; Goorskey, D.; Thessing, J.; Peng, X. *J. Am. Chem. Soc.* **2005**, *127*, 17528.
- (14) Pradhan, N.; Peng, X. *J. Am. Chem. Soc.* **2006**, *129*, 3339.
- (15) Yang, H.; Santra, S.; Holloway, P. H. *J. Nanosci. Nanotechnol.* **2005**, *5*, 1364.
- (16) Coe, S.; Woo, W.; Bawendi, M. G.; Bulović, V. *Nature* **2002**, *420*, 800.
- (17) Caruge, J.-M.; Halpert, J. E.; Wood, V.; Bawendi, M. G.; Bulović, V. *Nat. Photonics* **2008**, *2*, 247.
- (18) Kim, L. A.; Anikeeva, P. O.; Coe-Sullivan, S. A.; Steckel, J. S.; Bawendi, M. G.; Bulović, V. *Nano Lett.* **2008**, *8*, 4513.
- (19) Wood, V.; Panzer, M. J.; Chen, J. L.; Bradley, M. S.; Halpert, J. E.; Bawendi, M. G.; Bulović, V. *Adv. Mater.* **2009**, *21*, published online March 4.
- (20) Kobayashi, S.; Tani, Y.; Kawazoe, H. *Jpn. J. Appl. Phys.* **2007**, *46*, L966.
- (21) Thakar, R.; Chen, Y.; Snee, P. T. *Nano Lett.* **2007**, *7*, 3429.

NL900898T